

Influence of resonant magnetic perturbations on transient heat load deposition and fast ion losses

Inaugural-Dissertation

zur Erlangung des Doktorgrades
der Mathematisch-Naturwissenschaftlichen Fakultät
der Heinrich-Heine-Universität Düsseldorf

vorgelegt von

Michael Thomas Rack
aus Solingen

Jülich, Mai 2014

aus dem Institute für Energie- und Klimaforschung – Plasmaphysik
des Forschungszentrum Jülich

Gedruckt mit der Genehmigung der
Mathematisch-Naturwissenschaftlichen Fakultät der
Heinrich-Heine-Universität Düsseldorf

Referent: Prof. Dr. Ulrich Samm

Korreferent: Prof. Dr. Karl-Heinz Spatschek, Prof. Dr. Piero Martin

Tag der mündlichen Prüfung: 11. July 2014

Zusammenfassung

Thermonukleare Fusion ist der Energieumwandlungsprozess, der die Sonne strahlen läßt. In den letzten sechs Jahrzehnten haben Wissenschaftler die zugrundeliegende Physik untersucht, um eine solche Energieversorgung auch auf der Erde zu ermöglichen. Die erfolgversprechendsten Kandidaten für Fusionskraftwerke basieren auf dem magnetischen Einschluss von Plasma, um ideale Bedingungen für effektive thermonukleare Fusion in einer gut kontrollierten Umgebung herzustellen. Ein wichtiger Aspekt ist dabei die Kontrolle von Instabilitäten, die im Randbereich des Plasmas auftreten und zu Auswürfen von großen Energiemengen führen. Es wurde herausgefunden, dass magnetische Störfelder, die im Plasmarand resonant sind, das Plasma vorteilhaft verändern und so die Auswirkungen dieser Instabilitäten abmildern. Diese Dissertation behandelt die Effekte von resonanten magnetischen Störfeldern auf die ausgeworfene Energie sowie die Nachteile solcher Störfelder.

Der stoßartige Energieauswurf, der durch die Instabilitäten ausgelöst wird, verursacht extreme Wärmebelastungen auf den Wandkomponenten in Fusionsmaschinen. Daher ist es äußerst wichtig zu verstehen, wie resonante magnetische Störfelder die Deposition der Wärmelasten beeinflussen. Außerdem ist der Einfluss von resonanten magnetischen Störfeldern auf den Einschluss von schnellen Ionen ein wichtiger Aspekt, da schnelle Ionen weiterhin gut eingeschlossen sein müssen, um zusätzliche Wandbelastungen zu verhindern und die Fusionseffektivität zu steigern.

Kürzliche Verbesserungen am Joint European Torus erlauben eine detaillierte Untersuchung von Wärmelastdepositionsprofilen, die durch die stoßartigen Ereignisse verursacht werden. In dieser Arbeit wurden die neuen Möglichkeiten genutzt, um die Modifikationen der kurzlebigen Wärmelastdepositionen zu untersuchen, die auftreten, wenn resonante magnetische Störfelder verwendet werden. Dies führt zu einem tieferen Verständnis der beteiligten Prozesse während der Plasmarandinstabilitäten. Zusätzlich wird eine alternative Methode zur Erzeugung von resonanten magnetischen Störfeldern, unter Verwendung der unteren Hybridresonanzen, untersucht. Außerdem wird eine

neue Diagnostik vorgestellt, die zur Detektion von Verlusten schneller Ionen in der Gegenwart von resonanten magnetischen Störfeldern geeignet ist. Sie wird verwendet, um den Einfluss unterschiedlicher Arten von Störfeldern, statische und rotierende, auf die Verluste zu untersuchen.

Die Untersuchungen der Wärmelastdepositionsprofile zeigen interessante Eigenschaften der resonanten magnetischen Störfelder. Zum einen kann die Wärme gewinnbringend umverteilt werden, um den lokalen Wärmefluß zu reduzieren, zum anderen wurde erstmalig ein physikalischer Prozess beobachtet, der mit der Umverteilung der Wärme verbunden zu sein erscheint und zu langsam propagierenden Wärmeflußstrukturen führt, die lange vor dem Hauptenergieauswurf auftreten. Dies eröffnet einen neuen Blick auf die Physik von resonanten magnetischen Störfeldern, da es zeigt, dass Prozesse mit verschiedenen Zeitskalen bei der Kontrolle von Plasmarandinstabilitäten involviert sind. Die Kontrolle dieser Instabilitäten kann von der neuen Methode zum Erzeugen resonanter magnetische Störfelder unter Verwendung der unteren Hybridresonanzen profitieren. Diese Methode stellt eine hohe Flexibilität zur Verfügung, so wie es für die Optimierung der Wärmelastumverteilung benötigt wird. Es wird gezeigt, dass sie Störfelder erzeugt, welche stets im Plasmarandbereich resonant sind. Zusätzlich wurde gefunden, dass in einem weiten Bereich von Störfeldern keine klaren Nachteile entstehen, vielmehr gibt es starke Indizien dafür, dass eine Verbesserung des Einschusses von schnellen Ionen auftritt.

Die gesamten Ergebnisse geben einen positiven Ausblick auf die Verwendung von resonanten magnetischen Störfeldern für die Kontrolle von Randinstabilitäten: (a) eine vorteilhafte Umverteilung der stoßartigen Wärmebelastungen ist erreichbar, (b) die unteren Hybridresonanzen können verwendet werden um hochflexible resonante magnetische Störfelder zu erzeugen und (c) resonante magnetische Störfelder reduzieren nicht notwendiger Weise den Einschuss von schnellen Ionen. Diese Ergebnisse zeigen, dass eine Optimierung der verwendeten magnetischen Störfelder möglich ist, um die Probleme von stoßartigen Wärmebelastungen zu lösen ohne Nachteile für den wichtigen Einschuss von schnellen Ionen.

Abstract

Thermonuclear fusion is the energy conversion process which keeps the sun shining. For the last six decades, researchers have been investigating the physics involved in order to enable the usage of this energy supply on Earth. The most promising candidates for fusion power plants are based on magnetic confinement of plasma to provide the ideal conditions for efficient thermonuclear fusion in well controlled surroundings. One important aspect is the control of instabilities that occur in the edge region of the plasma and lead to an ejection of huge amounts of energy. Magnetic perturbation fields which are resonant in the plasma edge are found to modify the plasma favourably and reduce the impact of these instabilities. This dissertation focuses on the effects of resonant magnetic perturbation fields on the ejected energy as well as on the drawbacks of these perturbation fields.

The transient energy ejection which is triggered by the instabilities causes extreme heat loads on the wall components in fusion devices. Therefore, it is crucial to understand how resonant magnetic perturbation fields affect the heat load deposition. Furthermore, the impact of resonant magnetic perturbation fields on the confinement of fast ions is an important aspect as fast ions are still required to be well confined in order to avoid additional wall loads and increase the fusion efficiency.

Recent upgrades on the Joint European Torus allow for a detailed study of the heat load deposition profiles caused by transient events. Throughout this work, the new features are used for the study of the modifications of the transient heat load depositions that occur if resonant magnetic perturbation fields are applied. This leads to a further understanding of the processes involved during the plasma edge instabilities. Additionally, an alternative method using lower hybrid waves for applying resonant magnetic perturbations is investigated. Furthermore, a new diagnostic, capable of detecting fast ion losses in the presence of resonant magnetic perturbation fields, is presented. It is used to investigate the impact of various types of perturbation field, static and rotating, on the losses.

The investigations of the heat load deposition profiles show important features of the resonant magnetic perturbation fields. Firstly, the heat can be favourably redistributed to reduce the local heat fluxes; secondly, a physical process is observed that appears to be linked to the heat redistribution and causes a slow propagation of a heat flux pattern long before the major energy is ejected. This opens a new view on the physics of resonant magnetic perturbation fields as it shows that processes on different time-scales are involved during the control of the plasma edge instabilities. The control of these instabilities can benefit from the new method of applying resonant magnetic perturbation fields using lower hybrid waves. This method provides high flexibility as needed to optimize the heat load redistribution. It is proven to create perturbation fields that are always resonant in the plasma edge region. In addition, it was found that no clear drawbacks appear over a wide range of perturbation fields; moreover, strong indications for an improvement of the fast ion confinement are seen.

The overall results provide a positive outlook for the application of resonant magnetic perturbation fields to control edge instabilities: (a) an advantageous redistribution of transient heat loads is achievable, (b) lower hybrid waves can be used for the production of highly flexible resonant magnetic perturbation fields, and (c) resonant magnetic perturbation fields do not necessarily reduce the fast ion confinement. These results show that an optimization of the applied magnetic perturbation fields is able to solve the problem of transient heat loads without any drawbacks for the crucial fast ion confinement.

Contents

1. Introduction	1
2. Resonant magnetic perturbations	7
2.1. Methods of producing resonant magnetic perturbations	7
2.2. Modification of the magnetic topology	10
2.3. Effects on edge localized modes	13
2.4. Drawback: degradation of the fast ion confinement?	14
3. Effects of resonant magnetic perturbations on the distribution of heat loads due to edge localized modes	17
3.1. Dynamic structures prior to an edge localized mode crash	17
3.2. Heat load splitting during the major energy deposition	20
4. An alternative method for applying resonant magnetic perturbations	25
5. A possible drawback of applied resonant magnetic perturbations on the fast ion confinement	29
5.1. Assessment of a feasible measurement technique	29
5.2. Experimental results	31
6. Conclusions	35
Bibliography	37
A. Publications included	47
B. Commonly used acronyms	107

1. Introduction

Over the period of the compilation of this thesis, “energy” – in the form of usable energy – has been one of the main ongoing topics in public discussions and politics in Germany. Problems with the energy supply resonate in our society because they affect everyone through increases in energy costs and restrictions of energy consumption. Such “energy crises” are usually caused by limitations of energy resources, e.g. during the oil crisis in the 1970s. A further, important aspect in classifying an energy supply is its influence on the natural environment, like greenhouse gas emissions, waste production, and safety risks. In Germany, many different options for future energy supplies are studied. Most of these are in the field of “renewable” energies, which are understood to be environmentally friendly, but there are also other promising alternatives to currently used concepts. This thesis is focused on one of these alternatives.

Light atoms, for instance deuterium and tritium, both hydrogen isotopes, represent an energy resource with low greenhouse gas emissions, high and long-lasting availability and low safety risks. While a chemical process is responsible for the release of energy from fossil fuels, a nuclear process can make energy accessible from light atoms, as does the ongoing process in the sun – thermonuclear fusion. The basic physical process for fusion derives from the strong nuclear force following the principle of minimum total potential energy. Motivated by Einstein’s mass-energy equivalence [1], Weizsäcker and Bethe explained the possibility of obtaining net energy by fusing light or fissioning heavy nuclei [2, 3]. With respect to mass, the iron nuclide separates the region of nuclei usable for fusion from the region of nuclei which can be used for fission to obtain positive net energy.

Net energy can theoretically be gained through fusion reactions of several different nuclei. The fusion of deuterium and tritium has been found to be the most efficient for human-built fusion reactors (for further details see chapter 1.2 of reference [4]). A deuterium-tritium fusion reaction gives a net energy gain of 17.6 MeV obtained as kinetic energy. Most of this energy

1. Introduction

is carried by the neutron; a remaining 3.5 MeV is carried by the He-nuclide. Fusion reactions only happen under certain, special conditions. Due to the positive charge of nuclei, they feel the repulsive Coulomb force. This repulsive Coulomb force superposed with the strong nuclear force forms the Coulomb barrier. The nuclei have to pass this electrostatic barrier to undergo fusion. Relying on classical theory, the nuclei need a very high energy to pass the Coulomb barrier. However, a quantum mechanical phenomenon, known as quantum tunnelling, explains that it is possible for the nuclei to tunnel through the barrier, i.e. lower energies are sufficient to pass the barrier and fuse. Still, this happens with a very low probability. Therefore, thermonuclear fusion, involving many collisions between particles, seems to be the only applicable technique for obtaining an efficient fusion rate for a human-built reactor.

Heating a hydrogen gas to a very high temperature leads to the ionization of the gas atoms, and the gas turns into a plasma that contains mainly electrons and nuclei. A dense, high-temperature plasma ensures that a large number of nuclei at necessary energies are available and a process with a very low probability like quantum tunnelling can take place at a sufficient rate. John D. Lawson derived a criterion for a burning thermonuclear fusion plasma [5]. The triple product of density n , energy confinement time τ_E , and plasma temperature T (measured in kinetic energy) has to be greater than a specific value for the ignition of a fusion reactor

$$n\tau_E T > 5 \times 10^{21} \text{ keV s m}^{-3}. \quad (1.1)$$

In other words, the challenge is to confine the energy of a high-temperature, high-density plasma for sufficient time for the plasma to ignite. Ignition means that no external plasma heating is required to sustain the fusion reactions. However, even with a remaining externally supplied heating power, P_h , a net energy gain, $Q = P_f/P_h > 1$, can be achieved, with P_f being the fusion power. On the sun, the confinement of the plasma particles is based on the gravitational force. However, machines based on that principle cannot be built on Earth. Therefore, many different technologies have been studied in the past six decades, mostly relying on inertial or magnetic confinement. The main focus has been on magnetic confinement. The plasma can be confined by magnetic fields because of the charge of its particles. Due to the Lorentz force, a charged particle follows magnetic field lines. The movement along a field line is superposed by a gyration around it. Toroidally shaped,

magnetic confinement devices have the most promising layout. Two main concepts exist: the tokamak and the stellarator.

The tokamak concept was proposed by the Soviet nuclear physicists Andrei D. Sakharov and Igor Y. Tamm in 1952. Two magnetic field systems are used to confine the hot plasma. The main magnetic field is produced by toroidal field coils. A second, poloidal magnetic field is generated via a toroidal current in the plasma, usually using a transformer with the plasma itself as the secondary winding. The combination of both fields results in a twisted magnetic field. Such a twisted magnetic field is necessary to compensate effects due to plasma drifts and balance the plasma pressure. Additional vertical field coils are needed for the position and shape control of the plasma. The stellarator concept is a combination of the two main magnetic coil systems of a tokamak in one coil system that directly produces twisted magnetic field lines, without a net current flow in the plasma. It was proposed by the American physicist Lyman Spitzer in 1951. In the early years of fusion research, it was technically simpler to build devices based on the tokamak concept. Therefore, most of today's fusion devices are tokamaks [6–14], but interesting stellarator projects are in progress [15, 16].

The first tokamaks were built in a limiter configuration where the first wall of the vessel is protected by heat-resistant plates that stop plasma particles outside of a defined maximum minor radius $r = a$. These heat resistant plates are called a limiter, and by their position, the last closed flux surface (LCFS) of the magnetic field is defined. The region beyond this is the scrape-off layer (SOL). At the LCFS, the confined plasma is separated from the non-confined plasma; therefore, the mathematical term separatrix is sometimes used for it, see a sketch of the poloidal cross-section of the Tokamak Experiment for Technology-Oriented Research (TEXTOR) in figure 1.1 (left). An important aspect is the impurity content in the plasma: particles from the wall materials which enter the plasma and reduce the plasma temperature and energy confinement. Initially planned to reduce the number of impurity particles, a divertor concept was developed which finally lead to another key observation (see below). In the divertor configuration, additional magnetic fields are applied at a specific location to move the plasma strike-zone far away from the confined plasma. Due to the additional magnetic fields, magnetic X-points are formed at the position on the separatrix where the poloidal magnetic field vanishes (figure 1.1 (right), set-up of the Joint European Torus (JET)). At present, all large tokamaks have

1. Introduction

a divertor. In addition, most of the tokamaks have an elongated poloidal shape as this brings further advantages in the energy confinement time.

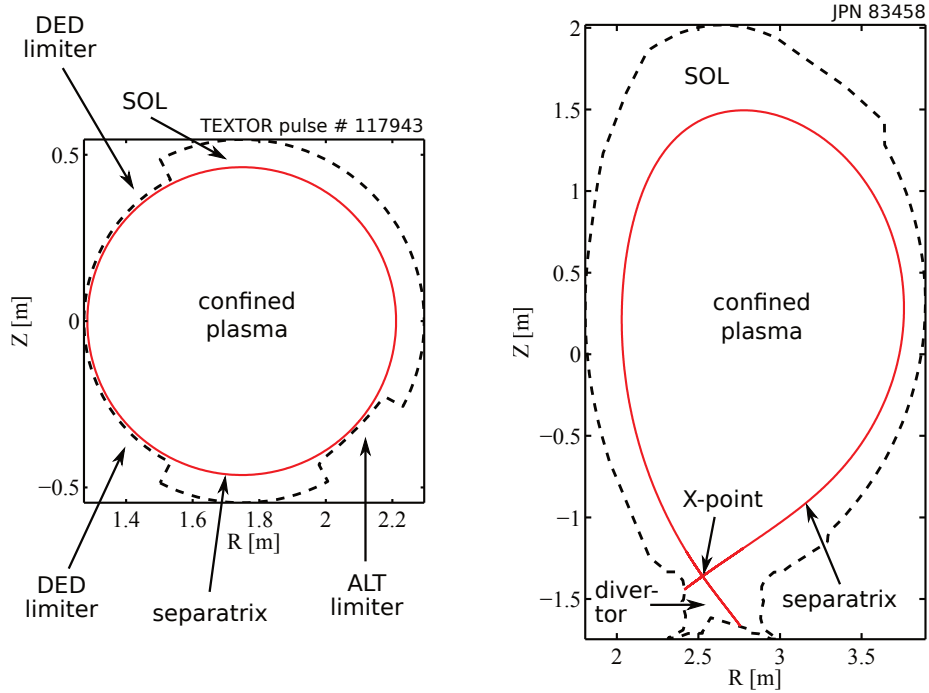


Figure 1.1.: Poloidal cross-sections of the limiter tokamak TEXTOR (left) and the divertor tokamak JET (right).

The Axially Symmetric Divertor EXperiment (ASDEX), a tokamak located in Garching, Germany, was the first to make use of the divertor configuration. In 1982, an important observation was made at ASDEX which highlights the major advantage of a divertor over a limiter. At sufficiently high plasma heating, a high-confinement mode (H-mode) was found [17–19]. Energy confinement time in H-mode is doubled compared to the formerly known low-confinement mode (L-mode). H-mode is mainly observed at high plasma heating on devices with divertors and is much less pronounced on limiter machines. The increased energy confinement time is a result of a strong transport barrier located at the plasma edge due to which a large pressure gradient builds up, the so-called edge pedestal. Today, this is the operational scenario foreseen for the next-generation tokamak experiment,

ITER [20], and for future tokamak-based fusion power plants.

Aside from the many technological difficulties, there are unsolved issues in the physical understanding of processes in a magnetic confinement device. The focus of this work is on transient, high wall loads due to edge localized modes (ELMs), and furthermore on controlling this plasma edge instability by usage of additional magnetic perturbations. ELMs appear during plasma operation in H-mode and were found together with the H-mode on ASDEX [19]. They result in pulsed, repeating losses of particles and energy to the plasma-facing components, mainly in the divertor. Many types of ELMs are known, differing in the dependence of repetition rate and strength on parameters like the heating power. The most severe ones are of “type I”, the large ELMs. In today’s tokamaks like JET, their heat flux to the divertor easily reaches several hundred MW m^{-2} [21]. Although their heat pulses only last for very short times of a few ms, this is a severe problem for the wall material. As a comparison, the re-entry of a space shuttle causes a heat load of about 10 MW m^{-2} on the protection tiles, which is currently the material limit for steady-state heat loads. Such a value is also considered for future fusion devices in steady-state operation. The reader is referred to [22–24] for more details on ELMs themselves.

Different mitigation methods for ELMs are currently studied [25], all aiming for an increase of the repetition rate of ELMs, expecting a corresponding reduction in the energy loss per ELM. The application of resonant magnetic perturbations (RMPs) is one possible solution, and currently the most promising one. Although successful usage has been demonstrated, the understanding of the physics involved lacks in many aspects.

This cumulative dissertation is structured as follows: Chapter 2 gives the reader an overview on what RMPs are, describes existing approaches of producing them, and discusses the current understanding of the effects on the confined fusion plasma. Within that chapter, the general scientific context of the publications in this dissertation is presented. The essence of the publications is presented in chapters 3 to 5. Each of the chapters focuses on a specific aspect of RMP physics. The key questions investigated are:

- What is the impact of RMPs on ELM energy deposition? (chapter 3)
- Are there alternative methods for applying RMPs? (chapter 4)

1. Introduction

- Do RMPs have a negative effect on the fast ion confinement and therefore the performance of a fusion plasma? (chapter 5)

Finally, chapter 6 concludes the results of this dissertation.

2. Resonant magnetic perturbations

Magnetic perturbations which are resonant with field lines in the plasma are known as resonant magnetic perturbations (RMPs). The resonance condition is fulfilled when the inverse winding number of the field lines, in tokamak physics known as the safety-factor

$$q = \frac{1}{2\pi} \oint \frac{1}{R} \frac{B_t}{B_p} ds, \quad (2.1)$$

corresponds to the ratio of the applied poloidal m and toroidal n perturbation mode numbers:

$$q \stackrel{!}{=} \frac{m}{n}. \quad (2.2)$$

R is the major radius of the torus, B_t and B_p the toroidal and poloidal magnetic field components, and ds the line element in the poloidal plane. The term RMP is mostly used if the perturbation is deliberately applied. In a magnetic confinement device, several resonance conditions are usually fulfilled due to the continuous q -profile. As will be seen below, the key resonant perturbations are those in the edge region of the plasma near the separatrix.

2.1. Methods of producing resonant magnetic perturbations

A standard technique for producing such RMPs is the usage of external coil-systems with a certain geometry to apply the required poloidal and toroidal mode numbers. The main focus is often on low toroidal mode numbers, usually in the range of 1 to 4. Although the general idea is always the same, the design of such RMP coil systems differs a lot from device to device.

2. RMPs

Originally designed to suppress the intrinsic error field of misaligned toroidal field coils, some devices like JET use large error field correction coils (EFCCs) which are located outside of the vacuum vessel [26] to apply RMPs, see figure 2.1. As a consequence of the large distance between the coils and the plasma edge, a strong current of several tens of kA is required to achieve an adequate perturbation of the plasma edge using such EFCCs.

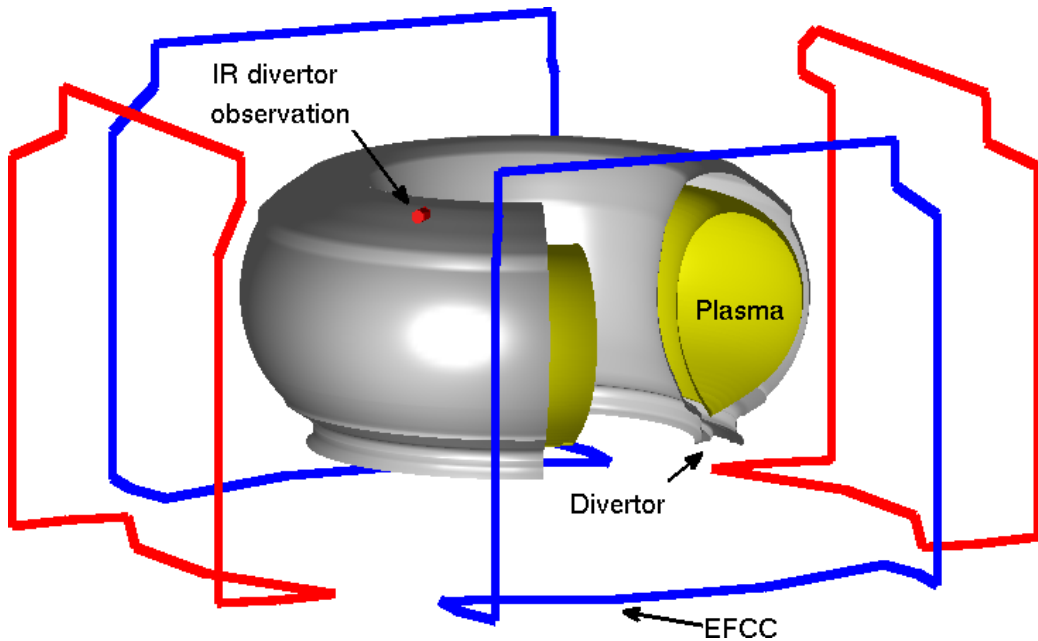


Figure 2.1.: Sketch of an experimental set-up for EFCC experiments on JET. The colours of the EFCCs indicate different current flow directions, here shown for perturbations with toroidal mode number $n = 2$. On top of the machine, an infra-red (IR) camera for the divertor observation (red) is shown. This camera is viewing the divertor at the bottom of the machine.

The EFCCs at JET are designed to apply perturbations with toroidal mode numbers of either $n = 1$ or $n = 2$, which defines the number of required coils. In figure 2.1, the different colours indicate different current flow directions to create $n = 2$ perturbations as used for the experiments discussed in [27, 28] (chapter 3). An alternative is the usage of much smaller, also rectangular, coils which are inside the vessel and therefore very close to the plasma. This approach has been studied intensively on the DIII-D tokamak and is now also

2.1. Methods of producing RMPs

used on ASDEX Upgrade (AUG) [29]. It enables the usage of smaller currents (only a few kA) while still achieving a comparably strong perturbation of the plasma edge.

Another approach is the usage of helical, internal coils. In contrast to the previously discussed principle, the coils are aligned parallel to field lines with a defined q . It is possible to change the poloidal and toroidal perturbation mode numbers while keeping the ratio constant by changing the current flow direction in the different wires. Such a coil system aligned to $q = 3$ was used on TEXTOR, referred to as the dynamic ergodic divertor (DED) [30, 31].

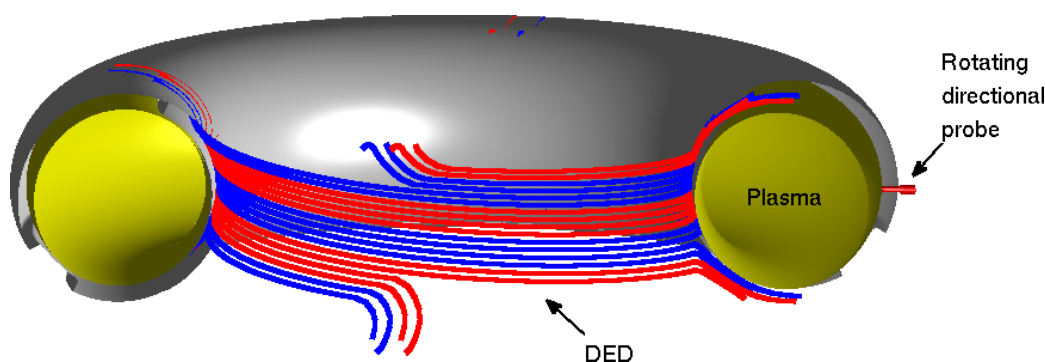


Figure 2.2.: Sketch of the TEXTOR geometry with the helical DED coils located on the inner side. On the outer side, the rotating directional probe (red) is shown at its measurement position in the SOL.

Figure 2.2 shows the DED, which is located at the high-field side (HFS) of TEXTOR. The colours of the wires indicate the different current flow directions for a perturbation with $m/n = 6/2$. A special feature of the DED at TEXTOR is the ability to rotate the perturbation fields at various frequencies and in different directions. By doing this, the effects of dynamic perturbations on the plasma can be studied. Studies of the effects of such perturbations on the losses of fast ions are discussed in [32] (chapter 5).

One aspect of this thesis is to show that such perturbations produced by helical currents can also be applied using lower hybrid waves (LHWs) [33] (chapter 4). An advantage of wave-induced currents is the improved flexibility compared to a hard-wired coil system with a fixed pitch angle. The wave-induced currents flow along SOL field lines and follow changes in the magnetic topology. Therefore, such currents are always kept in resonance

2. RMPs

with the plasma edge. The toroidal perturbation mode number is defined by the number of available LHW guides at different toroidal locations. At the Experimental Advanced Superconducting Tokamak (EAST), this approach has been experimentally demonstrated [34, 35].

2.2. Modification of the magnetic topology

The application of RMPs results in the reorganization of the magnetic topology into a new equilibrium state. The non-axisymmetric fields cause a deformation of the plasma boundary, and their resonances inside the plasma lead to internal kinking and magnetic reconnection processes, also known as tearing. Due to this reconnection, magnetic islands are created on surfaces at locations with a q in resonance. On those flux surfaces, groups of islands form which correspond in the number of islands in the poloidal and toroidal directions with the poloidal and toroidal mode numbers of the resonance at that location.

One method of visualizing the changes in the magnetic topology is a Poincaré plot. The simplest approach to model effects of RMPs on the plasma is to superpose the axisymmetric equilibrium field with the additional perturbation field. This is a vacuum approach as no plasma is considered, although the field produced by the toroidal plasma current is included. Knowing the total magnetic field $\vec{B} = (B_R, B_\varphi, B_Z)$, the field lines can be traced based on the equations

$$\frac{dR}{d\varphi} = R \frac{B_R}{B_\varphi}, \quad (2.3)$$

$$\frac{dZ}{d\varphi} = R \frac{B_Z}{B_\varphi}. \quad (2.4)$$

The crossing points of the field lines with the poloidal cross-section at a fixed toroidal angle φ generate the Poincaré plot.

Figure 2.3 shows such Poincaré plots originating from vacuum modelling for EAST. On the left, the reference case without RMPs is shown. Within the separatrix (red line), nested flux surfaces (blue ellipses) can be seen. On each of these flux surfaces, one field line was started and followed for 3000 toroidal turns. On the right, a case with RMPs is shown. The RMPs are created by LHW-induced helical currents in the SOL as discussed above.

2.2. Modification of the magnetic topology

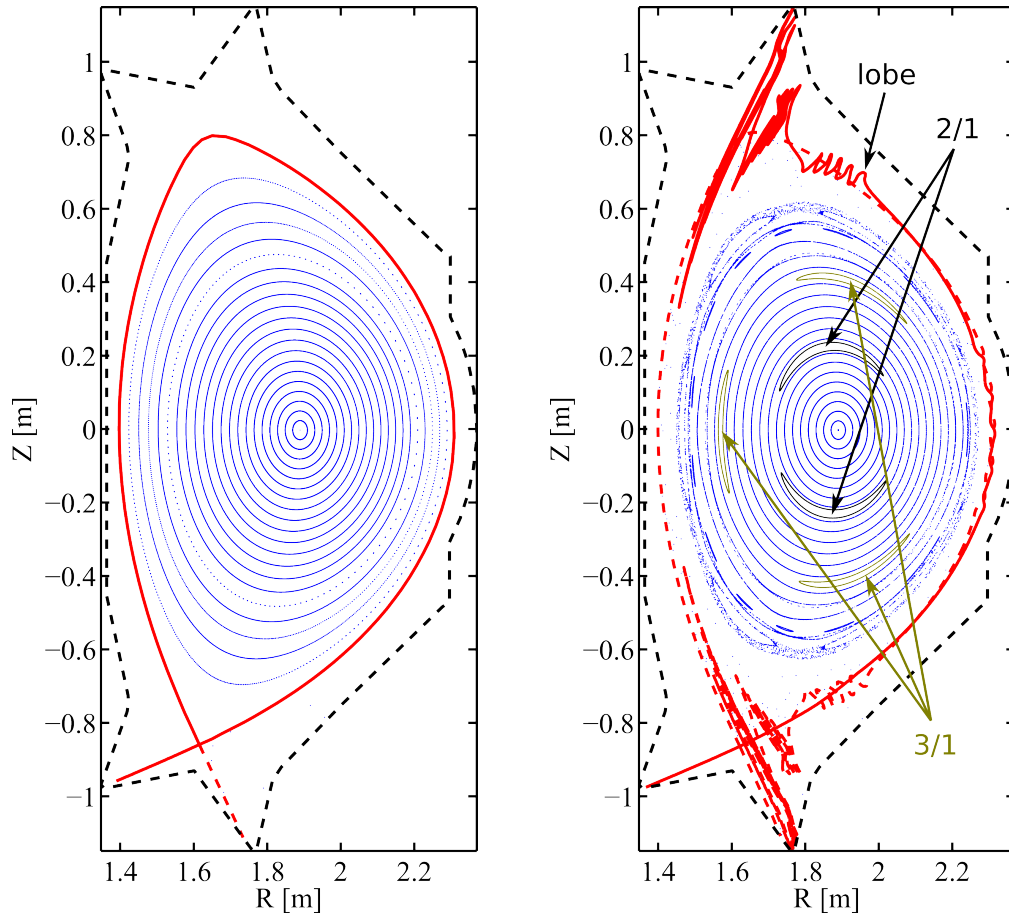


Figure 2.3.: Poincaré plots of the magnetic topology in EAST based on an equilibrium for pulse number 29 100 at 3.5 s. The unperturbed equilibrium is shown on the left and a case with additional perturbations on the right. Two chains of magnetic islands at different rational surfaces are highlighted. The intersection of the stable (red, solid) and unstable (red, dashed) manifolds creates lobe-like structures.

2. RMPs

Here, a current of 0.5 kA equally distributed across five current filaments with a distance of 1 cm from the separatrix is applied. In the core region, most of the flux surfaces remain nearly unchanged, but two island chains are clearly created. The islands are located at $q = 2$ and $q = 3$. The applied perturbation has a dominant toroidal mode number of $n = 1$. This is why we see the creation of 2/1 and 3/1 island chains; both of them are formed by tracing only one field line each. Further outside at the plasma edge, we observe a much stronger modification of the Poincaré plot. Some more island chains are created, containing small and large islands. Furthermore, a stochastic region is formed, seen by the dots that do not set up a surface or island but cover a larger radially extended region. Focusing on the separatrix, we also observe a strong deformation. The separatrix splits into a stable (red, solid) and an unstable (red, dashed) manifold [36] which form the boundary between the confined plasma and the SOL. The intersections of the two separatrix manifolds form lobe-like structures which become longer if located closer to the X-point. On the divertor targets, this appears as a splitting of the strike-line, causing a redistribution of the energy deposition. Previously untouched regions of the wall can come into contact with the plasma at these locations.

RMP physics is focused on the plasma edge of magnetic confinement devices. In that region, the effective perturbation (the perturbation field normalized by the toroidal field, see equations (2.3) and (2.4)) is aimed to be highest to achieve a strong stochastization. Within the stochastic region, the radial transport is enhanced, which changes the plasma parameters [37–40] and may explain experimental observations like the heat redistribution [41], modification of the edge electric field [42, 43], and the control of edge instabilities [44–46].

Within the last decade, it has become clear that the magnetic topology of a plasma in a tokamak cannot fully be described by the simple vacuum approach. Especially, during the plasma operation in H-mode, additional currents exist in the plasma or are created as a response of the plasma to the applied external RMP fields. Many studies [47–51] have shown that these plasma responses need to be considered in order to understand the ongoing processes in a tokamak plasma in the presence of RMPs. The two main effects discussed are RMP field screening and resonant field amplification. In addition, particle drifts in H-mode operation appear to have a strong influence [52]. Different ideas to improve the vacuum approach are discussed [52–

54] and new methods based on kinetic [55] and fluid modelling used [56–58]. All these improved modelling approaches show an impact on the magnetic topology in the edge and core regions leading to modified plasma transport.

2.3. Effects on edge localized modes

ELMs can lead to a severe problem for plasma-facing components due to high energy fluences that they are exposed to, as mentioned in chapter 1. Within the last decade, it has been shown that the energy loss per ELM can be controlled by the application of RMPs [49, 59–61]. While decreasing the energy loss of each ELM, an increase in the ELM frequency is observed, which keeps the total energy lost over time constant [62]. Initial ideas held the stochastization of the plasma edge directly responsible for the increased thermal and particle losses which reduce the energy loss of a single ELM. Other interpretations do require an external kinking of the plasma edge to explain the increased ELM frequency [63]. The currently most accepted explanation is based on the influence of the RMP on the stability of the edge instability via stochastization as well as internal and external kinking and many accompanied effects of RMPs on the plasma parameters [64–66].

Up to now, a common understanding of ELM control with RMPs has not been achieved. Experiments on the DIII-D tokamak show a resonant window (certain edge safety-factor range) for which complete suppression of the large edge instabilities is seen [67]. Elsewhere, on JET and AUG, such a resonant window is not found [60, 61]. In contrast, on JET, a multi-resonance effect has been observed [46] whereby the ELM frequency strongly depends on the edge safety-factor. The experiments on AUG instead show a strong dependence on the edge density: suppression of large ELMs appears to have an edge density threshold. The edge density affects the collisionality of the edge plasma, which is an important parameter in RMP physics.

The loss of confined energy gives a measure for the ELM size, but this is not the crucial parameter for determining the impact on plasma-facing components. Aside from convection to the target, radiation is a further loss channel which needs to be considered; RMPs can affect both channels. Within this dissertation, the energy arriving on the target is considered. If the effects on the energy loss and frequency of ELMs are considered to be macroscopic, this work focuses on microscopic effects which are seen in the

2. RMPs

heat flux profile of an ELM pulse on the target. By doing so, detailed structures can be observed and compared with macroscopic observations to gain a more complete picture of the ongoing processes when applying RMPs for controlling ELMs. The effects on the heat flux profiles are studied by means of infra-red thermography with fast cameras viewing the outer divertor from top of the machine, see figure 2.1. The study of ELM heat load deposition using fast infra-red cameras allows a two-dimensional view of the deposition process, resolved in time and space along the radial axis. On many devices, this has become a standard technique for studying energy deposition due to ELMs [68–70]. It strongly contributed to the understanding of the ELM via the observation of the natural stochasticization [68], the study of its toroidal mode number [71], and the finding of filamentation [70].

Observations of the ELM heat load deposition during RMP application show a controlled splitting of the deposition profile [72]. Recalling the discussions about RMP effects on the topology, this appears not to be surprising as strike-line splitting is expected, when applying RMPs. However, splitting in the heat load deposition is only observed during the major ELM energy loss but not in the phases between ELM pulses. This is understood as a consequence of the plasma response: screening of the RMP field suppresses the splitting. Within this work, it is studied whether the observed splitting of the heat load deposition of an ELM behaves as predicted by the vacuum model or needs consideration of further physical processes to be understood [28] (section 3.2). Furthermore, the first evidence is presented that RMPs also affect processes during the ELM itself seen on a long time-scale of up to 5 ms before the major ELM energy deposition appears [27] (section 3.1).

2.4. Drawback: degradation of the fast ion confinement?

The confinement of high-energy fusion-born He-nuclei is an important aspect for a self-sustaining burning fusion plasma. In the last two decades, it has become clear that due to perturbations with high toroidal mode numbers as caused by the ripple of the toroidal field fast ion losses are enhanced [73]. This leads to a loss of He-nuclei before they had a chance to thermalize and contribute to the plasma heating. Such an energy sink is a critical aspect for

2.4. Drawback: degradation of the fast ion confinement?

a fusion reactor: it reduces the plasma heating and increases the wall loads. A key aspect for RMP physics is whether these losses can also appear due to perturbations with lower toroidal mode numbers. Simple models predict such enhanced losses due to RMPs [74–76]. However, up to now, these models have used the vacuum assumption and miss the important contribution of the plasma response, which will affect the results as discussed before. Whether the plasma response will reduce or enhance the losses is difficult to predict without performing improved modelling.

In terms of observations from RMP experiments, the research in this field is still in its infancy. In current RMP experiments, mostly beam-induced fast ions are studied, which means that either hydrogen or deuterium ions at much lower energies than fusion-born He-nuclei are used. Some experiments measure enhanced losses at one toroidal location and reduced losses at another, whereas other experiments detect increasing losses only with strong resonance of the perturbations in the edge [77, 78]. Equipped with the DED, TEXTOR provides a large variety of magnetic perturbations to study their effect on the fast ions. For the measurement of fast ion losses at TEXTOR, a rotating directional probe [79] (section 5.1) is used, see figure 2.2. The probe is inserted from the low-field side (LFS) into the SOL for measuring co- and counter-going ions, and the amount of fast ions is determined from the difference between the two directions. This allows for the detection of fast ion losses along a radial profile covering the whole SOL at TEXTOR. In agreement with previous observations, it is shown that a clear influence on the fast ion losses is only seen at strong resonance [32] (section 5.2).

3. Effects of resonant magnetic perturbations on the distribution of heat loads due to edge localized modes

Over the last decade, the macroscopic effects of RMPs on ELMs have been studied in detail and theories to explain their effects have been developed. However, a full understanding has not yet been achieved. Especially, the study of the actual influence on the target energy deposition was restricted due to mechanical issues in the past. After a significant improvement of the infra-red viewing systems of the world's largest tokamak JET, this important aspect can now be studied.

3.1. Dynamic structures prior to an edge localized mode crash

As part of this dissertation, an extensive view into the dynamic ELM process during application of RMPs has been achieved. Dynamic structures are found to appear before the ELM energy deposition and have been observed to have an effect on it [27]. The observation of such structures prior to an ELM crash has never been reported before. In the following, a detailed summary of the study is presented:

Applying RMP fields above a certain strength (at JET: $I_{\text{EFCC}} > 2.5$ kA ($\times 16$ turns), in $n = 2$ configuration) leads to a significant modification of the heat deposition on the outer divertor target. Several ms before the major energy deposition of an ELM appears, structures propagating radially outward are seen. These structures form either near the original strike-line

3. Effects of RMPs on the distribution of heat loads due to ELMs

or at a distance of up to several cm away from it, depending on the plasma configuration. The distance depends on the magnetic topology, experimentally controlled by the edge safety-factor. Additionally, the propagation speed of the structures is found to be altered at different edge safety-factors. A relatively slow propagation between 7 m s^{-1} to 20 m s^{-1} is observed.

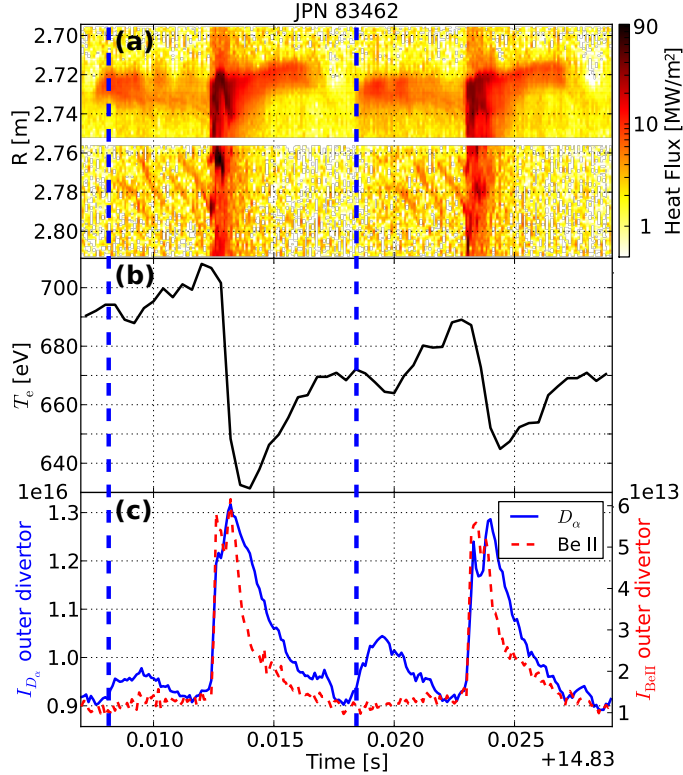


Figure 3.1.: Two ELM crashes during the application of RMPs are shown: time-traces of the heat flux profile on the outer divertor target (a), electron temperature at the plasma edge (b), and intensity of the D_α and Be II emission light (c). Reprinted with permission from [27]. Copyright 2014, Euratom.

These structures appear as several parallel lines in the heat flux profile and propagate until the major energy deposition of the ELM reaches the target, see figure 3.1 (a). The ELM deposition profile shows increased heat fluxes at the locations of the structures, which indicate that these pre-ELM structures directly affect the final ELM heat deposition. In some cases, a

3.1. Dynamic structures prior to an ELM crash

few of the structures even seem to continue to propagate during the major ELM energy deposition on the target, causing large heat fluxes.

A statistical analysis of the creation time of the pre-ELM structures with respect to the major energy deposition of the ELM gives a time delay of about 3 ms. This is much longer than any ELM time-scale known before. Due to this long delay it appears impossible to understand the pre-ELM structures as rotating ELM filaments, which are reported to have a fast radial motion from 0.5 km s^{-1} to 2 km s^{-1} [80] and therefore much shorter lifetimes. However, ELM filaments in the presence of RMPs are rarely studied and their involvement cannot be fully excluded. A possible slowing-down of the filament's rotation due to RMPs has not yet been investigated.

The pre-ELM structures are also accompanied by additional effects shown through different plasma parameters. There is a drop in the edge electron temperature when the pre-ELM structures are created (figure 3.1 (b)). This drop recovers while the pre-ELM structures are propagating until the ELM crash appears, which strongly reduces the edge electron temperature. In addition, there is an increase in the ion influx (seen via the D_α signal) when the pre-ELM structures are created, which also disappears after a short period, see figure 3.1 (c). In contrast, the Be II light emission from the divertor target does not show such an increase when the pre-ELM structures are created. The Be II light is only emitted during the ELM crash itself. These experimental observations are a strong indication of the origin of the heat flux creating the pre-ELM structures. High-energy particles would also cause the Be II signal to peak, which is not the case. Therefore, only low-energy particles seem to be involved in this process.

A probable explanation for the observations is a reconnection process which leads to the formation of the observed structures. The stochasticization of the plasma edge, caused by the reconnection process, would lead to the loss of fast electrons, seen by the drop in electron temperature and the increased D_α signal with no effect on the Be II emission. Furthermore, the loss of electrons can start a self-amplification process of thermoelectric currents as suggested by Evans [81], which finally results in the ELM crash. For testing this hypothesis, the thermoelectric current model [82, 83] has been applied and compared to the experimental data. A good qualitative agreement was found, which further supports the hypothesis. In the next step, measurements of the thermoelectric currents are required; but those are beyond the capabilities of JET and need to be performed elsewhere, such as at

3. Effects of RMPs on the distribution of heat loads due to ELMs

AUG.

This new finding strongly extends the understanding of ELM control by RMPs: although RMPs lead to an increased ELM frequency, some processes occur which are very slow compared to ELM time-scales. It appears that due to the RMPs, different processes decouple. Future experimental results on other devices will allow further understanding by studying this effect under conditions that are not achievable on JET. All this contributes to the further development of theories for the understanding of RMP ELM control.

3.2. Heat load splitting during the major energy deposition

The recent experiments with RMPs on JET enabled the further study of the previously found heat load splitting, during the ELM crash, on the DIII-D tokamak [72]. It is observed that theoretical predictions made, based on the DIII-D results, do not hold for the findings on JET and need further refinement. The experimental study and its theoretical explanation [28] performed as a part of this dissertation are summarized below:

Uncontrolled type-I ELMs show a random heat deposition on the divertor target during their crash [71]. Taking an average over a large number of these ELMs results in a smooth radial decay of the heat load along the target. In contrast, ELMs in the presence of RMPs appear to have radially predefined locations for the heat deposition. If RMPs are applied, the averaged heat deposition profiles, under the same conditions, show preferred heat deposition at distinct radial positions. This distinct heat deposition can be described as splitting during the ELM crash in reference to strike-line splitting during L-mode operation. The structure of the splitting changes when the magnetic topology varies, for instance by a difference in the applied perturbation field or a changed edge safety-factor of the plasma.

At different perturbation amplitudes modifications are observed which can be quantified as a change in the amount of splitting. Three distinct regions of high heat flux are seen at the measurement position for the case with $n = 2$ perturbation fields, see figure 3.2 (left). If the perturbation strength increases by a factor of 7 (solid \rightarrow dashed), the radial distance of the first region from

3.2. Heat load splitting during the major energy deposition

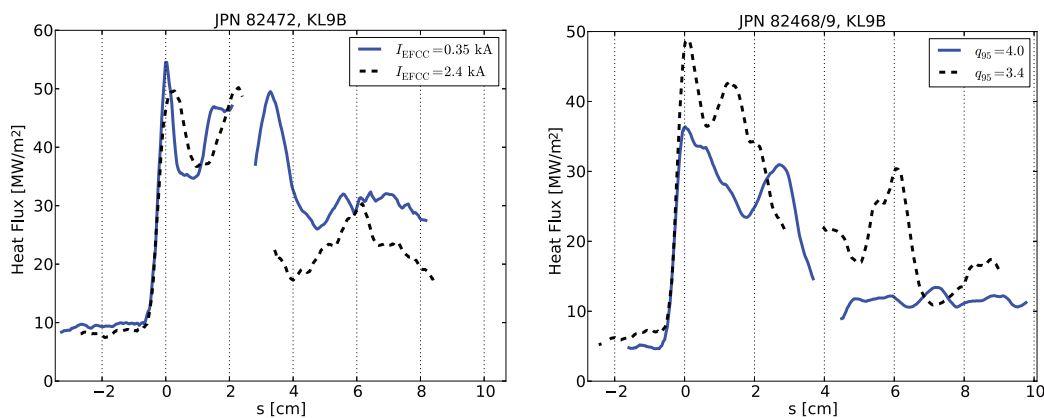


Figure 3.2.: Conditional average of the ELM heat load profile at different perturbation amplitudes (left) and different edge safety-factors (right). Reprinted with permission from [28]. Copyright 2014, Euratom.

the second increases only by a small amount, but the outermost peak is shifted outward by several cm and its amplitude is decreased. Such a change in splitting is not predicted by the vacuum approach if increasing perturbation amplitudes are considered. Instead, the vacuum approach predicts a modification of the amount of splitting, if different edge safety-factors are studied. This trend was experimentally confirmed for the splitting during the ELM heat deposition. A modification of the edge safety-factor by 15% results in a clear change of the splitting by about 1.5 cm, see figure 3.2 (right).

This observed splitting may indicate that the ELM locks to the externally applied perturbations. However, the detailed studies of the time-resolved heat flux profiles show a remaining, slow movement of heat flux structures during the ELM heat deposition. This indicates that the ELMs are not locking to the external perturbations in those experiments, which appears to be in contrast to previous reports [72].

Summarizing the experimental observations, it can be stated that some of the observed features agree with the prediction of the vacuum approach whereas others disagree. For a better understanding, the magnetic topology for two ELM crashes at different perturbation strengths is modelled based on the vacuum approach (see section 2.2) and compared to experimental observations. The predictions indicate the correct trend, but a precise comparison at the measurement location shows a strong discrepancy between

3. Effects of RMPs on the distribution of heat loads due to ELMs

measurement and prediction: a much smaller splitting is predicted than experimentally found.

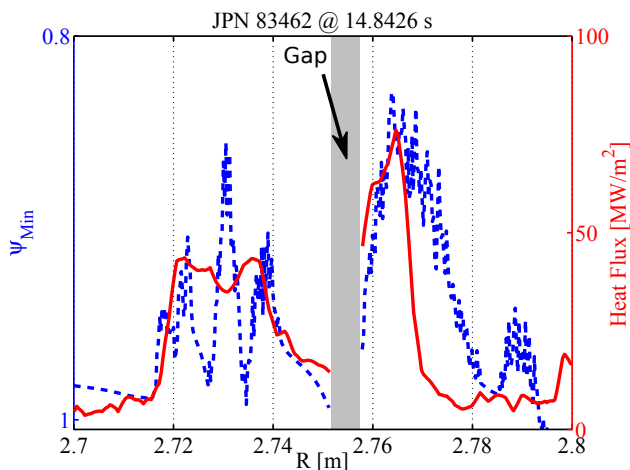


Figure 3.3.: Comparison of the experimental heat flux profile (solid) with the predicted field line penetration depth, $1 - \psi_{\text{Min}}$, of the thermoelectric current model (dashed) during the peak heat deposition of one ELM. Reprinted with permission from [28]. Copyright 2014, Euratom.

Previous publications [82, 83] have demonstrated that consideration of additional thermoelectric currents explains the heat deposition of standard type-I ELM. This provides motivation for also applying the thermoelectric current model to controlled ELMs in the presence of RMP fields. Application of this extended model results in a good qualitative agreement between the experiment and predictions, see figure 3.3. For a quantitative comparison more advanced plasma transport models need to be considered, which is beyond the scope of this work.

One remaining question is: why is different behaviour seen for the experiments on DIII-D and JET? The essential difference between the experiments performed at DIII-D and those at JET discussed here, is the collisionality of the plasma. The experiments at JET discussed here have a three times higher electron collisionality at the pedestal. This seems to lead to the involvement of further physical processes, meaning the experimental findings can not longer be explained using the simple vacuum approach.

These findings are of high importance for future experiments at larger

3.2. Heat load splitting during the major energy deposition

devices where much higher heat fluxes are expected to the targets. Due to the fact that a much larger strike-line splitting is observed than initially predicted by the simple vacuum approach, severe damage can occur if regions which are not prepared for such heat loads come into contact with the plasma. Therefore, it is crucial to consider an improved model – including thermoelectric edge currents – to predict the expected strike-line splitting.

4. An alternative method for applying resonant magnetic perturbations

Experimental observations at EAST show strong evidence that LHWs are able to create RMPs. This is seen through splitting of the outer strike-line and the successful control of ELMs while LHWs are applied [34]. Furthermore, the hypothesis is strengthened by the detection of non-axisymmetric currents, using external pick-up coils. For a further understanding of the features of such wave-induced RMPs, a theoretical study has been performed as a subject of this dissertation [33]. A detailed summary follows:

The LHW-induced RMPs are assumed to create helical current filaments in the SOL, experimentally seen via helical radiation belts. Vacuum modeling (see section 2.2) of magnetic field lines in the SOL confirms that such radiation belts are field-aligned. When field lines are initiated in front of the LHW antenna rows, their traces match the experimentally observed radiation belts, proving that the latter are field-aligned.

In the next step, a current flow along these SOL field lines is considered. The magnetic field generated perturbs the axisymmetric equilibrium and results in a changed magnetic topology (see figure 2.3). This changed magnetic topology shows a splitting of the separatrix into stable and unstable manifolds, confirming the experimentally observed strike-line splitting.

The results of the model depend on four parameters which are studied in detail to gain a quantitative understanding of the physics involved. These parameters are: the amount and direction of current flow, the distance of the current filaments from the LCFS, and the spacing between two helical current filaments. The aim in studying these parameters is also to reduce the number of free parameters by understanding their correlations based on experimental measurements.

4. An alternative method for applying RMPs

It is shown that the amount of current flowing through the helical current filaments affects the degree of stochastization of the plasma edge and the length of lobes created by the intersection of the stable and unstable separatrix manifolds, see figure 4.1. The length of the lobes also affects the strike-line splitting seen on the target. A quantitative study of the relative change in lobe length with current, measured in poloidal flux, shows a non-linear increase in the length. Therefore, simple predictions of the expected lobe length are difficult and a detailed modelling is required.

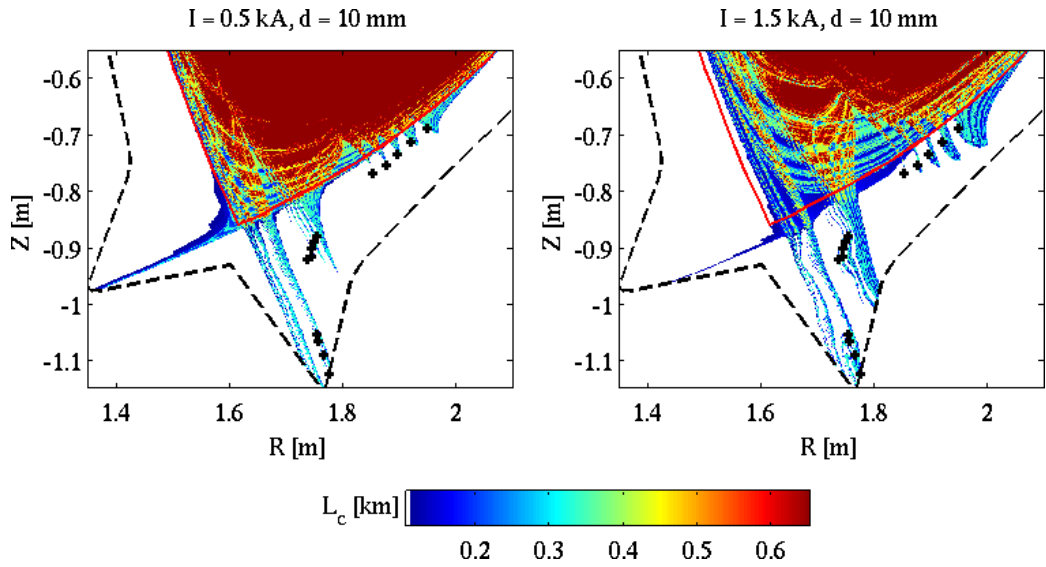


Figure 4.1.: Connection length of the magnetic field lines representing the changes in the magnetic topology depending on the applied perturbation strength: 0.5 kA (left) and 1.5 kA (right). The colour code represents the connection length L_C and the black markers indicate the location of the helical current filaments. The unperturbed separatrix is shown in red. Reprinted with permission from [33]. Copyright 2014, Euratom.

The current flow direction can be measured experimentally, observed in the same direction as the plasma current in the performed experiments. However, one interesting aspect is the behaviour of the strike-line splitting when the current flows in the opposite direction to the plasma current. The model predicts a significant shrinking of the strike-line splitting and the rearrangement of regions which are touched by field lines with a large penetration

depth. These regions with a large penetration depth are expected to show a stronger heat flux deposition than other regions. Therefore, the knowledge of the detailed structure of the strike-line splitting is important for preventing damage during the experiments.

The distance of the current filaments from the LCFS affects both the effective perturbation to the plasma, and the near-field effects on the strike-line splitting. If the helical current filaments are located far from the LCFS, they act as only one filament carrying all the current. Consequently, sub-structures in the footprints vanish and the experimentally expected heat flux appears more localized. This prediction can be understood by calculating the perturbation spectra: the effective perturbation of high poloidal mode numbers strongly decreases if the distance is increased.

The fact that both the current amplitude and the distance of the filaments from the LCFS, have an impact on the effective perturbation indicates that these parameters are not independent. A comparison with experimentally determined fields measured by pick-up coils shows that both are coupled. The dependence can be investigated by comparing the current amplitude to the distance of the filaments from the LCFS while keeping the effective perturbation constant at the same point.

Studying the spacing of helical current filaments shows a similar effect as observed by changing the distance of these from the LCFS. An increased spacing allows the sub-structures in the footprints to become more pronounced and creates a more equal distribution of the heat flux on the target. A perturbation spectrum analyses showed that with an increased spacing, the effective perturbation at higher poloidal mode numbers also increases.

The comparison of model predictions with experimentally measured heat and particle fluxes at different toroidal locations results in qualitative agreement. In conclusion, it can be said that the agreement of the radiation belts with the location of the helical current filaments, the agreement of the measured magnetic signals with the predicted ones, and the agreement in the particle and heat flux profiles strongly support the model assumptions. Consequently, it can be stated that the model correctly describes the underlying physics of LHW-induced RMPs.

The developed model greatly improves the theoretical understanding of the physics of LHW-induced magnetic perturbations. Applying the model to EAST experiments helped to explain the experimentally found splitting [34]

4. An alternative method for applying RMPs

and its relative heat distribution between the different strike-regions in dependence on the ion flux [35]. Using this model, the study of the edge safety-factor dependence of the perturbation spectrum is possible. This demonstrates the outstanding feature of wave-induced RMPs: that they are always resonant with the edge magnetic field, as required for a strong effect on the plasma edge. It makes the LHW-induced RMPs a promising new tool for future devices.

5. A possible drawback of applied resonant magnetic perturbations on the fast ion confinement

5.1. Assessment of a feasible measurement technique

The study of fast ion losses in non-axisymmetric magnetic fusion devices requires suitable diagnostics which can deal with the special conditions. As part of this dissertation, a flexible Langmuir-probe-based diagnostic has been developed and assessed [79]. In the following, the solutions and the features of the diagnostic are summarized:

One important aspect to consider when measuring physical quantities during the application of RMPs is their local variation due to these perturbations. A key role when discussing fast ions is the pitch angle of the field lines which influences the fast ion propagation. As a consequence of the radially dependent safety-factor profile in a tokamak, the pitch angle changes with the radial position and is further perturbed due to the RMP fields. Therefore, a diagnostic for the fast ion loss detection has been developed which diagnoses the correct pitch angle at any radial position in order to measure the physical quantities correctly.

The developed rotating directional probe is based on Langmuir probe arrays, which are biased to a negative voltage for measuring the ion saturation current. The probe head is equipped with two such arrays, facing in opposite directions, see figure 5.1. This is a requirement for being able to measure the fast ion losses because their velocity distribution is non-isotropic. The

5. A possible drawback of applied RMPs on the fast ion confinement

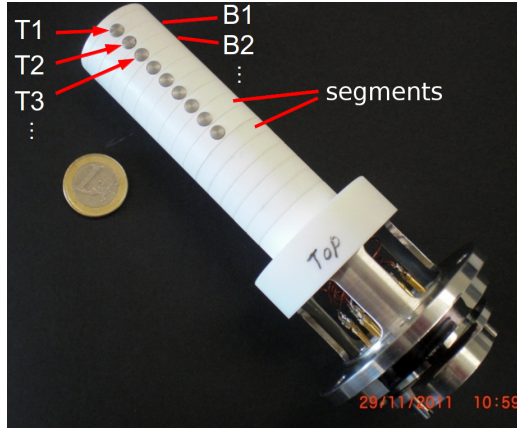


Figure 5.1.: Picture of the probe head showing nine Langmuir probe pins labelled with T1, T2, T3, The same number of Langmuir probe pins are located on the opposite side (B1, B2, . . .). Reprinted with permission from [79]. Copyright 2013, Euratom.

probe head is installed on a fast manipulator; the fast reciprocating probe at TEXTOR. This gives the ability to quickly move the probe into the SOL, rotate, and retract it. The quick movement is needed to reduce the heat load on the probe head and avoid damage. The measurement while rotating is the key feature of the probe as this allows the exact detection of the pitch angle and consequently the correct measurement of the ion saturation current.

The angularly resolved ion saturation current, which is measured by each Langmuir probe, peaks where the particle flux is normal to the Langmuir probe surface. At that angle, the current density from the two opposite facing probe pins can be determined as j_{Co} and j_{Ctr} , with “Co” and “Ctr” giving the flow direction parallel and anti-parallel to the plasma current direction, respectively. Assuming a thermal distributed plasma flow in the SOL without any fast ion losses, both current densities are identical. Having a certain number of fast ions contributing to the total current density measured on one side, this can be detected by taking the difference between the two current densities:

$$j_{loss} = j_{Co} - j_{Ctr} . \quad (5.1)$$

For studying the fast ion behaviour on TEXTOR, neutral beam injection (NBI) is used to introduce ions of up to 50 keV into the plasma. Initial

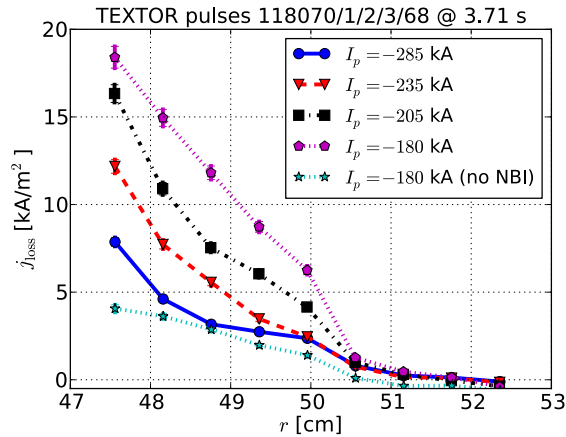


Figure 5.2.: Radial profiles of the ion losses measured for different plasma currents. A reference case without beam induced ions is shown by the stars. Reprinted with permission from [79]. Copyright 2013, Euratom.

experiments using this probe showed a good performance by confirming well known features of fast ion losses without applied RMPs. It is known that the poloidal field produced by the plasma current has a strong impact on the fast ion confinement. At high plasma current the fast ions are well confined, but at low current, they are easily lost. The study of different stages of plasma current shows a clear influence on the detected losses as predicted, see figure 5.2.

Due to the usage of many Langmuir probes along its radial axis, the rotating directional probe allows for a detailed study of the radial decay of fast ion losses. This is seen as a smooth, nearly linear decrease in the outward direction. Furthermore, the availability of time-dependent data from different radial positions enables a radial correlation of the ion saturation signal. The radial correlation can be used to measure the propagation speed in the radial direction of losses or other events in the SOL.

5.2. Experimental results

The correlation of the probe signals from the different radial positions with the signal from the foremost probe pin shows a clear difference in behaviour

5. A possible drawback of applied RMPs on the fast ion confinement

for the measured losses from the co- and counter-directions. The correlation found for the counter-direction has a much larger radial extent. This is a consequence of the losses from beam-induced fast ions, which only occur in the co-direction and impact the radial correlation of the thermal ions. It further supports the suggested measurement method for fast ion losses discussed above.

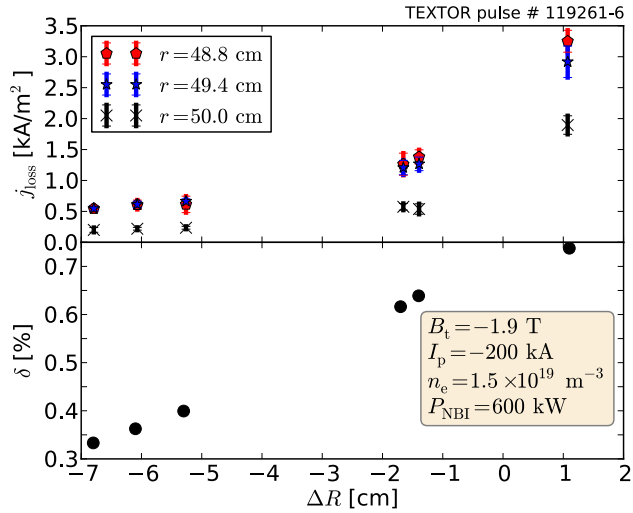


Figure 5.3.: Dependence of the fast ion losses on the plasma position, given as displacement ΔR of the magnetic axis with respect to the geometrical axis. The fast ion losses (top) and the toroidal field ripple (bottom) are shown. Reprinted with permission from [32]. Copyright 2014, IOP Publishing Ltd.

Before studying the influence of RMPs, some basic features of the beam-induced fast ion losses are assessed. These are: the dependence of the number of injected beam particles, the role of the radial plasma position, and the influence of the injection direction. The investigation of different amounts of injected beam particles shows a clear effect on the fast ion losses. For a greater fast ion content in the plasma, stronger losses are detected, which is in line with the general understanding. No clear effect on the fast ion losses can be found if considering different injection directions of the beam ions. Although a small trend for increased losses in a fully co-injected plasma is detected, the losses remain for both injection directions in the co-current direction. As a consequence of the radial decay of the fast ion losses, the

5.2. Experimental results

distance of the probe from the LCFS appears to be an important aspect. Figure 5.3 shows the measurements during a radial position scan of the plasma. Measurements at three distinct locations are plotted against the radial displacement ΔR with respect to the geometrical axis. Additionally, the toroidal field ripple δ seen at the LCFS is plotted. A clear dependence of the detected losses on the radial displacement is found, and at the same time, a strong change of the toroidal field ripple is seen. A simple radial shift of the loss profiles does not explain the differences detected. In addition, the improved fast ion confinement due to the smaller toroidal field ripple needs to be considered.

Many different perturbation modes of the DED have been studied in order to obtain a broad view of the effects of the RMPs on fast ions. These include static and rotating perturbations. Indications are found that ion losses are greatest with static perturbation at the maximum perturbation strength with toroidal mode number $n = 1$. However, such an effect is not verified with $n = 2$ perturbations. The application of rotating perturbations in co- and counter-directions does not show any effect on the losses. Even a study of the high-frequency modulations of the signal does not indicate effects of the rapidly changing perturbation field on the ion losses.

A strong influence on the fast ion losses is found when investigating the edge safety-factor dependence by changing the strength of the toroidal magnetic field, see figure 5.4. A certain scatter is observed in the fast ion losses (grey region) if scanning B_t without applying RMPs but no clear dependence is seen. Once the perturbations are added, the situation changes and a clear drop in the losses is found for $B_t = 1.3 \text{ T}$, which corresponds to a small $q_a \approx 4$. At the same time, an increase in the central plasma rotation from 6.2 kHz to 7.8 kHz is observed. Such an increase in plasma rotation also leads to improved confinement. Considering this, the drop in the fast ion losses appears reasonable, although it is not the only possible explanation. An alternative interpretation is suggested by findings from AUG, where at one toroidal location a strong increase and at another toroidal location a strong drop was observed when applying RMPs.

On TEXTOR, measurements at different toroidal locations to further study the possibility of a toroidal dependence of fast ion losses on RMPs are not possible due to technical limitations. Here, a theoretical study is required in order to gain further understanding. Modelling will also help to qualify the toroidal range seen by the directional probe measurements along

5. A possible drawback of applied RMPs on the fast ion confinement

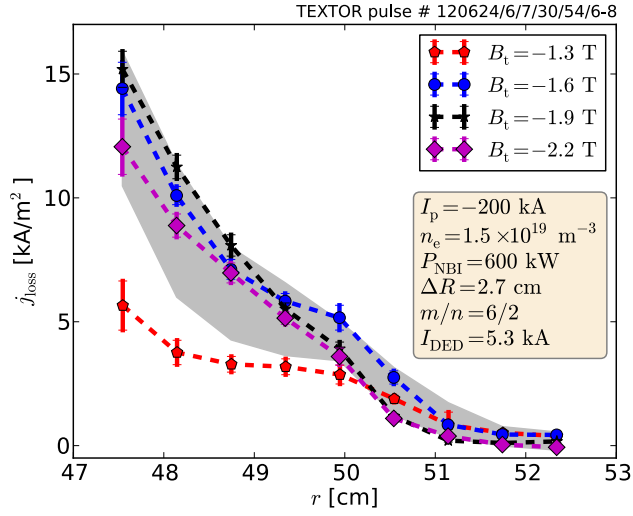


Figure 5.4.: Radial profiles of the ion losses measured for different toroidal fields. The reference cases without RMPs are shown in grey. Reprinted with permission from [32]. Copyright 2014, IOP Publishing Ltd.

the radial profile. A second important aspect is that clear influences are only detected at strong resonances of the RMPs with the plasma edge magnetic field. This is in agreement with findings on another device, K-STAR [77]. There, no effect was seen when the resonance condition in the plasma edge was not met, but strong effects were observed under resonant conditions.

Although more investigations are needed for a full understanding of the involvement of RMPs in the process of fast ion losses, this work [32] is a step towards a better understanding. It is the first and only study providing measurements of fast ion losses in the presents of RMPs on TEXTOR. The results give a good basis for further theoretical studies. Especially, the reduction of the fast ion losses due to RMPs is of high interest for the community and needs further investigations.

6. Conclusions

This thesis focuses on the impact of resonant magnetic perturbations (RMPs) on transient energy losses from plasma edge instabilities, often called edge localized modes (ELMs). This topic is of high importance for the next generation of magnetic confinement fusion devices where strong transient energy losses towards plasma-facing components are expected to cause material damage through overheating or cracking. The use of RMPs is a promising technique for preventing such damage. Furthermore, in this thesis, a new approach for producing such RMPs using electro-magnetic waves is studied theoretically. Finally, motivated by the importance of sufficient fast ion confinement, the influence of RMPs on fast ion losses is investigated.

These studies show that due to RMPs, a process is started early during an ELM which enhances energy and particle transport to the target for a duration much longer than previously known. This process is observed as radially propagating structures in the heat deposition profiles, prior to the major ELM energy deposition. The first evidence presented, shows that the final deposition profile caused by the ELM is formed based on these pre-ELM structures. Modifications to the major ELM heat deposition pattern due to RMPs are studied. They strongly depend on the plasma and perturbation parameters. It is found that these modifications caused by RMPs cannot be explained by a simple vacuum approach. Therefore, a thermoelectric current model, extended for the usage with RMPs, is applied. Predictions of the thermoelectric current model presented in this thesis show a qualitative agreement with the experimental measurements for pre-ELM structures as well as for the major heat deposition of an ELM. This demonstrates the important role of additional currents in the plasma edge during ELMs. For further, quantitative studies, the use of more complex transport models, which also consider cross-field diffusion, is suggested.

The theoretical study of wave-induced RMPs demonstrated their capability of substituting RMPs created by coils. A model predicting the effects of RMPs induced by lower hybrid waves (LHWs) is developed and

6. Conclusions

discussed, and its predictions are compared to experimental studies. Helical currents in the scrape-off layer (SOL) created due to the electro-magnetic waves replace the coils. The model demonstrates the larger flexibility of the wave-induced perturbations compared to current techniques. Perturbation fields created with such an approach are always resonant with flux surfaces in the plasma edge as required for a strong enhancement of the plasma edge transport. This is a consequence of the wave-induced currents as they flow along field lines in the SOL near the plasma edge. These SOL field lines have a similar pitch to the field lines in the plasma edge and therefore are resonant with them. Predictions of the model can explain experimental results from ELM control and heat redistribution studies.

The investigation of the effects of RMPs on fast ion losses at the limiter tokamak TEXTOR does not show significant drawbacks of RMPs. For the purpose of the study, a feasible probe that can deal with the modified topology due to applied RMPs has been assessed and a suitable analysis technique developed. The major improvements of the new probe compared to existing designs are: the simultaneous measurement at different radial locations, and rotation during the measurement, for detecting the correct pitch angle with high accuracy. Over a wide range of perturbation parameters, no effect of RMPs on fast ion losses is seen. In the course of the studies, perturbations with different modes, amplitudes, and rotation frequencies and directions have been applied. It is shown that fast rotating perturbations do not have an additional impact on the fast ion losses compared with static perturbations. Only under conditions with strong resonance in the plasma edge is an impact of the applied static RMPs on the fast ions found, which confirms recently published observations from other devices. In contrast to previous observations, the fast ion confinement appears to be improved due to RMPs.

Bibliography

- [1] A. Einstein. *Ist die Trägheit eines Körpers von seinem Energieinhalt abhängig?* Annalen der Physik **323**, 639–641 (1905).
- [2] C. Weizsäcker. *Zur Theorie der Kernmassen*. Zeitschrift für Physik **96**, 431–458 (1935).
- [3] H. A. Bethe and R. F. Bacher. *Nuclear Physics A. Stationary States of Nuclei*. Reviews of Modern Physics **8**, 82–229 (1936).
- [4] J. Wesson. *Tokamaks*. International Series of Monographs on Physics. OUP Oxford, 2011. ISBN: 9780199592234.
- [5] J. D. Lawson. *Some Criteria for a Power Producing Thermonuclear Reactor*. Proceedings of the Physical Society. Section B **70**, 6–10 (1957).
- [6] E. Bertolini. *JET with a pumped divertor: design, construction, commissioning and first operation*. Fusion Engineering and Design **30**, 53–66 (1995).
- [7] J. Luxon. *A design retrospective of the DIII-D tokamak*. Nuclear Fusion **42**, 614 (2002).
- [8] K. Lackner et al. *Recent results from divertor operation in ASDEX Upgrade*. Plasma Physics and Controlled Fusion **36**, B79 (1994).
- [9] S. Wu. *An overview of the EAST project*. Fusion Engineering and Design **82**, 463–471 (2007).
- [10] Y.-K. Oh et al. *Commissioning and initial operation of KSTAR superconducting tokamak*. Fusion Engineering and Design **84**, 344–350 (2009).
- [11] M. Ono et al. *Exploration of spherical torus physics in the NSTX device*. Nuclear Fusion **40**, 557 (2000).

Bibliography

- [12] A. Barke et al. *The Mega Amp Spherical Tokamak*. In: Fusion Engineering, 1995. SOFE '95. Seeking a New Energy Era., 16th IEEE/NPSS Symposium. Vol. 2. Sept. 1995. Pp. 1456–1459.
- [13] F. Hofmann et al. *Creation and control of variably shaped plasmas in TCV*. Plasma Physics and Controlled Fusion **36**, B277 (1994).
- [14] R. Pánek et al. *Reinstallation of the COMPASS-D tokamak in IPP ASCR*. Czechoslovak Journal of Physics **56**, B125–B137 (2006).
- [15] A. Iiyoshi et al. *Overview of the Large Helical Device project*. Nuclear Fusion **39**, 1245 (1999).
- [16] H.-S. Bosch et al. *Technical challenges in the construction of the steady-state stellarator Wendelstein 7-X*. Nuclear Fusion **53**, 126001 (2013).
- [17] F. Wagner et al. *Regime of Improved Confinement and High Beta in Neutral-Beam-Heated Divertor Discharges of the ASDEX Tokamak*. Physical Review Letters **49**, 1408–1412 (1982).
- [18] M. Keilhacker et al. *Confinement studies in L and H-type ASDEX discharges*. Plasma Physics and Controlled Fusion **26**, 49 (1984).
- [19] ASDEX Team. *The H-mode of ASDEX*. Nuclear Fusion **29**, 1959 (1989).
- [20] B. J. Green, I. I. Team and P. Teams. *ITER: burning plasma physics experiment*. Plasma Physics and Controlled Fusion **45**, 687 (2003).
- [21] B. Sieglin et al. *Power load studies in JET and ASDEX-Upgrade with full-W divertors*. Plasma Physics and Controlled Fusion **55**, 124039 (2013).
- [22] H. Zohm. *Edge localized modes (ELMs)*. Plasma Physics and Controlled Fusion **38**, 105 (1996).
- [23] H. Zohm. *The physics of edge localized modes (ELMs) and their role in power and particle exhaust*. Plasma Physics and Controlled Fusion **38**, 1213 (1996).
- [24] J. W. Connor. *Edge-localized modes - physics and theory*. Plasma Physics and Controlled Fusion **40**, 531 (1998).
- [25] Y. Liang. *Overview of edge-localized mode control in tokamak plasmas*. Fusion Science and Technology **59**, 586–601 (2011).

-
- [26] I. Barlow et al. *The error field correction coils on the JET machine*. Fusion Engineering and Design **58-59**, 189–193 (2001).
- [27] M. Rack, B. Sieglin, T. Eich, J. Pearson, Y. Liang, I. Balboa, S. Jachmich, A. Wingen, S. Pamela and J. E. Contributors. *Findings of pre-ELM structures through the observation of divertor heat load patterns at JET with applied $n = 2$ perturbation fields*. Nuclear Fusion **54**, 072004 (2014).
- [28] M. Rack et al. *Modified heat load deposition of the ELM crash due to $n = 2$ perturbation fields at JET*. Nuclear Fusion **54**, 064012 (2014).
- [29] W. Suttrop et al. *In-vessel saddle coils for MHD control in ASDEX Upgrade*. Fusion Engineering and Design **84**, 290–294 (2009).
- [30] B. Giesen, H. Bohn, W. Huettemann, O. Neubauer, M. Poier and W. Schalt. *Technical lay-out of the dynamic ergodic divertor*. Fusion Engineering and Design **37**, 341–346 (1997).
- [31] O. Neubauer, G. Czymek, K. Finken, B. Giesen, P. Hüttemann, H. Lambertz and J. Schruff. *The dynamic ergodic divertor in TEXTOR – A novel tool for studying magnetic perturbation field effects*. Fusion Engineering and Design **75-79**, 495–498 (2005).
- [32] M. Rack, Y. Liang, P. Denner, J. Pearson, Y. Yang, L. Zeng and the TEXTOR Team. *On the effects of magnetic perturbations on fast ion losses studied at TEXTOR*. submitted to Plasma Physics and Controlled Fusion. (2014).
- [33] M. Rack et al. *Modelling of LHW-induced helical current filaments on EAST: study of an alternative method of applying RMPs*. Nuclear Fusion **54**, 064016 (2014).
- [34] Y. Liang et al. *Magnetic Topology Changes Induced by Lower Hybrid Waves and their Profound Effect on Edge-Localized Modes in the EAST Tokamak*. Physical Review Letters **110**, 235002 (2013).
- [35] J. Li et al. *A long-pulse high-confinement plasma regime in the Experimental Advanced Superconducting Tokamak*. Nature Physics **9**, 817–821 (2013).
- [36] A. Wingen, K. H. Spatschek and S. Abdullaev. *Stochastic Transport of Magnetic Field Lines in the Symmetric Tokamak*. Contributions to Plasma Physics **45**, 500–513 (2005).

Bibliography

- [37] T. Stix. *Plasma transport across a braided magnetic field*. Nuclear Fusion **18**, 353–358 (1978).
- [38] H. Wobig and R. H. Fowler. *The effect of magnetic surface destruction on test particle diffusion in the Wendelstein VII-A stellarator*. Plasma Physics and Controlled Fusion **30**, 721 (1988).
- [39] T. Eich, D. Reiser and K. Finken. *Two dimensional modelling approach to transport properties of the TEXTOR-DED laminar zone*. Nuclear Fusion **40**, 1757 (2000).
- [40] A. Wingen, S. Abdullaev, K. Finken, M. Jakubowski and K. Spatschek. *Influence of stochastic magnetic fields on relativistic electrons*. Nuclear Fusion **46**, 941 (2006).
- [41] M. Jakubowski, S. Abdullaev, K. Finken and the TEXTOR Team. *Modelling of the magnetic field structures and first measurements of heat fluxes for TEXTOR-DED operation*. Nuclear Fusion **44**, S1 (2004).
- [42] S. Jachmich, P. Peleman, M. Van Schoor, Y. Xu, M. Jakubowski, M. Lehnen, B. Schweer and R. Weynants. *First Mach probe measurements of rotation, electric field and particle transport in the DED-ergodized edge plasma of TEXTOR*. In: Proceeding of the 33th EPS Conference on Plasma Physics. O3.014. 2006.
- [43] A. Wingen and K. Spatschek. *Influence of different DED base mode configurations on the radial electric field at the plasma edge of TEXTOR*. Nuclear Fusion **50**, 034009 (2010).
- [44] T. E. Evans et al. *Edge stability and transport control with resonant magnetic perturbations in collisionless tokamak plasmas*. Nature Physics **2**, 419–423 (2006).
- [45] O. Schmitz et al. *Aspects of three dimensional transport for ELM control experiments in ITER-similar shape plasmas at low collisionality in DIII-D*. Plasma Physics and Controlled Fusion **50**, 124029 (2008).
- [46] Y. Liang, C. G. Gimblett, P. K. Browning, P. Devoy, H. R. Koslowski, S. Jachmich, Y. Sun and C. Wiegmann. *Multiresonance Effect in Type-I Edge-Localized Mode Control With Low n Fields on JET*. Physical Review Letters **105**, 065001 (2010).

-
- [47] T. Evans, I. Joseph, R. Moyer, M. Fenstermacher, C. Lasnier and L. Yan. *Experimental and numerical studies of separatrix splitting and magnetic footprints in DIII-D*. Journal of Nuclear Materials **363-365**, 570–574 (2007).
- [48] E. Nardon et al. *Strike-point splitting induced by external magnetic perturbations: Observations on JET and MAST and associated modelling*. Journal of Nuclear Materials **415**, S914–S917 (2011).
- [49] A. Kirk et al. *Magnetic perturbation experiments on MAST L- and H-mode plasmas using internal coils*. Plasma Physics and Controlled Fusion **53**, 065011 (2011).
- [50] Y. Yang, Y. Liang, Y. Sun, T. Zhang, J. Pearson, Y. Xu and TEXTOR Team. *Experimental observations of plasma edge magnetic field response to resonant magnetic perturbation on the TEXTOR Tokamak*. Nuclear Fusion **52**, 074014 (2012).
- [51] P. Denner, Y. Liang, Y. Yang, M. Rack, L. Zeng, J. Pearson, Y. Xu and the TEXTOR Team. *Local measurements of screening currents driven by applied RMPs on TEXTOR*. Nuclear Fusion **54**, 064003 (2014).
- [52] A. Wingen, O. Schmitz, T. E. Evans and K. H. Spatschek. *Heat flux modeling using ion drift effects in DIII-D H-mode plasmas with resonant magnetic perturbations*. Physics of Plasmas **21**, 012509 (2014).
- [53] P. Cahyna and E. Nardon. *Model for screening of resonant magnetic perturbations by plasma in a realistic tokamak geometry and its impact on divertor strike points*. Journal of Nuclear Materials **415**, S927–S931 (2011).
- [54] H. Frerichs, D. Reiter, O. Schmitz, P. Cahyna, T. E. Evans, Y. Feng and E. Nardon. *Impact of screening of resonant magnetic perturbations in three dimensional edge plasma transport simulations for DIII-D*. Physics of Plasmas **19**, 052507 (2012).
- [55] M. F. Heyn, I. B. Ivanov, S. V. Kasilov, W. Kernbichler, I. Joseph, R. A. Moyer and A. M. Runov. *Kinetic estimate of the shielding of resonant magnetic field perturbations by the plasma in DIII-D*. Nuclear Fusion **48**, 024005 (2008).

Bibliography

- [56] M. Bécoulet et al. *Physics of penetration of resonant magnetic perturbations used for Type I edge localized modes suppression in tokamaks*. Nuclear Fusion **49**, 085011 (2009).
- [57] E. Nardon, P. Tamain, M. Bécoulet, G. Huysmans and F. Waelbroeck. *Quasi-linear MHD modelling of H-mode plasma response to resonant magnetic perturbations*. Nuclear Fusion **50**, 034002 (2010).
- [58] A. Wingen, N. Ferraro, M. Shafer, E. Unterberg, T. Evans, D. Hillis and P. Snyder. *Impact of plasma response on plasma displacements in DIII-D during application of external 3D perturbations*. Nuclear Fusion **54**, 064007 (2014).
- [59] T. E. Evans et al. *Suppression of Large Edge-Localized Modes in High-Confinement DIII-D Plasmas with a Stochastic Magnetic Boundary*. Physical Review Letters **92**, 235003 (2004).
- [60] Y. Liang et al. *Active control of type-I edge localized modes on JET*. Plasma Physics and Controlled Fusion **49**, B581 (2007).
- [61] W. Suttrop et al. *First Observation of Edge Localized Modes Mitigation with Resonant and Nonresonant Magnetic Perturbations in ASDEX Upgrade*. Physical Review Letters **106**, 225004 (2011).
- [62] W. Suttrop, O. Gruber, B. Kurzan, H. D. Murmann, J. Neuhauser, J. Schweinzer, J. Stober, W. Treutterer and the ASDEX Upgrade Team. *Effect of plasma shape variation on ELMs and H-mode pedestal properties in ASDEX Upgrade*. Plasma Physics and Controlled Fusion **42**, A97 (2000).
- [63] J. Pearson, Y. Liang, C. Gimblett, D. Reiser, Y. Sun, T. Zhang and Y. Yang. *Modelling of edge localized modes with a current relaxation model on JET and TEXTOR*. Nuclear Fusion **52**, 074011 (2012).
- [64] P. B. Snyder, T. H. Osborne, K. H. Burrell, R. J. Groebner, A. W. Leonard, R. Nazikian, D. M. Orlov, O. Schmitz, M. R. Wade and H. R. Wilson. *The EPED pedestal model and edge localized mode-suppressed regimes: Studies of quiescent H-mode and development of a model for edge localized mode suppression via resonant magnetic perturbations*. Physics of Plasmas **19**, 056115 (2012).

-
- [65] I. T. Chapman et al. *Towards understanding edge localised mode mitigation by resonant magnetic perturbations in MAST*. *Physics of Plasmas* **20**, 056101 (2013).
- [66] A. Kirk et al. *Understanding the effect resonant magnetic perturbations have on ELMs*. *Plasma Physics and Controlled Fusion* **55**, 124003 (2013).
- [67] T. Evans et al. *RMP ELM suppression in DIII-D plasmas with ITER similar shapes and collisionalities*. *Nuclear Fusion* **48**, 024002 (2008).
- [68] T. Eich, A. Herrmann and J. Neuhauser. *Nonaxisymmetric Energy Deposition Pattern on ASDEX Upgrade Divertor Target Plates during Type-I Edge-Localized Modes*. *Physical Review Letters* **91**, 195003 (2003).
- [69] M. Jakubowski et al. *Toroidally resolved structure of divertor heat flux in RMP H-mode discharges on DIII-D*. *Journal of Nuclear Materials* **415**, S901 –S905 (2011).
- [70] S. Devaux, T. Eich, G. Arnoux, W. Fundamenski and H. Thomsen. *Type-I ELM filamentary substructure on the JET divertor target*. *Journal of Nuclear Materials* **415**, S865 –S868 (2011).
- [71] T. Eich et al. *Type-I ELM substructure on the divertor target plates in ASDEX Upgrade*. *Plasma Physics and Controlled Fusion* **47**, 815 (2005).
- [72] M. Jakubowski et al. *Overview of the results on divertor heat loads in RMP controlled H-mode plasmas on DIII-D*. *Nuclear Fusion* **49**, 095013 (2009).
- [73] A. Fasoli et al. *Chapter 5: Physics of energetic ions*. *Nuclear Fusion* **47**, S264 (2007).
- [74] M. Heyn, I. Ivanov, S. Kasilov, W. Kernbichler, A. Loarte, V. Nemov and A. Runov. *On the confinement of passing alpha particles in a tokamak-reactor with resonant magnetic field perturbations shielded by plasma currents*. *Nuclear Fusion* **52**, 054010 (2012).

Bibliography

- [75] O. Asunta, S. Äkäslompolo, T. Kurki-Suonio, T. Koskela, S. Sipilä, A. Snicker, M. García-Muñoz and the ASDEX Upgrade team. *Simulations of fast ion wall loads in ASDEX Upgrade in the presence of magnetic perturbations due to ELM-mitigation coils*. Nuclear Fusion **52**, 094014 (2012).
- [76] T. Koskela, O. Asunta, E. Hirvijoki, T. Kurki-Suonio and S. Äkäslompolo. *ITER edge-localized modes control coils: the effect on fast ion losses and edge confinement properties*. Plasma Physics and Controlled Fusion **54**, 105008 (2012).
- [77] M. Garcia-Munoz et al. *Fast-ion redistribution and loss due to edge perturbations in the ASDEX Upgrade, DIII-D and KSTAR tokamaks*. Nuclear Fusion **53**, 123008 (2013).
- [78] M. A. V. Zeeland et al. *Modulation of prompt fast-ion loss by applied $n = 2$ fields in the DIII-D tokamak*. Plasma Physics and Controlled Fusion **56**, 015009 (2014).
- [79] M. Rack, Y. Liang, H. Jaegers, J. Aßmann, G. Satheeswaran, Y. Xu, J. Pearson, Y. Yang, P. Denner and L. Zeng. *A rotating directional probe for the measurements of fast ion losses and plasma rotation at Tokamak Experiment for Technology Oriented Research*. Review of Scientific Instruments **84**, 083501 (2013).
- [80] A. Kirk, S. Lisgo, E. Nardon, T. Eich, A. Herrmann, A. Kallenbach and A. Loarte. *Physics of ELM power fluxes to plasma facing components and implications for ITER*. Journal of Nuclear Materials **390-391**, 727–732 (2009).
- [81] T. E. Evans, J. H. Yu, M. W. Jakubowski, O. Schmitz, J. G. Watkins and R. A. Moyer. *A conceptual model of the magnetic topology and nonlinear dynamics of ELMs*. Journal of Nuclear Materials **390-391**, 789–792 (2009).
- [82] A. Wingen, T. E. Evans, C. J. Lasnier and K. H. Spatschek. *Numerical Modeling of Edge-Localized-Mode Filaments on Divertor Plates Based on Thermoelectric Currents*. Physical Review Letters **104**, 175001 (2010).

- [83] M. Rack, A. Wingen, Y. Liang, K. Spatschek, D. Harting, S. Devaux and JET-EFDA contributors. *Thermoelectric currents and their role during ELM formation in JET*. Nuclear Fusion **52**, 074012 (2012).

A. Publications included

Chapter 3:

- M. Rack, B. Sieglin, T. Eich, J. Pearson, Y. Liang, I. Balboa, S. Jachmich, A. Wingen, S. Pamela and J. E. Contributors. *Findings of pre-ELM structures through the observation of divertor heat load patterns at JET with applied $n = 2$ perturbation fields*. Nuclear Fusion **54**, 072004 (2014).
- M. Rack, B. Sieglin, J. Pearson, T. Eich, Y. Liang, P. Denner, A. Wingen, L. Zeng, I. Balboa, S. Jachmich and J.-E. Contributors. *Modified heat load deposition of the ELM crash due to $n = 2$ perturbation fields at JET*. Nuclear Fusion **54**, 064012 (2014).

Chapter 4:

- M. Rack, L. Zeng, P. Denner, Y. Liang, A. Wingen, K. Gan, L. Wang, F. Liu, B. Shen, B. Wan, J. Li and the EAST Team. *Modelling of LHW-induced helical current filaments on EAST: study of an alternative method of applying RMPs*. Nuclear Fusion **54**, 064016 (2014).
- Y. Liang, X. Z. Gong, K. F. Gan, E. Gauthier, L. Wang, M. Rack, Y. M. Wang, L. Zeng, P. Denner, A. Wingen, B. Lv, B. J. Ding, R. Chen, L. Q. Hu, J. S. Hu, F. K. Liu, Y. X. Jie, J. Pearson, J. P. Qian, J. F. Shan, B. Shen, T. H. Shi, Y. Sun, F. D. Wang, H. Q. Wang, M. Wang, Z. W. Wu, S. B. Zhang, T. Zhang, X. J. Zhang, N. Yan, G. S. Xu, H. Y. Guo, B. N. Wan and J. G. Li. *Magnetic Topology Changes Induced by Lower Hybrid Waves and their Profound Effect on Edge-Localized Modes in the EAST Tokamak*. Physical Review Letters **110**, 235002 (2013).
- J. Li, H. Y. Guo, B. N. Wan, X. Z. Gong, Y. F. Liang, G. S. Xu, K. F. Gan, J. S. Hu, H. Q. Wang, L. Wang, L. Zeng, Y. P. Zhao, P.

A. Publications included

Denner, G. L. Jackson, A. Loarte, R. Maingi, J. E. Menard, M. Rack and X. L. Zou. *A long-pulse high-confinement plasma regime in the Experimental Advanced Superconducting Tokamak*. *Nature Physics* **9**, 817–821 (2013).

Chapter 5:

- M. Rack, Y. Liang, H. Jaegers, J. Aßmann, G. Satheeswaran, Y. Xu, J. Pearson, Y. Yang, P. Denner and L. Zeng. *A rotating directional probe for the measurements of fast ion losses and plasma rotation at Tokamak Experiment for Technology Oriented Research*. *Review of Scientific Instruments* **84**, 083501 (2013).
- M. Rack, Y. Liang, P. Denner, J. Pearson, Y. Yang, L. Zeng and the TEXTOR Team. *On the effects of magnetic perturbations on fast ion losses studied at TEXTOR*. submitted to *Plasma Physics and Controlled Fusion*. (2014).

Letter

Findings of pre-ELM structures through the observation of divertor heat load patterns at JET with applied $n = 2$ perturbation fields

M. Rack¹, B. Sieglin², T. Eich², J. Pearson¹, Y. Liang¹, I. Balboa³,
S. Jachmich⁴, A. Wingen⁵, S.J.P. Pamela⁶ and JET EFDA
Contributors^a

JET-EFDA, Culham Science Centre, Abingdon, OX14 3DB, UK

¹ Forschungszentrum Jülich GmbH, Institut für Energie-und Klimaforschung-Plasmaphysik, EURATOM Association, 52425 Jülich, Germany

² Max-Planck-Institut für Plasmaphysik, EURATOM-Association, 85748 Garching, Germany

³ EURATOM/CCFE Fusion Association, Culham Science Centre, Abingdon, OX14 3DB, UK

⁴ Laboratoire de Physique des Plasmas-Laboratorium voor Plasmafysica, Association

'Euratom-Belgian state', Ecole Royale Militaire-Koninklijke Militaire School, Partner in the Trilateral Euregio Cluster, B-1000 Brussels, Belgium

⁵ Oak Ridge National Laboratory, PO Box 2008, Oak Ridge, TN 37831-6169, USA

⁶ IIFS-PIIM. Aix Marseille Université-CNRS, 13397 Marseille Cedex 20, France

E-mail: m.rack@fz-juelich.de

Received 29 November 2013, revised 21 February 2014

Accepted for publication 10 March 2014

Published 1 April 2014

Abstract

Resonant magnetic perturbation experiments at JET with the ITER-like wall have shown the formation of radially propagating pre-ELM structures in the heat flux profile on the outer divertor. These appear a few milliseconds before the major divertor heat load, caused by type-I edge-localized modes (ELMs). The formation of the pre-ELM structures is accompanied by an increase in the D_α emission. For some pronounced examples, the propagation appears to end at the positions where an increased heat load is seen during the ELM crash a few milliseconds later. These observations are presented and discussed along with a comparison of a thermoelectric edge currents model.

Keywords: edge-localized modes, resonant magnetic perturbations, divertor heat loads

(Some figures may appear in colour only in the online journal)

1. Introduction

The edge-localized modes (ELMs) which appear in high-confinement mode (H-mode) plasmas are one of the major topics of fusion research since they were first discovered at ASDEX [1, 2]. ELMs lead to fast periodic losses of heat and particles, causing strong increases in the heat flux to the target plates. Uncontrolled type-I ELMs could cause severe damage to the plasma-facing components in large-scale fusion devices, such as ITER [3]. Therefore, a full understanding of ELMs is crucial. ELMs have been studied from various directions, e.g. magnetic signals of magnetohydrodynamic (MHD) behaviour,

heat loads on the divertor targets, release of particles to the scrape-off layer (SOL), and changes to the topology of the plasma edge. Over the last decade, the understanding of ELMs has greatly increased and ELMs are now associated with a non-axisymmetric energy deposition [4], filament-like structures [5] and thermoelectric edge currents [6]. However, the dynamics of ELMs are still not fully understood.

One of the most promising techniques to control ELMs is the use of non-axisymmetric magnetic perturbation fields [7–10], commonly applied as resonant magnetic perturbations (RMPs). Fast infra-red thermography [4, 11, 12] is used on ASDEX Upgrade, DIII-D and JET as the key diagnostic for the study of ELM heat loads on the divertor plates when RMPs are applied. Elsewhere, the MAST tokamak uses a fast visible

^a See the appendix of Romanelli F. *et al* 2012 *Proc. 24th IAEA Fusion Energy Conf. (San Diego, CA, 2012)*. doi:10.1088/0029-5515/53/10/104002

A. Publications included

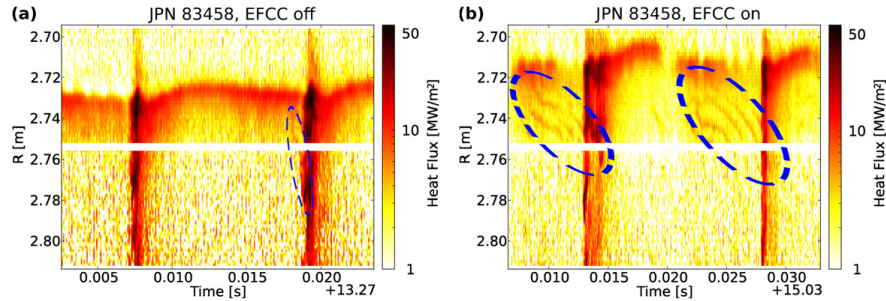


Figure 1. Changes of the divertor heat loads without (a) and with RMPs (b) during the H-mode phase with a plasma current $I_p = 1.4$ MA, a toroidal field $B_t = 2.2$ T, and an edge safety factor $q_{95} = 4.0$. Pre-ELM structures are observed (marked by the ellipses). The white stripe in the heat flux plots indicates the gap between two stacks of the new JET divertor and the colour code gives the heat flux on a logarithmic scale.

light camera for the observation of topology changes in the near X-point region and for filament studies [13, 14].

An RMP ELM control experiment has been performed on JET with the new ITER-like wall, which contains a beryllium main chamber and a tungsten divertor [15]. The error field correction coils (EFCCs) [16] are used for the application of RMP fields to the plasma. During the last shut-down, the power supplies of the EFCCs have been upgraded to provide a current of up to 6 kA, twice as much as before [9]. In this experiment, an $n = 2$ RMP field with an EFCC current of 5 kA has been applied. This EFCC current corresponds to a total current of 80 kA as the EFCCs have 16 turns each. For the study of the divertor heat load patterns, an upgraded infra-red thermography system [17, 18] has been used. The quality of the thermography data is enhanced with the ITER-like wall as the deposition of carbon layer on the divertor is no longer an issue [19].

The experiments show pre-ELM structures that are seen as a change in the divertor heat load pattern. A few milliseconds before a large heat flux, caused by the ELM, reaches the outer divertor plates, a footprint structure is formed near the pre-ELM strike-line position. This grows radially outwards until the major ELM heat pulse appears on the divertor plates. The structure then vanishes after the ELM. The time-scale of this footprint pattern development is large compared to the usual rise time of the ELM heat pulse (in the order of 100 μ s).

This letter focuses on the observation of the pre-ELM structures. These are of importance and interest for the understanding of the dynamic processes during ELM events and their control mechanisms by RMPs. A possible mechanism that could lead to the formation and propagation of such pre-ELM structures is discussed.

2. Experimental observation

In figure 1 a comparison of the divertor heat loads with (b) and without (a) applied RMP fields is shown. Both plots show the heat flux deposition on tile 5 of the outer divertor for the duration of two ELMs (see figure 5 for reference to the JET geometry). The change of the radial position of the strike line between the non-RMP and RMP case is caused by the applied EFCC fields and the shaping control during the discharge. For the case without RMPs we observe standard type-I ELMs, as

reported many times before [12, 20]. The ELM crash leads to a strong increase of the heat flux to the position of the pre-ELM strike line and comes with a burst of particles deposited along the divertor plate in the radially outward direction.

The case with applied RMPs is different. It clearly shows the appearance of a pattern in the period between two ELM crashes (marked by ellipses). These structures continue up to the major heat pulse at the ELM crash. In the case of the applied RMP field, the pre-ELM structures are observed to last for several milliseconds. The standard type-I ELM shows an indication of a pre-ELM structure, but with a much shorter lifetime.

Figure 2 shows two ELM periods during the RMP phase. After each ELM crash the heat flux to the divertor plates is strongly reduced. During that time the pedestal temperature and density recover. In the presented measurement, about 5 ms before the next ELM crash occurs, the heat load at the strike line increases to about 10 MW m^{-2} . Slightly after the increase of the strike line heat load, the above-mentioned footprint structures are created, followed by a reduction of the heat load onto the original strike line by a factor of two. The pre-ELM footprint structures are seen as lines in the time trace of the divertor heat load ($2.76 \text{ m} < R < 2.79 \text{ m}$). The position of these footprint structures is not constant in time, but moves radially outward. Most of the lines are created at a radial position of $2.76 \text{ m} \pm 1 \text{ cm}$, with a distance of about 4 cm to the pre-ELM strike-line position. The radial speed of the structures along the divertor target can be determined to be approximately 20 m s^{-1} . They continue until the major ELM heat pulse reaches the divertor plates. Compared with typical ELMs at JET, the heat load patterns of these ELMs show a split nature. The main heat load is not only deposited at the pre-ELM strike-line position but also comparable high heat fluxes can be observed at different radial positions [21, 22]; especially at those positions where the pre-ELM structures end or will be expected if continuing with the same propagation speed (e.g. $t = 14.8424 \text{ s}$ at $R = 2.788 \text{ m}$; $t = 14.8535 \text{ s}$ at $R = 2.78 \text{ m}$ and $R = 2.795 \text{ m}$). See also figure 1(b), e.g. $t = 15.043 \text{ s}$ at $R = 2.74 \text{ m}$; $t = 15.058 \text{ s}$ at $R = 2.759 \text{ m}$. In contrast, the pre-ELM structures in figure 1(b) start from/close to the original strike line (further details below). Whether this finding is of general nature or is taking place only under special conditions needs further investigation focusing on this

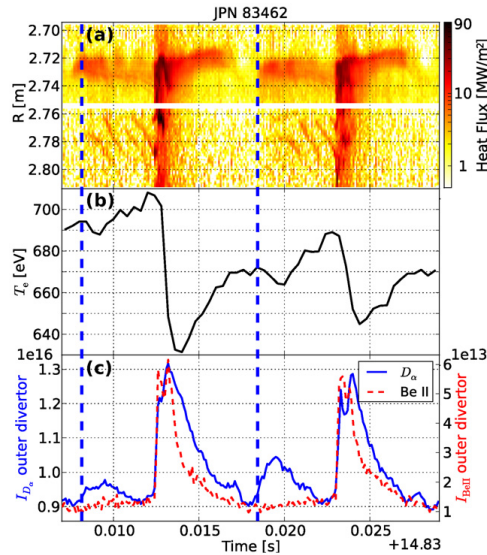


Figure 2. Time trace of the measured heat load pattern on the outer divertor target tile 5 (a) during the application of RMPs ($I_p = 1.4$ MA, $B_t = 1.7$ T, $q_{95} = 3.2$). In addition, a time trace of the electron temperature at normalized poloidal flux $\psi = 0.84$ (b) and the intensity of the D_α and Be II emission light (c) are shown.

interested phenomena also including diagnostic details of such a infra-red system in snap-shot mode.

At the first increase of the heat load at the pre-ELM strike-line (vertical dashed lines), the D_α emission shows an additional peak in the phase between two ELM crashes. After the formation of the pre-ELM structure, the emission decreases again until the pedestal crash due to the ELM. The crash of the pedestal finally brings a strong edge temperature loss and the process starts again.

A comparison of the D_α and Be II light emission from the outer divertor plate during this phase shows that the pre-ELM structures only cause an increase of the D_α emission. The Be II emission stays unaffected by the structures and increases only due to the major heat pulse caused by the ELM crash. This indicates that no highly energetic particles are ejected during the pre-ELM heat load increase. This feature can be used for the detection of pre-ELM structures and a statistical analysis of their appearance time with respect to the following ELM crash is seen in figure 3.

The analysis uses the Be II emission light for the ELM crash detection by locating the time windows in which the emission light peaks (occurrence of ELM crash), and the D_α emission light for the pre-ELM and ELM crash peak detection. In the analysis, 333 pre-ELMs are considered which appeared during the application of RMP with $I_{EFCC} = 5$ kA in a q_{95} range of 3.1–3.5. In that limited q_{95} range, no dependence of the appearance time of the pre-ELM structures on q_{95} could be found. The ELM frequency is approximately 100 Hz during the analysed time windows. The analysis shows that the pre-ELM structures appear on average 2.7 ms before the ELM crash, with a standard deviation of 0.8 ms.

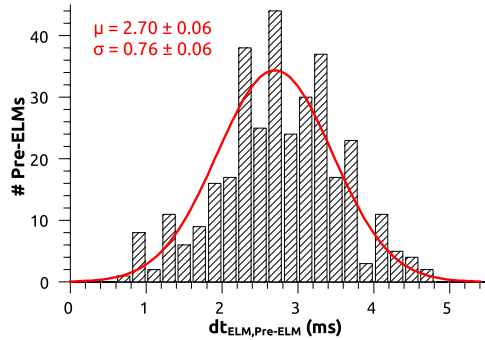


Figure 3. Statistical analysis of the appearance time of the pre-ELM feature with respect to the associated ELM crash.

The propagation speed of the pre-ELM structures is found to vary between 7 and 20 m s⁻¹. The separation of the created structure to the pre-ELM strike-line position is less than 2 cm when the propagation speed is low and increases to about 4 cm when the propagation speed is high. The experiments performed, covered q_{95} from 3.1 to 4.5, where no clear q_{95} dependence was found regarding distance to pre-ELM strike-line position and propagation speed. Throughout the study, no pre-ELM structures on the outer divertor target were observed below an EFCC current of about 2.5 kA. A similar threshold is found for ELM mitigation in the experiments presented in [21]. If the EFCC amplitude increases above this value, a strong increase in the ELM frequency is seen. At the same time, measurements of the plasma response show a change from a linear to a non-linear response to the applied magnetic perturbation. A threshold behaviour was also recently found on MAST [14] dealing with the effect of RMPs on the topology change in the near X-point region. All three observations are made under different conditions and further quantitative analysis is needed before conclusions can be drawn.

3. Pre-ELM structures versus radially propagating ELM filaments

The ELM event can be described as a MHD mode in the plasma edge which becomes non-linearly unstable causing an explosion of particles from the plasma edge to the SOL [23]. ELMs are accompanied by filaments which are created in the plasma edge region during the ELM onset. These filaments separate from the plasma when the ELM crash occurs and propagate radially outwards until they hit the first wall [24]. Analysis of data from different sized tokamaks has shown that the ELM filament propagation speed is typically in the range of 0.5–2 km s⁻¹ [25]. A standard JET plasma has a radial distance to the first wall of about 5–10 cm at the mid-plane. The time the ELM filament spends in the SOL, before interacting with the wall and collapsing, is therefore in the range of 25–200 μ s. Since the observed pre-ELM structures appear in a range of 1–4 ms, they cannot be explained by the much faster radially propagating ELM filaments. The same argument applies for inter-ELM filaments, that were found at MAST [26] to have a radial propagation speed of 1–2 km s⁻¹.

A. Publications included

The observed propagating structures have similar features to previous observations of strike-line splitting during the application of RMPs; see [27]. One requirement for strike-line splitting is a change in the topology of the plasma. This is evidence of a magnetic perturbation of the plasma edge already present before the ELM crash. This perturbation could be formed by internal modes, additional current filaments in the plasma edge, the applied RMP field or a combination of these. Recent findings by Kirk *et al* [14] have shown lobe structures during RMP phases in the near X-point region on MAST. Such lobes create footprint patterns on the divertor plates similar to RMP experiments in L-mode plasmas. However, the radial propagation of the footprint pattern is unusual for strike-line splitting by static RMPs. This demonstrates the dynamic nature of the observed structures. It has been reported that additional thermoelectric currents in the plasma edge during the onset of an ELM can lead to the formation of such dynamic footprint patterns [6, 28].

4. Interpretation based on the thermoelectric current model

The thermoelectric current model [29] describes the non-linear evolution of an ELM. Its application for DIII-D and JET [6, 28] shows good agreement with measurements. The model is based on the concept that an initial heat pulse triggers thermoelectric currents, through short connection length flux tubes [30]. A subsequent self-amplification process leads to a significant change in the magnetic topology, resulting in the complex structure of the footprint pattern as observed experimentally for ELMs.

This conceptual model provides a possible explanation of the experimental observations of the pre-ELM structures; the small drop in the edge electron temperature between two ELM crashes can be seen as the initial heat loss, which arrives on the target and leads to the increased D_α emission. A consequence of the onset of thermoelectric currents is the changing magnetic topology, seen as the appearance of the pre-ELM structures. After the initial heat pulse, the edge electron temperature continues to increase, while the self-amplification process of the thermoelectric currents continues.

The thermoelectric current model is applied to the discharge JET pulse number (JPN) 83462 to study whether the predicted topology changes fits to the observations. Application of the thermoelectric current model to a strongly perturbed RMP plasma results in one main difference regarding previous applications, which consider the much smaller intrinsic error field as the initial perturbation. This is that the RMPs cause much larger regions of short connection length flux tubes. In the early phase of the ELM this leads to a current density on the target considerably smaller than in the case of intrinsic error fields; here assumed to be 1.5 A cm^{-2} (a factor 4 smaller), exact measurements are not available. Figure 4 shows the prediction of the vacuum (thin line) and thermoelectric current model (dashed line) for the pre-ELM structures compared to the measured heat flux (bold line).

Both, the vacuum and the thermoelectric current model, predictions are represented as minimum poloidal flux ψ_{Min} reached by field lines starting from the given target positions which is a measure for the penetration depth. Based on the

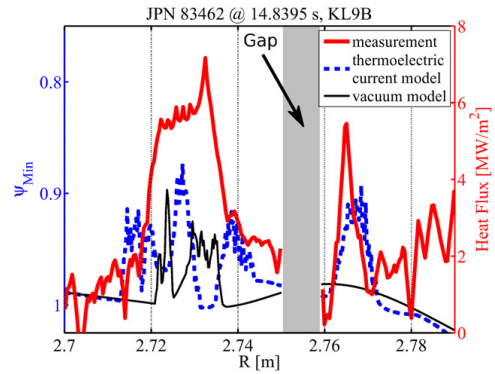


Figure 4. Prediction of the thermoelectric current model (dashed line, in normalized poloidal flux) compared to experimental measurements (bold line) of the heat flux to the outer target for the pre-ELM structure. A thermoelectric edge current of 2 kA is considered. The thin line gives the predicted penetration depth from the vacuum model as a comparison. The equilibrium reconstruction and heat flux profile are taken at 14.8395 s from JPN 83462.

MASTOC criterion it is valid to compare this quantity with measured heat flux profiles on the target [31]: field lines penetrating deeper into the plasma see a hotter region and can transport higher energetic particles to the target causing a larger heat flux compared to field lines staying only in the very edge. By comparing results from the vacuum modelling to the thermoelectric current model, the effect of the additional thermoelectric edge current (about 2 kA) is seen. The observed secondary peak at 2.76 m, caused by the pre-ELM structures, can be resembled by considering these additional edge currents that cause a strong change of the magnetic topology. Owing to the lack of time dependence of the thermoelectric current model, it cannot describe the radial propagation of the structures. Apart from this, the thermoelectric current model provides a possible, but not conclusive, explanation for the appearance of the pre-ELM structures. For a further development of this model the consideration of plasma transport is required. This would on the one hand show the effects of cross-field transport and on the other hand allow a direct modelling of heat fluxes, enabling a quantitative comparison.

5. Discussion

This paper focuses on the appearance of pre-ELM structures with applied EFCC fields. However, it has to be considered that pre-ELM structures are also observed without the additional perturbations by external coils, although less pronounced as seen by a much shorter lifetime; see figure 1(a). Up to now, no studies were carried out to examine whether the appearance without EFCC fields is linked to other, internal perturbations e.g. induced by modes in the plasma. Comparing the observations with and without EFCC fields it can be stated that an event, due to the EFCC fields, is either produced or decoupled from the ELM crash which results in the seen pre-ELM structures. This event is possibly caused by the

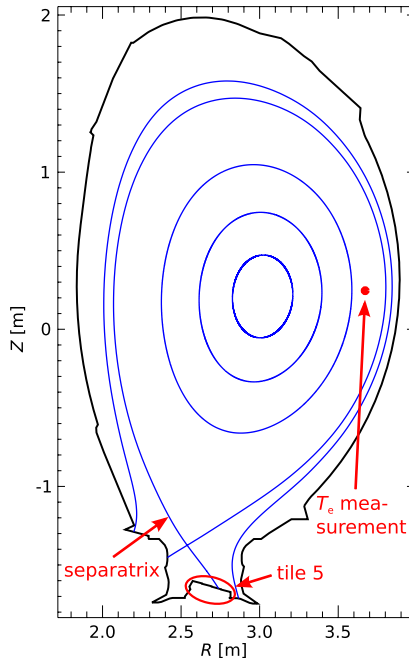


Figure 5. Geometrical set-up of the presented JET experiments. The locations of the heat flux and T_e measurements are shown.

ELM trigger mechanism that also causes the ELM frequency increase seen with RMPs, when the RMPs are understood to lead to an early triggering of ELMs.

A valid question to be discussed is: whether the pre-ELM structures originate from another (smaller) ELM, perhaps of type-III? For answering the question we recall the observations presented and other studies on ELM physics at JET. (1) The observed T_e drop and D_α increase in the phase between two large ELMs is comparably slow and does not show the burst like behaviour as expected for an ELM. (2) Compound ELMs have an irregular behaviour: after a large type-I ELM several small ELMs follow, a behaviour as presented in this letter where small and large D_α peaks appear alternately has never been seen on JET when studying compound ELMs. Furthermore, the pulses analysed are not performed in a regime which shows type-III ELMs at JET [32]. (3) In addition, it has been shown that mitigated ELMs still show the features of type-I ELMs and do not come with compound ELMs [9]. From all this we conclude that the described observations of the pre-ELM structures are unlikely to result from small ELMs.

It has been shown that the thermoelectric current model might predict the appearance of the pre-ELM structures but not their radial propagation. A possible explanation for the radial propagation of the pre-ELM structures may be found by considering the existence of ballooning modes at that early phase of the ELM, which could be enhanced by the RMPs and therefore appear early in the ELM cycle. Simulation results from the reduced MHD code JOEAK, have shown that radially propagating stripes in the heat flux on the divertor

during the ELM crash, are linked to rotating ballooning modes [33]. A radial propagation of the pre-ELM structures could therefore be due to the RMP effects on the ballooning mode stability, including threshold and growth rate, whereas the mode numbers can be dissimilar to the dominant RMP mode. Dedicated simulations considering RMPs have not been carried out. However, experiments have shown that an addition of RMPs causes a slowing down of the toroidal plasma rotation for the plasma configuration used [21]. A slower rotation of the ballooning modes leads to a reduction of the radial propagation speed of the structures. This is in-line with the experimentally observed difference in the propagation speed of the pre-ELM structures compared to the ELM stripes, seen without RMPs [33].

6. Summary

In this letter we have presented new observations of pre-ELM structure in the divertor heat loads. This structure is seen by the appearance of a dynamic, quasi-stable heat flux pattern on the divertor plates a few milliseconds before the ELM crash accompanied by an increase of the D_α emission. The pre-ELM structures appear on a much longer time-scale than that of typical ELM crash rise times [20]. This suggests that the phase prior to an ELM crash has an effect on the particle transport to the divertor before the ELM crash. The appearance location of the pre-ELM structures might be explained by considering thermoelectric currents in the plasma edge. Their radial propagation may be caused by rotating ballooning modes. Further studies, including full transport modelling, are needed to come to a conclusive understanding of the observed phenomena. The pre-ELM structures are not restricted to the application of EFCC fields, although they are seen to be strongly enhanced and appear regularly, when the EFCCs are present and above a threshold similar to that causing saturation of the ELM mitigation. Observed splitting of the ELM crash heat deposition appears to be influenced by the pre-ELM structures, whether this is a general feature of the pre-ELM structures remains open. Further experiments and analysis are needed to quantify this effect.

Acknowledgments

Valuable discussions with Peter de Vries and Sebastijan Brezinsek are gratefully acknowledged. M R is thankful for the support of Evgenij Bleile and Götz Lehmann. This work, supported by the European Communities under the contract of Association between EURATOM and FZJ, was carried out within the framework of the European Fusion Development Agreement. The views and opinions expressed herein do not necessarily reflect those of the European Commission. Additional support from the Helmholtz Association in frame of the Helmholtz-University Young Investigators Group VH-NG-410 is gratefully acknowledged.

References

- [1] Wagner F. *et al* 1982 *Phys. Rev. Lett.* **49** 1408
- [2] Keilhacker M. *et al* 1984 *Plasma Phys. Control. Fusion* **26** 49
- [3] Zhitlukhin A. *et al* 2007 *J. Nucl. Mater.* **363–365** 301

A. Publications included

Nucl. Fusion **54** (2014) 072004

Letter

- [4] Eich T., Herrmann A. and Neuhauser J. 2003 *Phys. Rev. Lett.* **91** 195003
- [5] Kirk A. *et al* 2004 *Phys. Rev. Lett.* **92** 245002
- [6] Wingen A., Evans T.E., Lasnier C.J. and Spatschek K.H. 2010 *Phys. Rev. Lett.* **104** 175001
- [7] Punjabi A., Verma A. and Boozer A. 1992 *Phys. Rev. Lett.* **69** 3322
- [8] Evans T.E. *et al* 2004 *Phys. Rev. Lett.* **92** 235003
- [9] Liang Y. *et al* 2010 *Nucl. Fusion* **50** 025013
- [10] Suttrop W. *et al* 2011 *Phys. Rev. Lett.* **106** 225004
- [11] Jakubowski M. *et al* 2011 *J. Nucl. Mater.* **415** S901
- [12] Devaux S. *et al* 2011 *J. Nucl. Mater.* **415** S865
- [13] Kirk A. *et al* 2006 *Phys. Rev. Lett.* **96** 185001
- [14] Kirk A. *et al* 2012 *Phys. Rev. Lett.* **108** 255003
- [15] Philipps V., Mertens P., Matthews G. and Maier H. 2010 *Fusion Eng. Des.* **85** 1581
- [16] Barlow I. *et al* 2001 *Fusion Eng. Des.* **58–59** 189
- [17] Eich T. *et al* 2011 *J. Nucl. Mater.* **415** S856
- [18] Balboa I. *et al* 2012 *Rev. Sci. Instrum.* **83** 10D530
- [19] Devaux S. *et al* 2011 *38th EPS Conf. Plasma Physics (Strasbourg, France)* O3.108
<http://ocs.ciemat.es/EPS2011PAP/pdf/O3.108.pdf>
- [20] Eich T. *et al* 2005 *Plasma Phys. Control. Fusion* **47** 815
- [21] Liang Y. *et al* 2013 *Nucl. Fusion* **53** 073036
- [22] Rack M. *et al* 2014 Modified heat load deposition of the ELM crash due to $n = 2$ perturbation fields at JET *Nucl. Fusion* at press
- [23] Wilson H.R. and Cowley S.C. 2004 *Phys. Rev. Lett.* **92** 175006
- [24] Fundamenski W., Pitts R.A. and JET EFDA Contributors 2006 *Plasma Phys. Control. Fusion* **48** 109
- [25] Kirk A. *et al* 2009 *J. Nucl. Mater.* **390–391** 727
- [26] Ayed N.B. *et al* 2009 *Plasma Phys. Control. Fusion* **51** 035016
- [27] Harting D. *et al* 2012 *Nucl. Fusion* **52** 054009
- [28] Rack M. *et al* 2012 *Nucl. Fusion* **52** 074012
- [29] Evans T.E. *et al* 2009 *J. Nucl. Mater.* **390–391** 789
- [30] Wingen A., Evans T.E. and Spatschek K.H. 2009 *Nucl. Fusion* **49** 055027
- [31] Nguyen F., Ghendrih P. and Grosman A. 1997 *Nucl. Fusion* **37** 743
- [32] Sartori R. *et al* 2004 *Plasma Phys. Control. Fusion* **46** 723
- [33] Pamela S.J.P. *et al* 2011 *Plasma Phys. Control. Fusion* **53** 054014

Name of journal: Nuclear Fusion

Impact factor: 2.734 (2012)

Type of authorship: 1st

Own contribution: 90%

Details of contribution: Development and implementation of a movement correction algorithm for advancement of the data processing tool, operation of the infra-red camera, development of a tool for the statistical analysis of the pre-ELM timing, analysis and interpretation of the experimental data, application of the thermoelectric current model, preparation and writing of the manuscript.

Modified heat load deposition of the ELM crash due to $n = 2$ perturbation fields at JET

M. Rack¹, B. Sieglin², J. Pearson¹, T. Eich², Y. Liang¹, P. Denner¹,
A. Wingen³, L. Zeng^{1,4}, I. Balboa⁵, S. Jachmich⁶ and JET-EFDA
Contributors^a

JET-EFDA, Culham Science Centre, Abingdon, OX14 3DB, UK

¹ Forschungszentrum Jülich GmbH, Institut für Energie- und Klimaforschung – Plasmaphysik, EURATOM Association, 52425 Jülich, Germany

² Max-Planck-Institut für Plasmaphysik, EURATOM-Association, D-85748 Garching, Germany

³ Oak Ridge National Laboratory, PO Box 2008, Oak Ridge, Tennessee 37831-6169, USA

⁴ Institute of Plasma Physics, Chinese Academy of Sciences, Hefei 230031, People's Republic of China

⁵ EURATOM/CCFE Fusion Association, Culham Science Centre, Abingdon, OX14 3DB, UK

⁶ Laboratoire de Physique des Plasmas - Laboratorium voor Plasmafysica, Association 'Euratom-Belgian state', Ecole Royale Militaire - Koninklijke Militaire School, Trilateral Euregio Cluster, B-1000 Brussels, Belgium

E-mail: m.rack@fz-juelich.de

Received 28 June 2013, revised 21 October 2013

Accepted for publication 9 December 2013

Published 23 May 2014

Abstract

Significant changes in the edge localized mode (ELM) crash heat load deposition patterns compared to typical ELMs are seen via infra-red observations during resonant magnetic perturbation experiments at the Joint European Torus (JET). These modifications result from the changed magnetic topology of the plasma, caused by the perturbations. Dependences on the perturbation strength and the edge safety factor are analysed and discussed. A thermoelectric current model shows that current filaments in the plasma edge could explain the observations. This study gives an insight into how the changed magnetic topology affects the peak heat fluxes of ELMs which is crucial for understanding ELM control.

Keywords: JET, edge localized modes, divertor heat load deposition, resonant magnetic perturbations, thermoelectric current model

(Some figures may appear in colour only in the online journal)

1. Introduction

An edge localized mode (ELM) crash [1] leads to fast, repetitive losses of energy and particles from the plasma edge, resulting in peaked heat fluxes onto the plasma facing components, mainly in the divertor region. The high energy and particle fluxes may be unacceptable for large tokamaks like ITER [2]. Non-axisymmetric perturbations are one option for controlling ELMs. These perturbations are applied as resonant magnetic perturbations (RMPs) and their feasibility has been demonstrated on various, different sized, devices such as MAST [3], AUG [4], DIII-D [5] and JET [6]. However, the current understanding of the involved processes for ELM control is low. An open question is: what is the influence of RMPs on the dynamic of ELMs?

^a See the appendix of Romanelli F. *et al* 2012 *Proc. 24th IAEA Fusion Energy Conf. 2012 (San Diego, CA)* iopscience.iop.org/0029-5515/53/10/104002.

Applying RMPs to a low-confinement mode (L-mode) plasma, results in a perturbation of the plasma edge that changes the magnetic topology and causes a splitting of the strike-line [5, 7]. At a fixed toroidal angle this appears as several stripes in the heat load on the targets. It has been shown that the dependence on the perturbation strength and the edge safety factor is in accordance with modelling predictions based on the vacuum assumption [7]. The vacuum assumption only takes into account the magnetic fields of the toroidal symmetric equilibrium reconstruction, and the non-axisymmetric fields of the applied RMPs.

A different situation is found for the high-confinement mode (H-mode) discharges, which we are focussing on throughout the paper. No observations of continuous strike-line splitting of the divertor heat loads are reported in ELMy H-mode plasmas on the Joint European Torus (JET). The lack of splitting in these H-mode cases suggests that the effect of

RMPs is weakened. A spin-up of the electron perpendicular rotation caused by the high amount of neutral beam injection (NBI) is understood as one reason for the appearance of plasma response that results in the so-called RMP screening [8]. Different observations were made on the DIII-D tokamak, where a continuous splitting of the divertor heat flux appears during H-mode discharges, but larger than that predicted by simple vacuum assumption modelling [9].

However, different observations are made for the phases during ELM crashes. Findings at DIII-D show splitting of the ELM crash heat load deposition. In low-collisionality plasmas an agreement to vacuum model predictions for the splitting could be found. The splitting of type-I ELMs comes along with a drop of the deposited energy per ELM and was stated as a locking of the ELM to the RMPs [10]. A concern for ITER is the observation that the energy deposition on secondary stripes can exceed the amount of energy deposited at the position of the original strike-line. In cases where larger amounts of splitting occurs, the higher order strike-lines could be located in regions not specified for these high heat loads. Therefore, this is of high relevance for the design of the divertor.

The good agreement of the vacuum model predictions and measurements in low-collisionality H-mode plasmas suggests that the RMPs change the magnetic topology in the same way as it is known from L-mode discharges. It is now necessary to investigate the similarities between the L-mode and ELM crash observations in terms of the changed magnetic topology.

In this paper, the effects of RMPs on the heat load deposition patterns at the outer target, during ELM crashes on JET, and the dependence on a changed magnetic topology, are presented. Firstly, after a description of the experimental set-up, the significant differences of the heat deposition without and with RMPs are shown and discussed (sections 3.1 and 3.2). Secondly, the splitting is studied in terms of its dependence on the changed magnetic topology (sections 3.2.1 and 3.2.2) by varying the perturbation amplitude and the edge safety factor. Finally, the modified heat deposition is compared to a vacuum model and to an extension of this model, incorporating thermoelectric currents (section 4). It will be shown that for moderate-collisionalities the consideration of thermoelectric currents is necessary to result in good agreement.

2. Experimental set-up

During the JET shut-down between 2009 and 2011 the quality of the infra-red measurements has been greatly improved due to the new Tungsten divertor [11], and the upgraded infra-red divertor observation system [12, 13]. Furthermore the now available stronger perturbation fields lead to more pronounced effects. Compared to the old Carbon divertor, thermography on Tungsten is much more reliable due to the avoidance of a surface layer build up [14]. With these significant improvements, JET becomes an ideal device for the further study of the ELM crash heat deposition splitting.

Infra-red thermography is the key diagnostic for the discussed observations. Due to the high temporal and spatial resolution of the JET infra-red divertor cameras they allow for a good characterization of the heat loads deposited during an ELM crash as well as giving information about the ELM dynamic itself. The camera views the outer divertor from

the top of the machine, at a toroidal location of 43° . Its spatial resolution is 1.6 mm and the camera was operated at a frequency of about 10 kHz.

All presented experiments are performed in type-I ELMy H-mode plasmas with a toroidal magnetic field $B_t = 1.85$ T, and plasma currents between $I_p = 1.18$ – 1.38 MA, which results in edge safety factors in the range of $q_{95} = 3.4$ – 4.0 . The target plasma, with a moderate electron pedestal collisionality around $v_e^* \sim 0.7$, was sustained by additional NBI heating of 9.2 MW. A slim divertor configuration with a low triangularity ($\delta_U \sim 0.1$, $\delta_L \sim 0.4$) was chosen for the plasma shape.

At JET, the error field correction coils (EFCCs) [15] are used to apply RMPs. Each coil consist of 16 turns with a maximum current of $I_{\text{EFCC}} = 6$ kA per turn which makes a total current of $I_{\text{EFCC}} = 96$ kA per coil. For the discussed experiments the perturbation fields were operated to apply a dominant toroidal mode number $n = 2$. Based on calculations using the vacuum assumption the maximum applied perturbation current $I_{\text{EFCC}} = 5$ kA results in an effective perturbation of $b_{\text{res}}^{\text{eff}} = 3 \times 10^{-4}$ on the resonant surface $q = 3.5$.

3. Experimental observations

3.1. Typical ELM crash structures without RMPs

An ELM crash leads to a strong increase of the heat load at the original strike-line position due to the increased particle transport and the higher energetic particles leaving the confined region of the plasma. Additionally, a non-axisymmetric deposition of heat on the target, with a large radial spread in the outward direction, appears. Figure 1 gives a typical example of the heat deposition during one ELM crash of the discharge with JET pulse number (JPN) 82469. Here, the original strike-line is located at a major radius $R = 2.73$ m, where the highest heat flux during the ELM crash arrives.

The chaotic heat and energy deposition pattern on the target plates is understood to result from the natural ergodization during an ELM [16]. Natural ergodization means here that during the ELM, currents in the plasma edge create a chaotic layer even without externally applied RMPs. This pattern shows filamentary structures that appear at different radial positions with an increasing number of filaments during the ELM crash. Some filamentary structures propagate radially outward during the ELM crash [17]. As a consequence of the natural ergodization the locations and amplitudes of the individual heat flux peaks vary strongly for each ELM crash [18], also seen in figure 1 (bottom) where the averaged profile does show a smooth radial decay compared to the profile of the single ELM.

3.2. RMP effects on the ELM crash structures

The ELM crash structures seen during applied RMPs are different. They show splitting of the peaked heat flux and a reduced peak heat flux compared to the non-RMP case; see figure 2 (same pulse as before, but during the RMP phase). Furthermore, the duration of the increased heat deposition is reduced compared to the phase without applied RMPs which was found as a general feature of RMPs and comes along with the increase in ELM frequency [19, 20]. When the ELM

A. Publications included

Nucl. Fusion 54 (2014) 064012

M. Rack et al

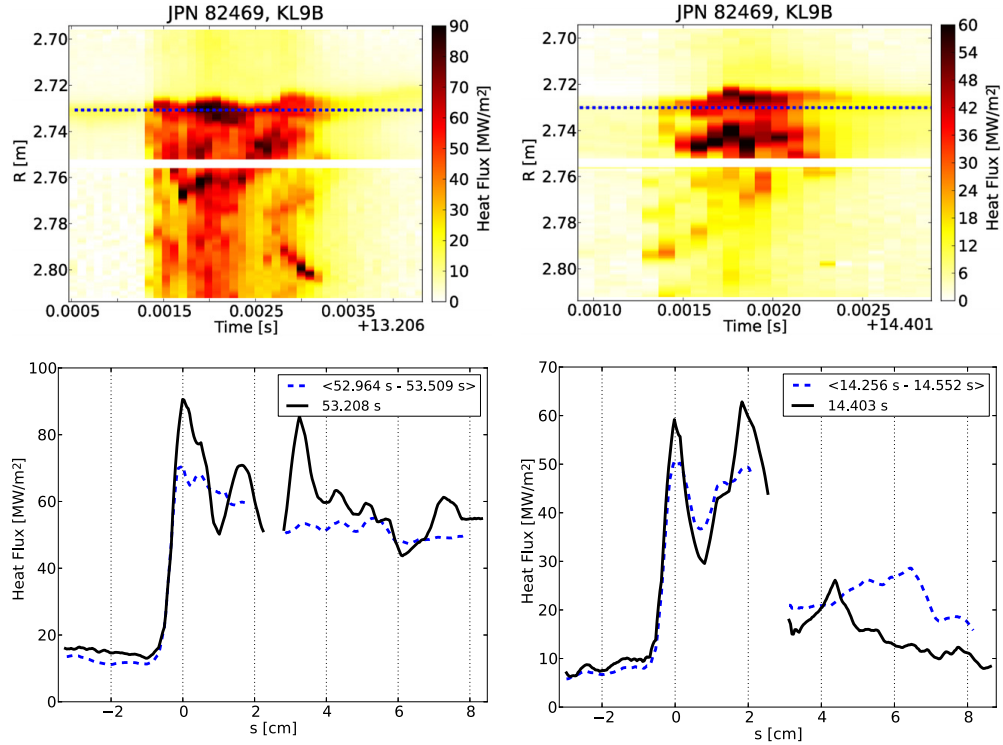


Figure 1. (top) Heat load deposition of one ELM showing typical heat deposition patterns. Plotted is the length along two of four lamellas of the outer target versus time. The colour scale indicates the amount of heat flux, the white line marks the gap between the two lamellas, and the dotted line indicates the location of the original strike-line before the ELM crash. (bottom) Radial profile of the ELM at the time of the maximum peak heat flux (solid) compared with an averaged profile for eight ELMs (dashed), s is the distance to the original strike-line position. The data is acquired at a plasma current $I_p = 1.38$ MA, a toroidal magnetic field $B_t = 1.85$ T, and an edge safety factor $q_{95} = 3.4$.

Figure 2. ELM heat flux during applied RMP fields ($I_{EFCC} = 2.8$ kA) for the same pulse as in figure 1. (top) Temporal evolution for one ELM, and (bottom) the profile at the maximum peak value for the same ELM (solid) as well as the average over eight ELMs (dashed).

crash occurs, an increase of the heat flux at the original strike-line position is observed, which is similar to typical ELM crash structures, but no clear radial propagating structures in the region further away from the original strike-line can be found. Instead a second region of strong heat flux appears and stays at a constant radial position over the duration of the ELM crash. This observation is comparable to the strike-line splitting caused by RMPs in L-mode discharges, but limited for the duration of an ELM crash.

It is hypothesized that the appearance of splitting for the ELM crash heat deposition results from the same mechanism as the observations for L-mode discharges. This suggests that the heat pattern will be affected by changes in the magnetic topology caused by different perturbation amplitudes or edge safety factors.

3.2.1. Dependence on the RMP amplitude. In figure 3 averaged ELM crash heat deposition profiles observed for the

same discharge at different perturbation amplitudes are shown: during the perturbation ramp-up (solid, $I_{EFCC} = 0.35$ kA), and at a high, constant perturbation amplitude (dashed, $I_{EFCC} = 2.4$ kA).

The amount of splitting appears to be dependent on the applied RMP strength. For a lower perturbation, a splitting of around 1.5 and 3.3 cm is observed for the additional stripes. For the case of the highest perturbation, the splitting is increased to a separation of about 2.3 and 6.0 cm. The distance of the third region from the original strike-line varies between 5 and 7 cm in the case of the strong perturbation. This third stripe is much lower in its heat flux, than the other two.

Similar behaviour is experimentally seen and theoretically predicted in L-mode studies where strike-line splitting at a fixed toroidal angle only appears above a certain RMP threshold [7]. The modelling suggests that this is due to a toroidally growing lobe structure which at a high enough perturbation, elongates into the area viewed by the infra-red diagnostic. This explains the appearance of the third region, however, it does not explain the increased separation of the original strike-line and the stripe next to it seen for the medium to high perturbation case.

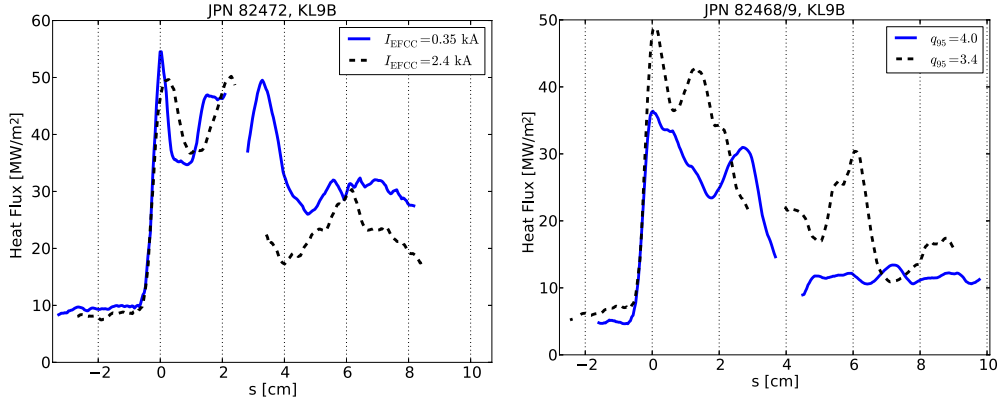


Figure 3. Averaged ELM heat fluxes during different phases of the applied RMPs: (solid) five ELMs during the EFCC ramp-up with $I_{\text{EFCC}} = 0.35$ kA, (dashed) seven ELMs at high constant EFCC current $I_{\text{EFCC}} = 2.4$ kA. Plasma parameters are the same as in figure 1.

3.2.2. Dependence on the edge safety factor. Previous analyses of the RMP effects on L-mode plasmas have also shown a dependence of the edge safety factor on the observed splitting of the strike-line [7]. A small change in q_{95} acts as a shift of the footprint structure along the divertor targets and therefore the splitting, observed at a fixed toroidal position, appears to increase or decrease depending on the q_{95} change. Small changes do not affect the resonance of the applied RMPs as they only lead to a negligible movement of the resonant surfaces in the plasma edge.

Two pulses with $q_{95} = 4.0$ (solid) and $q_{95} = 3.4$ (dashed) are shown in figure 4 (top). The amount of splitting of the ELM heat deposition decreases with decreasing q_{95} . This can be seen by the peaks at $s = 2.8$ cm and $s = 7.3$ cm coming about 1.5 cm closer to the original strike-line for the low q_{95} . This general trend is in-line with the observations from strike-line splitting for L-mode plasmas at JET. The q -scan is performed by changing the I_p for a constant $B_t = 1.8$ T.

In [10] it was stated that the ELMs lock to the external applied field, which would suggest no further movement in the heat load patterns for the duration of the ELM crash. The observations at JET show clear differences. Although the ELM crash heat deposition seems to be located at pre-defined static positions, the ELM heat load shows a remaining dynamic as seen for typical ELMs and described by filamentary structures. An example is shown in figure 4 (bottom) where for instance the stripe starting at $R = 2.73$ m shows a radial outward propagation of a filamentary structure.

4. Modelling of RMP affected ELMs

4.1. Vacuum assumption

It was presented in the previous section that the ELM crash heat depositions are clearly influenced by the RMPs. Changes in the magnetic topology lead to modifications in the deposition patterns. Field line tracing based on the vacuum

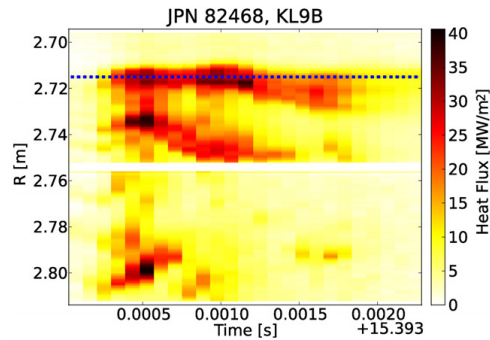


Figure 4. (top) Averaged heat flux profiles during the maximum ELM heat deposition for pulses with different q_{95} , due to different plasma currents ($I_p = 1.18$ MA, eight ELMs (solid) and $I_p = 1.38$ MA, six ELMs (dashed)). (bottom) Temporal evolution of the heat flux profile for an ELM heat load deposition showing a remaining dynamic during the deposition. A perturbation current of $I_{\text{EFCC}} = 5$ kA is used.

assumption is a standard technique to predict the RMP changed magnetic topology without considering any plasma response. A comparison of vacuum modelling predictions with the experimental measurements is shown in figure 5. Two ELMs during the same pulse are compared: one at a weak magnetic perturbation with $I_{\text{EFCC}} = 1.6$ kA (left) and another at a strong perturbation with $I_{\text{EFCC}} = 4.9$ kA (right). The experiment (top) shows large splitting for the strong perturbation case whereas no clear splitting is seen in the case of a weaker perturbation. It has to be stated here that due to the changes in the perturbation strength the target plasma at JET also changes. Especially, the shape compensation coils will cause shifts in the strike-line position and modifications in the plasma shape. For the consideration of these further effects in the modelling, corresponding equilibria reconstructions are used for the different cases. The modelling (bottom) shows the footprints on the outer target with ϕ , the toroidal angle. The colour scale gives the minimum poloidal flux, ψ_{Min} , reached by field lines started from the outer target according to the position given in the plot [21]. At regions with a smaller

A. Publications included

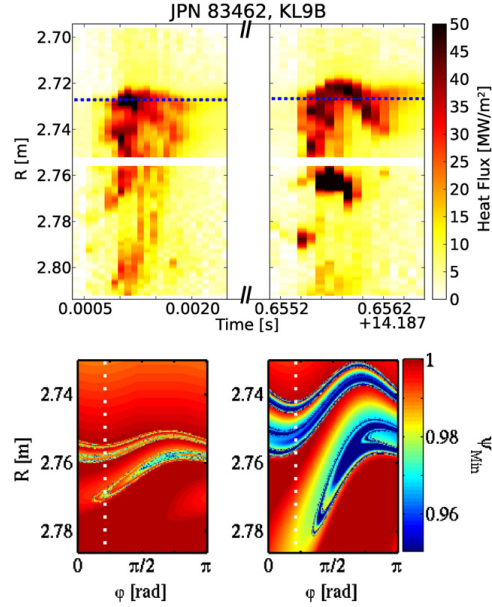


Figure 5. Comparison of the heat fluxes during two ELM crashes with different perturbation amplitudes (top) and the corresponding vacuum model predictions (bottom). Perturbation currents of $I_{EFCC} = 1.6$ kA (left) and $I_{EFCC} = 4.9$ kA (right) are used.

minimum poloidal flux, i.e. stronger penetration depth, it is expected to observe higher heat fluxes [22] which allows for this comparison. The modelling predicts for the two cases a difference in broadening of the region covered by the lobe structure. For weak perturbations, the strike-line extends about 2 cm radially, in the strong perturbation case the extension is more than doubled.

The comparison shows, that an absolute agreement of the original strike-line position between the modelling and experiments is not given, therefore only a qualitative comparison is possible. This disagreement originates from the EFIT equilibrium calculation [23] as such is a 2D reconstruction of a non-axisymmetric plasma configuration. A 3D reconstruction would be a better basis for the calculations, but does not exist. Based on the results, it can be stated that predictions and measurements show the same trend regarding the amount of splitting: the predicted separation between original strike-line and tip of the lobe is much larger for strong perturbations which agrees to the measured heat deposition. However, considering the absolute position of the infra-red camera (marked by the dotted lines), no agreement in the locations can be found between vacuum modelling and experiments for the case with the strong perturbation.

A more precise comparison is given in figure 6, where the heat flux profile (solid) for the time of the maximum peak heat flux is compared to the vacuum model predictions (dashed). The minimum poloidal flux, ψ_{Min} , reached by field lines, started from the target, is used for the comparison as a measure of the penetration depth. A much less broadened

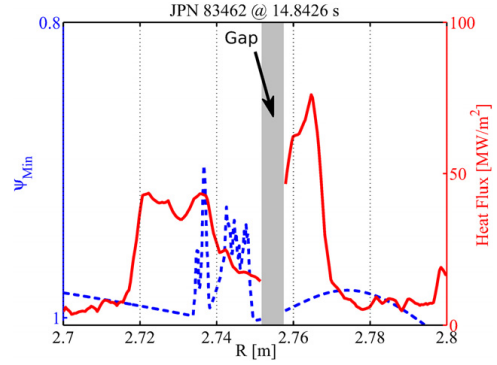


Figure 6. Comparison of the predicted penetration depth by the vacuum model (dashed) with the measured heat flux profile (solid) for the strong perturbation case in figure 5. An artificial shift in radial direction has been introduced to the modelled data as discussed in section 4.2.

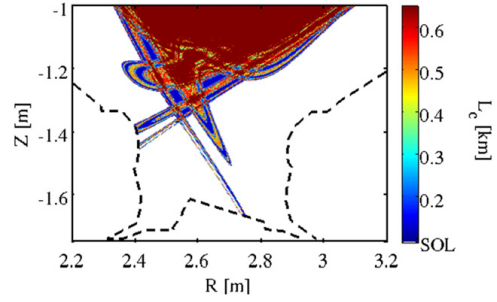


Figure 7. Connection length plot near the X-point region predicted by the vacuum model for the strong perturbation case in figure 5. The colour scale gives the connection length and white marks the scrape-off layer (SOL).

heat flux deposition is predicted by the vacuum model than experimentally measured. This is in contrast to the findings for low-collisionality cases on DIII-D, where a good agreement was found.

4.2. Thermoelectric current model

For typical ELMs, an interpretation of the ELM crash heat deposition patterns, based on the thermoelectric current model considering additional plasma edge currents, was found to result in good agreement with predictions and experiments [24, 25]. Up to now, the thermoelectric current model has only been applied to ELMs without RMPs. In the following, the model is applied to an ELM during the RMP phase and the necessity of thermoelectric currents to explain the observed ELM crash heat deposition pattern is discussed.

The starting point for the model is a perturbed magnetic topology, here with $n = 2$ fields at a perturbation current of $I_{EFCC} = 4.9$ kA. The changed magnetic topology, represented by a connection length plot in figure 7, shows short-connection length flux tubes (blue regions) created due to the initial RMP

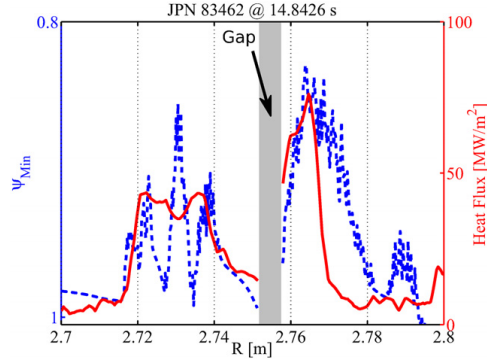


Figure 8. Comparison of the predicted penetration depth by the thermoelectric current model (dashed) with the measured heat flux profile (solid).

fields [26]. The model is based on the idea that triggered by an initial heat pulse during the ELM, thermoelectric currents flow through short-connection length flux tubes. This additional non-axisymmetric current flow is incorporated in the field line calculations and results in a strong change of the magnetic topology. It leads to a further growth of the lobe structures and the formation of several new structures due to the additional perturbations. For more details on the implementation of the thermoelectric current model for JET see [25].

Figure 8 compares the predicted penetration depth (dashed) by the thermoelectric current model with the experimental measured heat flux profile (solid) at one toroidal position. The thermoelectric current is assumed to have a current density of 6 A cm^{-2} on the outer target which results in a total current of 2.7 kA running through the short-connection length flux tubes via two poloidal turns from the outer to the inner target (see [25, 27]). This comparison shows that an addition of thermoelectric currents allows for a much better agreement than the vacuum assumption. The misalignment, discussed previously, was compensated by manual adjustment in figures 6 and 8 of $\Delta R = 7 \text{ mm}$ to achieve a strike-line alignment in the thermoelectric current model predictions.

By considering thermoelectric currents in the calculations of the magnetic topology, the model potentially covers the existence of the experimentally observed ELM filaments [28]. Due to the additional non-axisymmetric currents, an ergodization of the plasma edge is caused. This ergodization, resulting from the modelling, can be understood as the natural ergodization of ELMs, seen in experiments. The addition of RMPs brings a further ergodization, forcing the ELM heat deposition in pre-defined patterns. Only by considering both sources of ergodization can ELM crash heat deposition patterns during applied RMPs can be understood.

5. Discussion

The effects of RMPs on ELMs can be put in two classes: those influencing the ELM trigger mechanism, e.g. seen by an increased ELM frequency, and those affecting the ELM crash heat deposition, e.g. the discussed findings that show

clear splitting during H-mode discharges for the duration of an ELM crash.

In [10], a mechanism was suggested to explain why splitting appears only in the ELM crash heat deposition but not during the time between two ELM crashes. It is based on the idea that the RMPs perturb only the very edge of the plasma and create stochastic lobes which contain high energetic particles for a short period after the ELM crash and are cooled in the time between two ELM crashes. However, this mechanism does not explain the feature that the positions of the outermost heat deposition are not similar for every ELM which leads to a broadening in the averaged profiles as seen in figure 2. Thus, an additional mechanism to that proposed in [10] is suggested whereby the strong drop in electron temperature and density when a crash occurs reduces the screening. The drop in the electron profiles will effects the screening directly through the electron perpendicular rotation. This shows a dependence on $E \times B$ and ∇p_e , with E the electric field, B the magnetic field, and p_e the electron pressure. In the pedestal region, ∇p_e is the dominant parameter leading to the strong RMP screening in H-modes. The drop in temperature and density reduces the pressure gradient in the plasma edge, consequently lowering the electron perpendicular rotation, and therefore allows RMPs to penetrate deeper in the plasma. Therefore, if the additional mechanism is present the observations of the moving outermost strike-line could be explained by different ELM sizes, where for a smaller ELM, a larger RMP screening remains reducing the effect of the external field on the ELM crash heat deposition.

The good agreement of the thermoelectric current model prediction to the measurements strongly suggests the existence of additional edge currents during the ELM crash. An ELM crash leads to a redistribution of any existing currents in the pedestal region. During the ELM cycle such currents will start to slowly diffuse in radial direction. Once the currents reach and diffuse in the short-connection length flux tubes, they are quickly lost to the targets due to the much faster parallel transport. However, the field line tracing model only considers changes in the magnetic topology and lacks in the comparison with the experiments due to the missing plasma component. Therefore, a qualitative comparison can only be provided and no comparison of absolute values. Also cross-field diffusion is not considered as it is in fluid codes like EMC3. This also will have an influence on the predicted broadening.

In addition to the increased ELM frequency leading to a reduction of the ELM size, the split nature of the ELM crash heat deposition provides a further explanation of a reduced peak heat flux with RMPs due to the broader redistribution of the heat on the target. Through the dependence on the edge safety factor, it has been seen that the splitting has a toroidal dependence. Therefore, it is necessary to view the ELM heat load deposition pattern at different toroidal locations to understand if and how the heat distribution can be optimized to reach the lowest possible load on the plasma facing components.

The presented results show that the ELM crash heat deposition during RMPs can exceed the vacuum modelling predicted broadening. This larger splitting can lead to large heat loads being placed outside of the divertor region during RMP application which would be a problem for ITER. These effects needs to be considered to guarantee a safe operation.

A. Publications included

6. Summary

One understood effect of RMPs on a tokamak plasma is the appearance of strike-line splitting in L-mode discharges. However, the behaviour in H-mode discharges is different: no continuous strike-line splitting in the divertor heat load can be seen on JET, the splitting is only observable for the duration of an ELM crash. This paper shows, that the effects of RMPs on the ELM crash heat deposition pattern in contrast with typical ELM crashes result in the preferred static heat deposition during the ELM crash. A dependence on the applied perturbation strength and on the edge safety factor has been shown. The observed splitting in the ELM heat deposition disagrees for moderate-collisionalities to the vacuum model predictions. This paper shows that by considering further plasma edge currents, here motivated by thermoelectric currents, it is possible to find an agreement between the model predictions and experiments. These plasma responses can result in significantly larger splitting than expected from vacuum modelling predictions.

Acknowledgments

M.R. thanks Evgenij Bleile and Götz Lehmann for the long lasting support. This work, supported by the European Communities under the contract of Association between EURATOM and FZJ, was carried out within the framework of the European Fusion Development Agreement. The views and opinions expressed herein do not necessarily reflect those of the European Commission. Additional support from the Helmholtz Association in frame of the Helmholtz-University Young Investigators Group VH-NG-410 is gratefully acknowledged.

References

- [1] Connor J.W. 1998 *Plasma Phys. Control. Fusion* **40** 531
- [2] Loarte A. et al 2003 *Plasma Phys. Control. Fusion* **45** 1549
- [3] Kirk A. et al 2011 *Plasma Phys. Control. Fusion* **53** 065011
- [4] Suttrop W. et al 2011 *Phys. Rev. Lett.* **106** 225004
- [5] Evans T.E. et al 2004 *Phys. Rev. Lett.* **92** 235003
- [6] Liang Y. et al 2007 *Plasma Phys. Control. Fusion* **49** B581
- [7] Harting D. et al 2012 *Nucl. Fusion* **52** 054009
- [8] Nardon E., Tamain P., Bécoulet M., Huysmans G. and Waelbroeck F. 2010 *Nucl. Fusion* **50** 034002
- [9] Evans T.E., Joseph I., Moyer R.A., Fenstermacher M.E., Lasnier C.J. and Yan L.W. 2007 *J. Nucl. Mater.* **363–365** 570–4
- [10] Jakubowski M. et al 2009 *Nucl. Fusion* **49** 095013
- [11] Philipps V., Mertens P., Matthews G. and Maier H. 2010 *Fusion Eng. Des.* **85** 1581–6
- [12] Eich T., Thomsen H., Fundamenski W., Arnoux G., Brezinsek S., Devaux S., Herrmann A., Jachmich S. and Rapp J. 2011 *J. Nucl. Mater.* **415** S856–9
- [13] Balboa I. et al 2012 *Rev. Sci. Instrum.* **83** 10D530
- [14] Devaux S., Arnoux G., Eich T., Thomsen H., Brezinsek S., Coad P., Likonen J. and Stamp M. 2011 *38th EPS Conf. on Plasma Physics* O3.108
- [15] Barlow I. et al 2001 *Fusion Eng. Des.* **58–59** 189–93
- [16] Eich T., Herrmann A. and Neuhauser J. 2003 *Phys. Rev. Lett.* **91** 195003
- [17] Pamela S.J.P., Huysmans G.T.A., Beurskens M.N.A., Devaux S., Eich T., Benkadda S. and JET EFDA contributors 2011 *Plasma Phys. Control. Fusion* **53** 054014
- [18] Eich T. et al 2005 *J. Nucl. Mater.* **337–339** 669–76
- [19] Liang Y. et al 2011 *Nucl. Fusion* **51** 073001
- [20] Pearson J., Liang Y., Gimblett C., Reiser D., Sun Y., Zhang T. and Yang Y. 2012 *Nucl. Fusion* **52** 074011
- [21] Eich T., Reiser D. and Finken K. 2000 *Nucl. Fusion* **40** 1757–72
- [22] Nguyen F., Chendrih P. and Grosman A. 1997 *Nucl. Fusion* **37** 743
- [23] Lao L.L., John H.St., Stambaugh R.D., Kellman A.G. and Pfeiffer W. 1985 *Nucl. Fusion* **25** 1611
- [24] Wingen A., Evans T.E., Lasnier C.J. and Spatschek K.H. 2010 *Phys. Rev. Lett.* **104** 175001
- [25] Rack M., Wingen A., Liang Y., Spatschek K., Harting D., Devaux S. and JET-EFDA Contributors 2012 *Nucl. Fusion* **52** 074012
- [26] Wingen A., Evans T. and Spatschek K. 2009 *Nucl. Fusion* **49** 055027
- [27] Harbour P.J. et al 1989 *J. Nucl. Mater.* **162–164** 236–44
- [28] Kirk A., Lisgo S., Nardon E., Eich T., Herrmann A., Kallenbach A. and Loarte A. 2009 *J. Nucl. Mater.* **390–391** 727–32

Name of journal: Nuclear Fusion

Impact factor: 2.734 (2012)

Type of authorship: 1st

Own contribution: 90%

Details of contribution: Development and implementation of a movement correction algorithm for advancement of the data processing tool, analysis and interpretation of the experimental data, application of the thermoelectric current model, preparation and writing of the manuscript.

Modelling of LHW-induced helical current filaments on EAST: study of an alternative method of applying RMPs

M. Rack¹, L. Zeng^{1,2}, P. Denner¹, Y. Liang¹, A. Wingen³,
K.F. Gan², L. Wang², F.K. Liu², B. Shen², B.N. Wan², J.G. Li² and
the EAST Team

¹ Forschungszentrum Jülich GmbH, Institut für Energie- und Klimaforschung-Plasmaphysik, EURATOM Association, 52425 Jülich, Germany

² Institute of Plasma Physics, Chinese Academy of Sciences, Hefei 230031, People's Republic of China

³ Oak Ridge National Laboratory, PO Box 2008, Oak Ridge, TN 37831-6169, USA

E-mail: m.rack@fz-juelich.de

Received 28 June 2013, revised 31 January 2014

Accepted for publication 18 February 2014

Published 23 May 2014

Abstract

The lower hybrid wave (LHW) heating experiments at the Experimental Advanced Superconducting Tokamak (EAST) show a wide range of similarities to effects known from applied resonant magnetic perturbations (RMPs) by in-vessel or external magnetic perturbation coils. These observations suggest a current flow understood to be along scrape-off layer (SOL) field lines; here called helical current filaments (HCFs). For a better understanding of the experimental observations, a model to incorporate the magnetic perturbation of HCFs in the magnetic topology has been developed. Modelled SOL field lines, starting in front of the LHW antenna, show agreement in position and pitch-angle with the experimentally observed radiation belts. The comparison of the pick-up coil signals and the modelled HCFs' perturbation allows for determination of the current strength depending on the filaments' distance from the plasma edge. Agreement of predicted footprint structures with experimentally observed heat load and particle flux profiles at different toroidal angles in the divertor region is found. Based on the modelling results, the idea of LHW-induced RMPs, originating from the experimental observations, is strongly supported.

Keywords: resonant magnetic perturbations, lower hybrid waves, magnetic topology

(Some figures may appear in colour only in the online journal)

1. Introduction

Thermonuclear fusion is one possible future energy resource. The most developed machines for achieving thermonuclear fusion are magnetic confinement devices of the tokamak design. One of the requirements for a reactor, a steady-state operation, has not been achieved. Modern tokamaks, such as the Experimental Advanced Superconducting Tokamak (EAST) [1], focus on this aim. Current drive techniques are a key aspect [2–4]. During recent experiments, lower hybrid wave (LHW) induced magnetic perturbations have been observed, which indicates an additional non-axisymmetric current flow. An observation of scrape-off layer (SOL) currents induced by LHW was also found on Alcator C-Mod [5].

The EAST experiments with LHW show the appearance of helical radiation belts in the SOL which are well aligned with the LHW array once they pass the mid-plane [6, 7]. Furthermore, the number of radiation belts equals the number

of LHW antenna rows. The position of the helical radiation belts is determined to be in the SOL as they stay on the low field side (LFS) in a double-null plasma configuration. Those helical radiation belts are only observed if LHW heating is applied, especially in high-density plasmas. They become well pronounced with additional helium puffing. In addition, a splitting of both outer strike lines is seen, as well as the mitigation or even suppression of edge-localized modes (ELMs). Both effects resemble those of resonant magnetic perturbations (RMPs) [8–11].

This work discusses a modelling approach for LHW-induced helical current filaments (HCFs) located in the region where the radiation belts appear and studies HCF effects on the magnetic topology, which can lead to the described experimental observations. Further information on the experimental observations can be found in [6].

This paper begins by giving a brief overview of the field line tracing technique (section 2) which is the basis of the HCF

model. In the main part (section 3), the model approach and its parametric dependences are discussed with the focus on the effect on the magnetic topology. Finally, the application of the model to an EAST pulse and the agreement of predictions and measurements (section 4) are discussed. Section 6 provides a summary of the results and a conclusion of the investigations.

2. Field line tracing

Field line tracing is a standard technique for viewing and studying non-axisymmetric perturbations to magnetically confined plasmas [12–14]. It is based on the differential equations

$$\frac{dR}{d\varphi} = R \frac{B_R}{B_\varphi}, \quad (1)$$

$$\frac{dZ}{d\varphi} = R \frac{B_Z}{B_\varphi}, \quad (2)$$

where (R, φ, Z) are cylindrical coordinates, and $\vec{B} = (B_R, B_\varphi, B_Z)$ the total magnetic field. Magnetic fields can be expressed by the poloidal, ψ , and toroidal, F , fluxes via

$$B_R = -\frac{\partial\psi}{\partial Z} \frac{1}{R}, \quad (3)$$

$$B_\varphi = \frac{F}{R}, \quad (4)$$

$$B_Z = \frac{\partial\psi}{\partial R} \frac{1}{R}. \quad (5)$$

The simplest approach for the total magnetic field is the vacuum assumption. The magnetic field is calculated taking into consideration the toroidal field, the field produced by the plasma current, as well as fields of any shaping coils of the magnetic confinement device. This is commonly called the equilibrium reconstruction of the field, which is toroidally symmetric. Furthermore, non-axisymmetric perturbation fields are covered by the vacuum assumption. Throughout this work the perturbation of the error field is neglected as it is much smaller than the perturbation fields discussed later.

The limitation of the vacuum assumption is that no plasma responses, e.g. screening fields or resonant field amplifications, are included. Extensions have been developed to include further plasma effects [15, 16]. These are modelled as additional internal perturbation fields as a reaction of the plasma to the externally applied field or as a mock-up of internal modes. Throughout this work, plasma responses to additional applied fields are not considered. However, the model can be seen as an extension to the vacuum assumption to cover plasma responses to applied LHWs.

3. Model

Using the field line tracing technique, field lines in the SOL that start in front of the LHW antenna are modelled. The traced SOL field lines are found to agree in position and pitch-angle with the experimentally observed helical radiation belts (equilibrium reconstruction for EAST pulse 29 100 at 3500 ms used); see figure 1.

The qualitative agreement between the experimentally observed radiation belts and the modelled SOL field lines

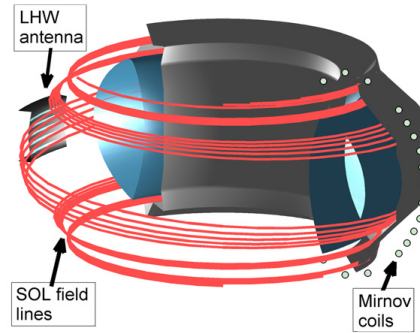


Figure 1. Sketch of the first wall of EAST (black) including the plasma shape taken from the equilibrium reconstruction of EAST pulse 29 100 at 3500 ms (blue). The solid lines give traced SOL field lines starting in front of the LHW antenna.

suggests that the radiation belts are field aligned. The formation of the HCFs is caused by a current flow along SOL field lines. By superimposing the equilibrium field with the magnetic field induced by line currents, the HCFs can be modelled and made accessible through the field line tracing technique. A further discussion of the implementation of each HCF is given in the appendix (for other applications of this method see also [15, 17, 18]). The helical current is understood to be a thermoelectric current flowing from one target tile to another, whereby the current flows only in the SOL. A possible trigger of these HCFs is discussed in [6] and is therefore not the focus of this work. This work presents the implementation of HCFs on the basis of a field line tracing code. Furthermore, the effects of HCFs on the magnetic topology of the plasma are discussed. As already presented in section 2, SOL field lines started in front of the LHW antenna with a certain distance from the last closed flux surface (LCFS) appear at the same position as the helical radiation belts discussed in [6]. However, the numerical implementation of the HCFs leaves a number of open parameters. These are (1) amount of current flow, $|I|$, (2) direction of current, $I/|I|$ (with respect to plasma current), (3) distance, d , from the LCFS and (4) spacing, Δz , between the HCFs.

Those parameters and their effects on the magnetic topology are discussed throughout the next subsections. Figure 2 indicates the meaning of the geometrical parameters d and Δz .

3.1. Amount of current flow

For the first part of this study, $\Delta z = 10$ cm is chosen as this equals the spacing between the LHW antennas which would seem to make it a reasonable choice. The distance from the LCFS is assumed to be $d = 10$ mm. This subsection focuses on the influence of the current amplitude.

The connection length plots [19] of the poloidal cross-section in figure 3 represent the magnetic topology at the same toroidal angle as the LHW antenna is positioned. An up/down symmetry is found for this double-null plasma shape, thus the presented calculations can focus only on the lower divertor region.

A. Publications included

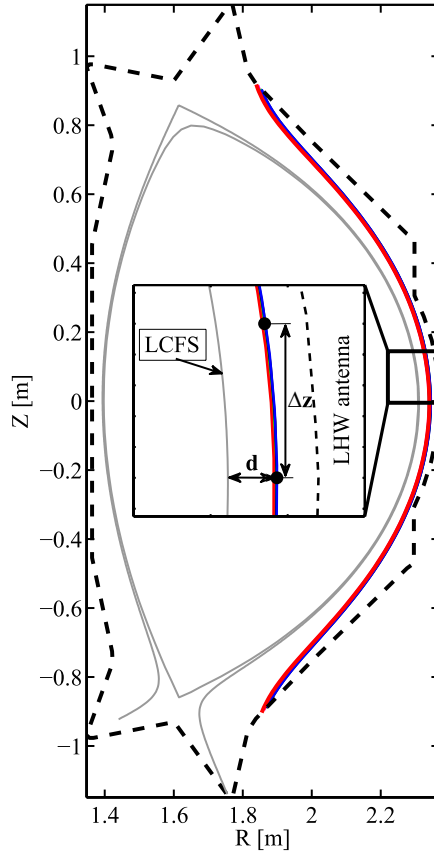


Figure 2. Poloidal projection of five SOL field lines starting in front of the LHW antenna. The black dots give the starting points at the toroidal angle $\varphi = 0$.

The presence of HCFs leads to significant changes in the magnetic topology. Consistent with the number of implemented HCFs, groups of five lobes each are found in the connection length plots. These groups of lobes elongate when they are closer to the X-points and consequently touch the wall at some distance from the original strike line. Such behaviour of X-point lobes is well known and studied in terms of RMP physics [20, 21].

In the two cases shown, an asymmetry is seen for the size of the lobes within one group. The lowest lobe in each group appears shorter than the uppermost lobe. This observation can be quantified by expressing the length of each lobe as the difference in poloidal flux between its tip and the separatrix, which yields a measure independent of the poloidal flux expansion. The second column of table 1 gives the relative lobe length for the 0.5 kA case normalized to the largest lobe at about $(R, Z) = (2 \text{ m}, -0.7 \text{ m})$. The asymmetry, confirmed by the measurement shown in table 1 (second column), can be explained based on simple considerations. Due to the geometrical configuration in the two cases shown,

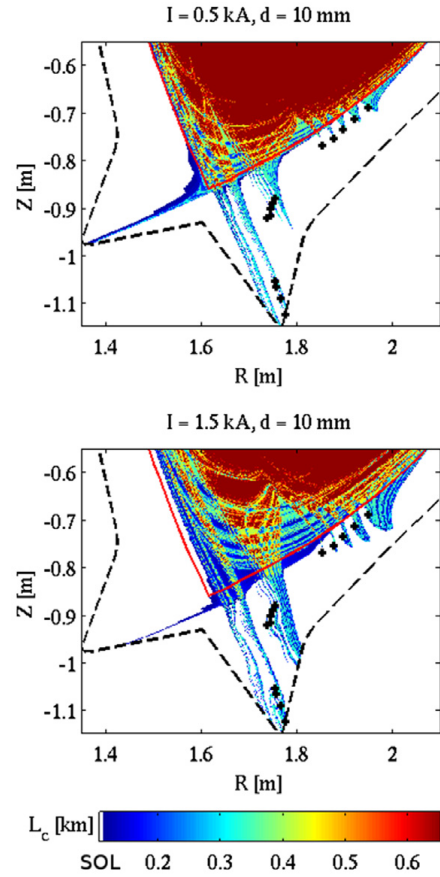


Figure 3. Connection length plots of the poloidal cross-section at the lower X-point regions for a helical current of 0.5 kA (top) and 1.5 kA (bottom). The solid line gives the LCFS of the unperturbed case and the crosses indicate the locations of the HCFs. The colour scale represents the connection length and is kept the same throughout this section of the paper.

Table 1. Lobe length relative to the longest lobe in a group in terms of poloidal flux. The lobes are numbered from bottom to top.

Lobe no.	0.5 kA case	1.5 kA case/0.5 kA case
1	0.139 ± 0.007	1.26 ± 0.29
2	0.382 ± 0.013	1.87 ± 0.16
3	0.554 ± 0.023	1.95 ± 0.11
4	0.772 ± 0.020	1.99 ± 0.07
5	1	1.97 ± 0.04

the uppermost lobe in each group experiences the strongest perturbation field in an outward direction as it feels the constructive contribution of all five HCFs. In contrast, the lowest lobe in a group experiences the strongest field in an inward direction. This causes the observed asymmetry of the lobe length in each group.

Clear changes can be seen for different current amplitudes. When increasing the current, the lobe size increases. The difference in the elongation of the lobe groups for different currents causes an increased broadening of the strike line for larger current amplitudes. A detailed study of the lobes within each group shows that for different currents, the increase in the lobe size appears to be different for different lobes. For instance, the lobe at the coordinates $(R, Z) = (2 \text{ m}, -0.7 \text{ m})$ seems to increase strongly in size, whereas the smallest lobe appears nearly unchanged. A quantitative study of the relative change in the lobe size with the current measured is given in the third column of table 1. The lobe lengths for the two cases are measured in terms of poloidal flux as described above. The length of the smallest lobe only increases by a factor of about 1.3, whereas the others are nearly doubled in size. The Melnikov integral [22, 24] suggests a linear increase with the source current of the perturbation, i.e. a similar relative increase for all lobes. Furthermore, an increase by a factor of three is predicted by the Melnikov integral as it is proportional to the perturbation current. Such a discrepancy between simulation results from field line tracing codes and the Melnikov integral has been seen before [23] for set-ups in which the source currents are located close to the separatrix. This discrepancy can be understood by considering that the Melnikov integral is a first-order approximation in current, which may no longer hold if the source current of the field is close to the point where the integral is evaluated.

A second effect that occurs with increased current amplitude is the deeper penetration of the chaotic layer into the plasma edge. This allows particles from further inside to propagate out of the plasma along the open field lines. As the HCFs are only positioned at the LFS, their effect on the plasma is limited to the outer strike line. The inner strike line does not show any splitting. Comparing the position of the inner strike line for the two discussed cases, a difference is seen. This is caused by a strong $n = 0$ component of the perturbation leading to a plasma shift.

3.2. Current flow direction

During the experiments at EAST, it was found via Mirnov coil measurements that the current through the HCFs flows in the same direction as the plasma current (same finding on Alcator C-Mod [5]). However, the trigger mechanism for this current is not completely understood and so it is not clear whether the current flow direction depends for instance on certain plasma parameters. Further experiments on this topic are needed to investigate this issue. Therefore, it is also worth discussing the effect of a reversed current flow through the HCFs.

A reversed current flow direction leads to significant changes in the magnetic topology (figure 4). The strong plasma shift in the X-point region (original LCFS in red) indicates the large $n = 0$ component, compare also figure 3 (bottom). In addition, the perturbation of the plasma edge is modified. The lobes create vortices which cannot be seen in the case of a co- I_p current flow direction. Additionally, the groups of lobes appear mirrored: regions of long connection length (green) are exchanged with the regions of shortest connection length (blue). This is a direct consequence of the argumentation discussed above. The tilting of the groups also changes. Small

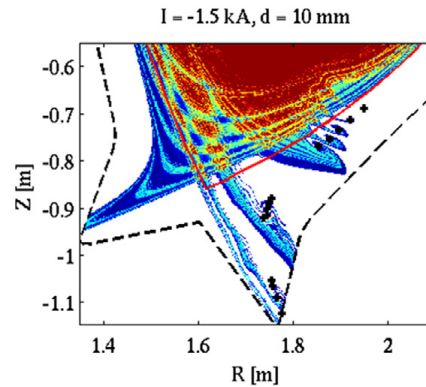


Figure 4. Same as figure 3 (bottom), but for a negative current.

lobes are less pronounced or vanish. This is a consequence of the plasma shift and a therefore larger distance of the HCFs from the plasma and will be discussed below. The separation between the different groups of lobes changes in such a way that a larger broadening of the strike line can be found for the co- I_p case.

3.3. Distance from LCFS

A parameter that cannot be directly measured from experimental viewing of the helical radiation belts is their distance from the LCFS. Via modelling, it was found that this distance has essential effects on the perturbation of the plasma edge. One effect on the topology is seen in the number of lobes per group, which reduces for larger d , as seen in figure 5. In addition to this, the lobes are pulled further out of the plasma and touch the wall far away from the original strike line, about 0.5 m for the case shown in figure 5 (bottom). This is a high safety risk for the plasma facing components as different wall materials are foreseen for the divertor and the first wall. An unexpected plasma-wall contact can cause severe damage. Considering these two main effects, we can summarize that the five HCFs appear to act as one strong HCF when they are located far away from the LCFS.

This effect can be further understood by calculating the spectrum of the applied perturbation for the different distances. Figure 6 shows the effective radial perturbation field for toroidal mode numbers, n , from 1 to 15 for the three previously considered distances of the HCFs. It can be seen that the lowest mode numbers have a similar amplitude in all three cases, but for highest mode numbers ($n = 10-15$) only the HCFs closest to the LCFS create a considerable perturbation. This explains the observations made via modelling where HCFs with $d = 42 \text{ mm}$ act more as a single filament at the plasma edge. Effective perturbations from higher mode numbers are required to create the group-like structures as seen for the other two cases.

A further effect to be mentioned is the variation in the length of the HCFs depending on d , see figure 7. The HCFs that are far away from the plasma will be shorter than those closer to the plasma. This has an influence on the poloidal

A. Publications included

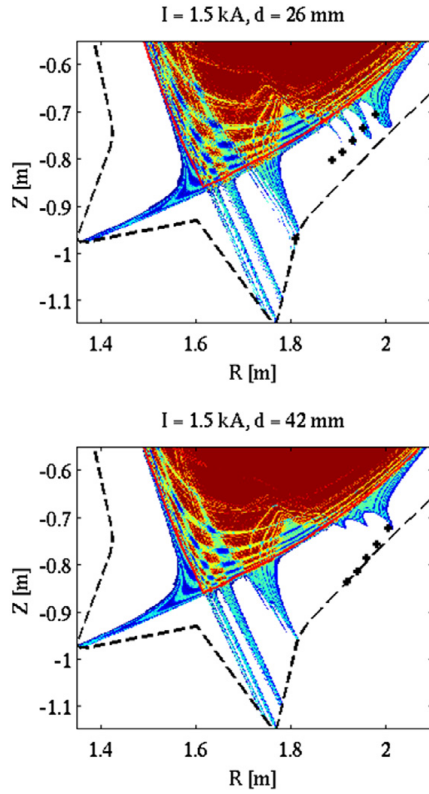


Figure 5. Same as figure 3 (bottom), but for larger distances of the HCFs from the LCFS, $d = 26$ mm (top) and $d = 42$ mm (bottom).

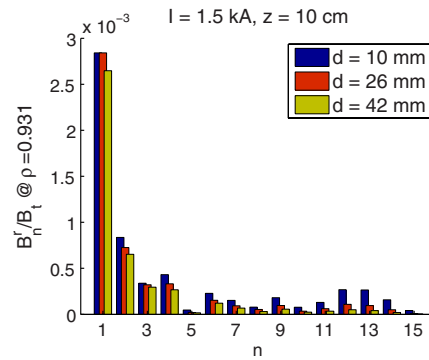


Figure 6. Comparison of the radial component of the perturbation field for the toroidal mode numbers, n , of the HCFs used in figure 3 (bottom) and figure 5.

current density of the HCFs. We can state that the amount of current, and the distance from plasma, of the HCFs influences the effective perturbation. For the effective perturbation, an expression of

$$\delta B \sim I_n(d) \quad (6)$$

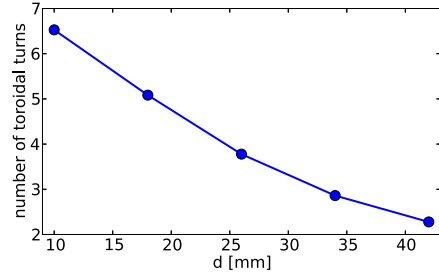


Figure 7. Relation of the distance of SOL field lines from the LCFS and their length. The SOL field lines closer to the wall will be shorter than those close to the plasma.

can be given, where l_n is the length of the HCFs in toroidal turns depending on their distance from the plasma.

A key requirement for the experimentally observed appearance of the radiation belts is that the HCFs are unaffected by their own perturbation field as they have to persist for very long time-scales. The perturbation also affects the SOL which could lead to a modification of the field lines on which the HCFs are aligned. This effect is visualized in figure 8 where the dashed-dotted line shows a perturbed field line which originally only stayed in the SOL and owing to the perturbation completes 2.5 poloidal turns. It shows that a certain distance from the LCFS is necessary to resemble the experimental observations. It also introduces a limitation on the current amplitude at distances d due to the dependence of the effective perturbation on both parameters.

3.4. Relation between distance and current amplitude

Based on experimental measurements, it is possible to analyse the relation of the distance and the current amplitude. Figure 9 gives the fit of the radial magnetic field of modelled HCFs to pick-up coil measurements at a fixed toroidal angle for different poloidal angles. Good agreement can be found for different sets of HCFs with distances $d \in \{8 \text{ mm}, 16 \text{ mm}, 23 \text{ mm}\}$. For each set of HCFs, a different current is found from the fit.

Figure 10 combines the fitting results for different distances so a relation $I \equiv I(d)$ can be determined. The relation shows two dominant effects. On the one hand, there is a radial decay of the perturbation field ($d > 12$ mm), and on the other hand, the influence of the plasma shift due to the $n = 0$ component ($d < 12$ mm). Only SOL field lines that stay on the LFS were analysed. The grey region marks the HCFs which would perturb themselves so they cannot remain for long time-scales.

Even though the distance of HCFs from the plasma is unknown, it can be related via $I(d)$ to the necessary current.

3.5. Spacing between HCFs

As a first approach, the spacing between the HCFs was assumed to be similar to the spacing of the LHW antenna rows ($\Delta z = 10$ cm). Although this sounds like a reasonable choice, it does not necessarily need to be true. A comparison of footprints with $\Delta z = 10$ cm and $\Delta z = 15$ cm is shown in

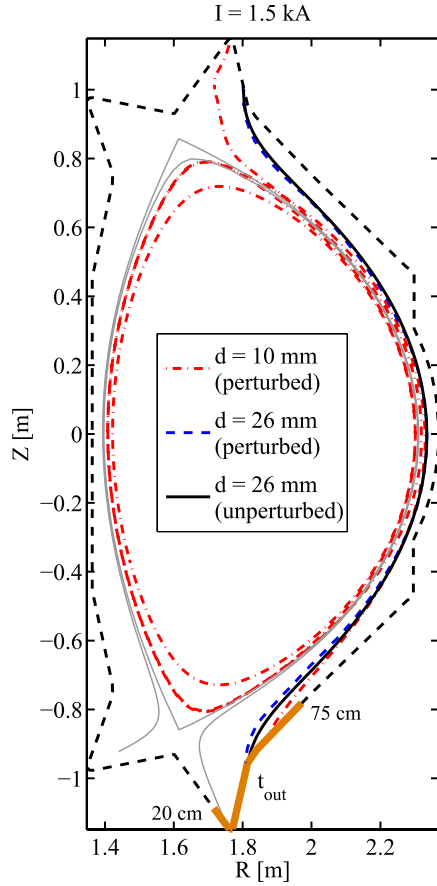


Figure 8. Poloidal projection of perturbed SOL field lines. The dashed-dotted ($d = 10$ mm) and the dashed ($d = 26$ mm) lines give the perturbed SOL field lines if HCFs with a current of 1.5 kA are present and the solid line a reference ($d = 26$ mm) without perturbation.

figure 11. The different spacing leads to significant changes in the footprint structures.

The separation between the lobes changes according to the spacing between the HCFs. For a larger spacing, the lobe lengths become more equal to each other. In addition, the lobes size is more similar. These effects indicate that the HCFs act more as individuals when the spacing is larger. Considering the experimental findings presented in [6] the larger Δz shows a better agreement than the case with $\Delta z = 10$ cm.

By comparing the radial components of the perturbation field, B_r^n , for different toroidal mode numbers, n , this effect can be further understood. Due to the special geometrical configuration of the HCFs, the dominant non-axisymmetric toroidal mode number is $n = 1$. Figure 12 shows the comparison of the radial components for spacings $\Delta z = 10$ cm and $\Delta z = 15$ cm. A reduction of the dominant mode amplitude can be found for the larger spacing and an increase for the

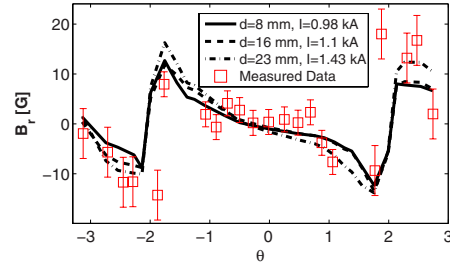


Figure 9. Fit of magnetic field of modelled HCFs to the experimentally measured field of pick-up coils at one toroidal position.

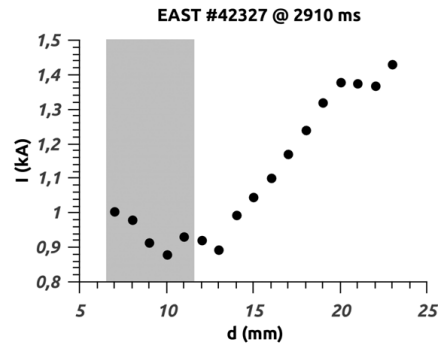


Figure 10. Dependence of the total HCF current on the distance from the LCFS based on the comparison with experimental measurements.

mode numbers $5 \leq n \leq 9$. This proves the idea that the HCFs act more as individuals for a larger spacing and explains the different appearance of the footprints.

4. Comparisons with heat and particle flux measurements

Following the MASTOC criterion [25] the predicted penetration depth, $1 - \psi_{\text{Min}}$, of a field line tracing model can be compared with measured heat and particle fluxes. Considering the studied parametric dependences we applied the HCF model to EAST pulse 42327. An equilibrium reconstruction of the plasma at 3900 ms is used with the model parameters: $I = 1.5$ kA, $d = 20$ mm, and $\Delta z = 10$ cm. Figure 13 shows a comparison of the predicted penetration depth with the measured heat (left) and particle flux (right) at two different positions.

The comparison shows a qualitative agreement for both toroidal positions. The experimentally found broadening of the footprint structure and its toroidally asymmetry can be described by the model presented here. The heat flux is measured at $\phi = 22.5^\circ$ and the particle flux at $\phi = 202.5^\circ$ with respect to LHW antenna. Although not the whole toroidal range can be experimentally viewed, the separation by 180° of the two measurement points gives a good overview and confirms that the dominant non-axisymmetric toroidal mode

A. Publications included

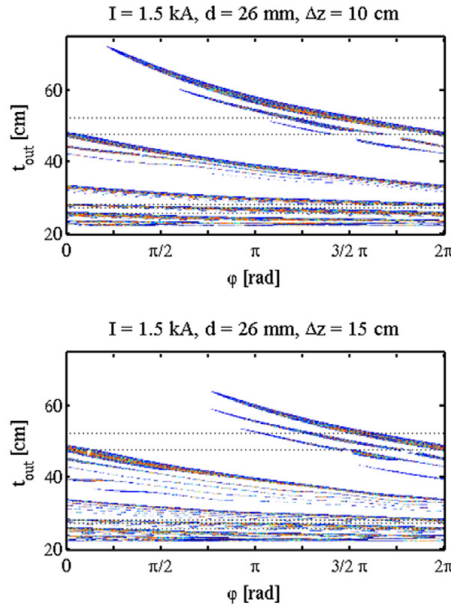


Figure 11. Connection length plots of the footprints for the same parameters as in figure 5 (top) with $\Delta z = 10$ cm (top) and $\Delta z = 15$ cm (bottom). The definition of the coordinate t_{out} is given in figure 8, φ is the toroidal angle. The dashed lines indicate the edges between the different divertor tiles.

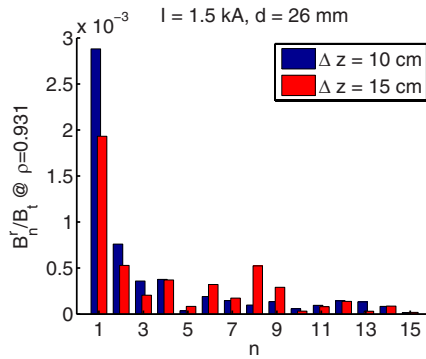


Figure 12. Same as figure 6, but for the HCFs used in figure 11.

number is $n = 1$. The agreement at both angles supports the correctness of the basic features of the model approach. A detailed comparison of the fine structures shows room for further optimizations, e.g. via experimental measurements of the current amplitude or considering plasma effects like screening.

5. Discussion

The model explains the effects that LHWs have on the magnetic topology. In particular, the effect on ELMS opens a new

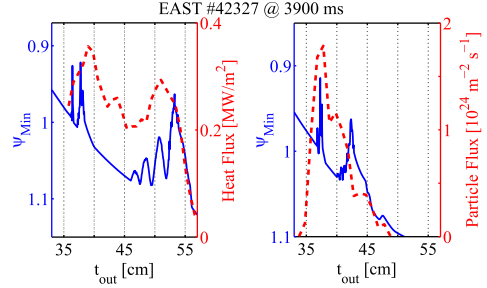


Figure 13. Comparison of the predicted penetration depth with the experimental heat (left) and particle (right) flux measured at different toroidal angles.

interesting field of fusion research. HCF-inducing LHWs could be an alternative method of ELM control, especially in future fusion power plants where internal perturbation coils may not be suitable. In addition, the RMPs applied by LHWs provide a much higher flexibility compared to fixed coil systems. The LHW geometry can be modified to optimize the perturbation spectrum for different purposes e.g. heat distribution and ELM control.

Other methods of creating RMPs without fixed coils have been discussed in the past [26, 27]. These methods are also based on the idea of driving a thermoelectric current in the SOL. The referenced publications discuss different methods of driving these thermoelectric currents by modifying the divertor properties. A key difference between those methods and the one presented here is the origin of the thermoelectric current. The source for the SOL current discussed in this work are spatially very localized, defined by the location of the LHW antenna. In contrast, the referenced publications describe large regions of the divertor being used to create the thermoelectric currents (e.g. via biasing). This causes the creation of surface currents rather than current filaments. A consequence is the possible degradation of the perturbation efficiency due to phase interference [27] which is not the case in the method presented here.

6. Summary and conclusions

The presented model approach demonstrates the effect of HCFs in the SOL on the plasma. A dependence of distance from the plasma and current of the HCFs was found based on the correlation of modelling and experimental measurements. Further dependences such as the current flow direction and spacing between the HCFs were discussed in terms of their effect on the plasma edge. From the studies, it can be concluded that, for a standard double-null and near double-null plasma configuration at EAST, the HCF currents flow in co- I_p direction and are in the range 1–1.5 kA, with a distance to the LCFS of 10–20 mm.

The presented studies were all made only for HCFs limited to the LFS as radiation belts on the high-field side (HFS) have not been observed at EAST. However, reports from Alcator C-Mod also describe LHW driven currents on the HFS, which will have further effects on the magnetic topology and can

cause splitting of the inner strike line. The presented model can be used to study the effect that HCFs will have on the HFS.

It also provides a basis for further studies on other devices where LHW heating is in use or planned, e.g. JET or ITER. For a further optimization of the model, tomographic methods could be applied to the visual observations of the radiation belts. This would allow the exact spacing of the radiation belts and their position in relation to the LCFS to be determined. The detailed study of the trigger mechanism of the currents via LHWs is needed to achieve a full understanding of the observations. Meanwhile, Langmuir probe measurements can be used to determine the thermoelectric current flow between the targets.

Acknowledgments

Many thanks to H. Frerichs for valuable discussions. M.R. thanks Evgenij Bleile and Götz Lehmann for the long lasting support. The financial support from the Helmholtz Association within the framework of the Helmholtz-University Young Investigators Group VH-NG-410 and the National Magnetic Confinement Fusion Science Program of China under Contract No 2013GB106003 is gratefully acknowledged.

Appendix. Implementation of the HCFs

For the discussions on the different model parameters presented in this paper, each HCF has been implemented as five virtual wires, carrying the same amount of current, see figure A1 (top). It is not clear whether this is a reasonable choice or not. Considering a resistivity of the plasma suggests that a representation of each HCF as an infinitely thin wire is unrealistic. However, depending on the focus of the study, the details of the implementation of such HCFs are not crucial for the results, as shown below.

Figure A1 shows the same footprint structure calculated with three different approaches for the current in the HCFs. The first footprint structure results from the assumption of infinitely thin HCFs, i.e. one virtual wire for each HCF. The disturbance of lobes due to strong local fields caused by the high current flowing through a single filament can be seen. Similarly, the vortices, seen in figure 4, are created due to strong near field effects. See also discussion in [18].

Another possibility for the implementation is the assumption of a finite width of the HCFs with a more equally distributed current per HCF. Figure A1 (top) sketches the used realization of a more equally distributed current per HCF with a diameter of 16 mm. The second footprint structure is calculated using this approximation. It results in a strong reduction of the near field effects and a much smoother appearance of the whole pattern. However, the envelope of the footprints including the length of the lobes remains nearly unchanged.

The last footprint structure results from an even higher number of 25 virtual wires distributed on a regular grid of 16 mm \times 16 mm. Such a further increase in the number of virtual wires does not strongly modify the resulting structure compared to the case with five virtual wires.

In summary, the usage of a single virtual wire per HCF results in strong near field effects at the target disturbing the

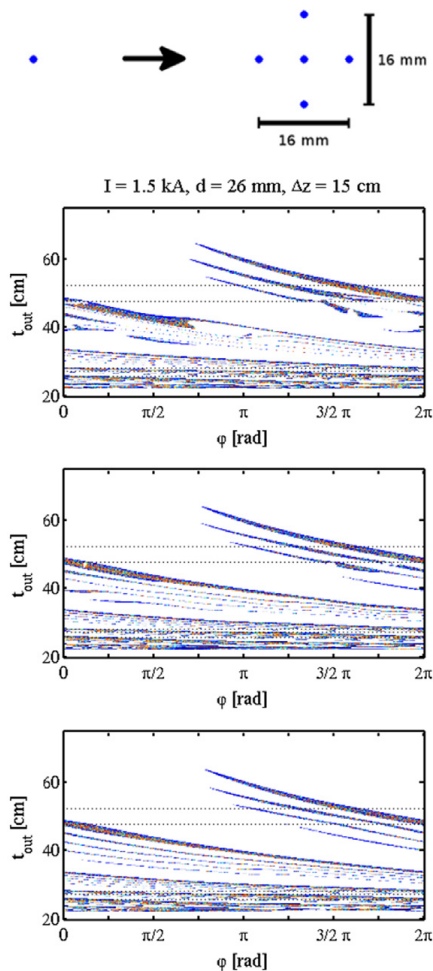


Figure A1. From top to bottom: sketch showing how each HCF is separated into several filaments, and footprints representing the resulting changes of the footprint structure with one, five and 25 filaments for each HCF.

footprint structure (e.g. at $t_{out} = 40$ cm, $\phi = 1.5\pi - 2\pi$ in figure A1 (upper footprint)). Multiple virtual wires per HCF reduce the near field effects as the current is more equally distributed. The length of the lobes is nearly unchanged. However, owing to weaker near field effects, the smaller lobes may get more pronounced and appear clearer. The number of virtual wires to choose depends on the total amount of current. In our given case, five virtual wires for each HCF appear to be sufficient without causing excessive computational costs.

The strong near field effects could be seen as non-physical artefacts, whereas the footprint using multiple filaments appears to be more regular. This would suggest that multiple filaments are needed. However, this is not proven and needs further experimental investigations in the given case. An

A. Publications included

alternative approach for implementing additional currents in the plasma edge/SOL is discussed in [23].

References

- [1] Wan B. and International Collaborators 2009 *Nucl. Fusion* **49** 104011
- [2] Fisch N.J. 1978 *Phys. Rev. Lett.* **41** 873–6
- [3] McWilliams R., Valeo E.J., Motley R.W., Hooke W.M. and Olson L. 1980 *Phys. Rev. Lett.* **44** 245–8
- [4] Ding B.J. *et al* 2011 *Phys. Plasmas* **18** 082510
- [5] Wallace G.M. *et al* 2010 *Phys. Plasmas* **17** 082508
- [6] Liang Y. *et al* 2013 *Phys. Rev. Lett.* **110** 235002
- [7] Gan K.F., Li M.H., Wang F.M., Gong X. and Zhang X.D. 2013 *J. Nucl. Mater.* **438** S364–7
- [8] Jakubowski M.W., Abdullaev S.S., Finken K.H. and the TEXTOR Team 2004 *Nucl. Fusion* **44** S1
- [9] Harting D.M. *et al* 2012 *Nucl. Fusion* **52** 054009
- [10] Evans T.E. *et al* 2004 *Phys. Rev. Lett.* **92** 235003
- [11] Liang Y. *et al* 2007 *Phys. Rev. Lett.* **98** 265004
- [12] Finken K.H., Eich T. and Kaleck A. 1998 *Nucl. Fusion* **38** 515
- [13] Wingen A., Evans T.E. and Spatschek K.H. 2009 *Phys. Plasmas* **16** 042504
- [14] Nardon E. *et al* 2011 *J. Nucl. Mater.* **415** S914–7
- [15] Wingen A., Evans T.E., Lasnier C.J. and Spatschek K.H. 2010 *Phys. Rev. Lett.* **104** 175001
- [16] Frerichs H., Reiter D., Schmitz O., Cahyna P., Evans T.E., Feng Y. and Nardon E. 2012 *Phys. Plasmas* **19** 052507
- [17] Buttery R.J., Hender T.C., Ashall J.D., Axon K.B., Blow G. and Fielding S.J. 1996 *Nucl. Fusion* **36** 1369
- [18] Wingen A., Evans T.E. and Spatschek K.H. 2011 *Phys. Plasmas* **18** 042501
- [19] Eich T., Reiser D. and Finken K.H. 2000 *Nucl. Fusion* **40** 1757–72
- [20] Evans T.E., Roeder R.K.W., Carter J.A., Rapoport B.I., Fenstermacher M.E. and Lasnier C.J. 2005 *J. Phys: Conf. Ser.* **7** 174
- [21] Kirk A., Harrison J., Liu Y., Nardon E., Chapman I.T. and Denner P. 2012 *Phys. Rev. Lett.* **108** 255003
- [22] Wiggins S. 2003 *Introduction to Applied Nonlinear Dynamical Systems and Chaos (Springer Texts in Applied Mathematics)* (Berlin: Springer) chapter 28
- [23] Cahyna P. and Nardon E. 2011 *J. Nucl. Mater.* **415** S927–31
- [24] Joseph I. *et al* 2008 *Nucl. Fusion* **48** 045009
- [25] Nguyen F., Ghendrih P. and Grosman A. 1997 *Nucl. Fusion* **37** 743
- [26] Joseph I. and Rognlien T.D. 2011 *J. Nucl. Mater.* **415** S932–5
- [27] Joseph I., Cohen R.H. and Ryutov D.D. 2009 *Phys. Plasmas* **16** 052510

Name of journal: Nuclear Fusion

Impact factor: 2.734 (2012)

Type of authorship: 1st

Own contribution: 85%

Details of contribution: Development of the model on the basis of an existing field line tracing code, application of the model to EAST discharges using equilibrium reconstructions provided, comparison with existing experimental data, interpretation of RMP spectra calculations provided, preparation and writing of the manuscript.

Magnetic Topology Changes Induced by Lower Hybrid Waves and their Profound Effect on Edge-Localized Modes in the EAST Tokamak

Y. Liang,^{1,*} X. Z. Gong,² K. F. Gan,² E. Gauthier,³ L. Wang,² M. Rack,¹ Y. M. Wang,² L. Zeng,^{1,2} P. Denner,¹ A. Wingen,⁴ B. Lv,² B. J. Ding,² R. Chen,² L. Q. Hu,² J. S. Hu,² F. K. Liu,² Y. X. Jie,² J. Pearson,¹ J. P. Qian,² J. F. Shan,² B. Shen,² T. H. Shi,² Y. Sun,² F. D. Wang,² H. Q. Wang,² M. Wang,² Z. W. Wu,² S. B. Zhang,² T. Zhang,² X. J. Zhang,² N. Yan,² G. S. Xu,² H. Y. Guo,² B. N. Wan,² J. G. Li,² and the EAST team

¹Forschungszentrum Jülich GmbH, Association EURATOM-FZ Jülich, Institut für Energie und Klimaforschung Plasmaphysik, Trilateral Euregio Cluster, D-52425 Jülich, Germany

²Institute of Plasma Physics, Chinese Academy of Sciences, Hefei 230031, China

³CEA, IRFM, F-13108 Saint-Paul-lez-Durance, France

⁴Oak Ridge National Laboratory, P.O. Box 2008, Oak Ridge, Tennessee 37831-6169, USA

(Received 10 February 2013; published 4 June 2013)

Strong mitigation of edge-localized modes has been observed on Experimental Advanced Superconducting Tokamak, when lower hybrid waves (LHWs) are applied to *H*-mode plasmas with ion cyclotron resonant heating. This has been demonstrated to be due to the formation of helical current filaments flowing along field lines in the scrape-off layer induced by LHW. This leads to the splitting of the outer divertor strike points during LHWs similar to previous observations with resonant magnetic perturbations. The change in the magnetic topology has been qualitatively modeled by considering helical current filaments in a field-line-tracing code.

DOI: [10.1103/PhysRevLett.110.235002](https://doi.org/10.1103/PhysRevLett.110.235002)

PACS numbers: 52.55.Fa, 52.25.Fi, 52.55.Tn

A great challenge for fusion energy research and technology is to confine a burning plasma while maintaining tolerable steady state and transient heat and particle fluxes on plasma-facing components. When tokamak plasmas operate in a high-confinement (*H*-mode) regime [1], a significant increase in the plasma energy confinement time is observed. However, as a consequence, a steep plasma pressure gradient and an associated increased current density at the plasma edge could exceed a threshold value to drive magnetohydrodynamic instabilities referred to as edge-localized modes (ELMs) [2]. ELMs lead to quasiperiodic expulsions of large amounts of energy and particles from the confined region, which in turn could result in serious damage to plasma-facing components. The next generation fusion machines, like ITER and DEMO, will need a reliable method for controlling or suppressing large ELMs [3].

Resonant magnetic perturbations (RMPs), which change the magnetic topology of the confined plasma, have been applied to completely suppress ELMs in DIII-D [4], or to mitigate ELMs (increase ELM frequency and reduce ELM size) in JET [5], MAST [6], and AUG [7]. Although the physics mechanism is still unclear, experimental results from those different devices demonstrate that the magnetic topology plays a key role in plasma confinement, edge magnetohydrodynamic stability, and interactions between the plasma and the first wall, particularly with the divertor [4,7,8].

To date, in all existing RMP ELM mitigation or suppression experiments, the magnetic perturbations are induced by either in-vessel or external coil systems. In-vessel

perturbation coils have been considered and designed for ELM control in ITER. However, in future fusion reactors, like DEMO, in-vessel perturbation coils may not be feasible. Thus, ELM control through actively changing magnetic topology by other mechanisms offers an attractive solution for next generation tokamaks beyond ITER.

Recent results from the Experimental Advanced Superconducting Tokamak (EAST) [9] show that lower hybrid waves (LHWs) provide an effective means to mitigate or suppress ELMs by inducing a profound change in the magnetic topology, similar to the effect previously observed with RMPs [4,5]. In this Letter, the influence of LHWs on the ELM behavior and the heat load distribution on the divertor plates will be presented, along with the experimental observation of LHW-induced nonrotating helical current filaments (HCFs), flowing along the magnetic field lines in the scrape-off layer (SOL). Comparisons are also made between the observed three-dimensional (3D) edge magnetic topology induced by the HCFs and predictions from a field-line-tracing code.

EAST (major and minor radii of 1.85 and 0.45 m, respectively) was built for demonstrating long-pulse stable high-performance *H*-mode plasmas with ITER-like configuration and heating schemes, i.e., with a flexible selection of double null, lower single null (SN), or upper SN poloidal divertor configurations and dominant radio frequency heating. The LHW system [10], operating at 2.45 GHz with an array of 20 (4 columns and 5 rows) waveguide antennas, was installed at the low field side midplane. The maximum output power of the LHW system is 2 MW. It was originally designed for a core plasma

current drive by transferring momentum to the plasma via electron Landau damping with a peak parallel wave refractive index of ~ 2.1 , and can achieve long-pulse H -mode operations with or without additional ion cyclotron resonance heating (ICRH). However, similar to other experiments [11,12], significant LHW power can be lost at the plasma edge, especially in a high-density plasma, due to a complex problem of coupling between fast waves and plasma particles.

The influence of LHW on the characteristics of ELMs has been studied through the modulation of LHW power in an ICRH-dominated H -mode plasma as shown in Fig. 1. In this experiment, the target H -mode plasma with a lower SN configuration was established mainly by ICRH with the input power of 1 MW in a relatively high-density regime after a fresh lithium wall coating. The edge safety factor q_{95} is 3.8 with a toroidal plasma current I_p of 500 kA and a toroidal field B_t of 1.8 T. The bottom triangularity, δ_L , is 0.45. The central line-averaged density, $\langle n_e \rangle$, is $\sim 4.7 \times 10^{19} \text{ m}^{-3}$, and the Greenwald fraction is ~ 0.9 . The H factor (H_{98y}) obtained during the H -mode phase is ~ 0.8 .

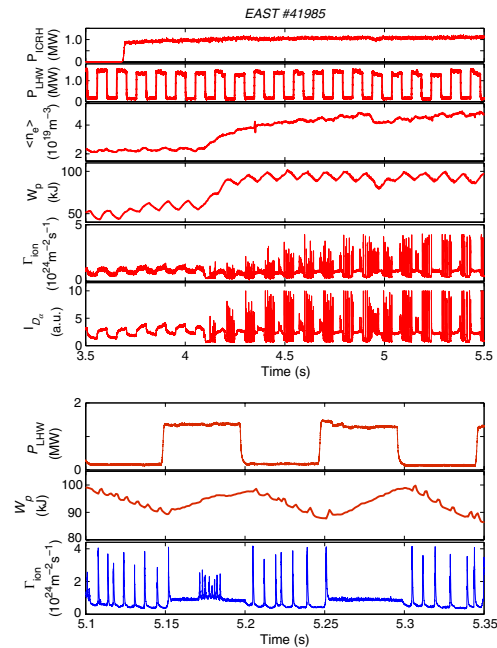


FIG. 1 (color online). Effect of LHW power modulation on ELMs. The time traces from top to bottom are injected power from ICRH and LHW, central line-averaged density, plasma stored energy, peak particle flux, and intensity of D_α emissions in the outer divertor. At the bottom is a focused view of LHW power, stored energy, and peak particle flux in the outer divertor.

The LHW power was set at 1.3 MW and modulated at 10 Hz with a 50% duty cycle. Thus, the duration of the LHW-off phase is 50 ms, which is about half of the energy confinement time. Without LHW, the ELM frequency is fairly regular at ~ 150 Hz. When LHW is switched on, the ELMs disappear or sporadically appear with higher frequency ~ 600 Hz as seen in Fig. 1 (lower panel). A significant reduction in the ELM peak particle flux by a factor of ~ 2 and an increase in the inter-ELM particle flux by a factor of ~ 2 (but still lower than that in the L -mode phase) have been observed on the divertor plate during the application of LHW. The plasma stored energy W_p was increased by a factor of 2 from ~ 50 to ~ 100 kJ once the H mode was established, and varied slightly (within $\pm 5\%$) following the modulation of LHW power. A quick reduction in the divertor ion flux can be clearly seen when the LHW was switched off. This may indicate the LHW power was absorbed not only in the core plasma but also deposited in the SOL.

Five helical radiation belts (HRBs) have been observed in the SOL during the application of LHW in both L -mode and H -mode plasmas on EAST. The number of HRBs is the same as the number of rows of the LHW antenna. Helium gas has been used to make the structure of the HRBs clear without changing its general features. As a typical example, Fig. 2 shows two tangential visible images taken during a helium plasma discharge from different sides of the EAST torus during the application of LHWs. The target plasma ($I_p = 300$ kA, $B_t = 2$ T, $q_{95} \sim 8$) was heated by LHW with a power of 0.7 MW in a double null configuration. The gap between the plasma separatrix and the outer limiter at the midplane is ~ 8 cm. The HRBs flow through the SOL at the low field side toward both upper and lower outer divertors along field lines in front of the antenna. Modeled SOL field lines, starting at 1 cm away from the original separatrix in front of the LHW antennas, show a good agreement in position and pitch angle with the experimentally observed HRBs.

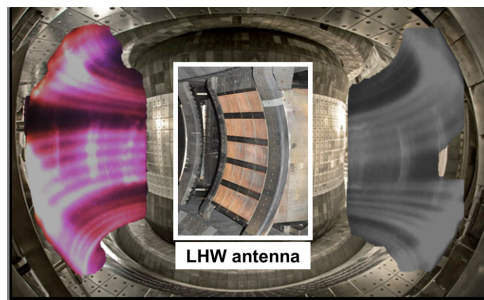


FIG. 2 (color online). Image of helical radiating belts induced by LHW superimposed on the EAST torus chamber. Photo of the LHW antenna on EAST (middle).

A. Publications included

PRL **110**, 235002 (2013)

PHYSICAL REVIEW LETTERS

week ending
7 JUNE 2013

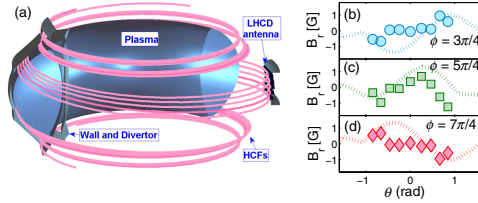


FIG. 3 (color online). (a) The sketch of the HCF modeling and the poloidal profiles of the LHW-induced nonaxisymmetric radial perturbation fields measured at different toroidal sectors with (b) $\phi = 3\pi/4$, (c) $\phi = 5\pi/4$, and (d) $\phi = 7\pi/4$. Here, the poloidal angle θ is defined as starting from the midplane at the low field side and is positive in the clockwise direction. The toroidal angle ϕ starts from the sector containing the LHW antennae in the counter-clockwise direction when viewing the EAST torus from the top. The simulated nonaxisymmetric radial perturbations using the modeled HCFs with a total filament current of 1.3 kA induced by LHW are also plotted.

Magnetic perturbations induced by the currents flowing in these edge helical filament structures (so-called HCFs) have been measured by a set of Mirnov coils during the modulation of LHWs. In this experiment, LHW power was modulated with a square wave from 0 to 1.2 MW, with a repetition rate of 100 Hz and a duty cycle of 50%. The formation of HCF currents was rather quick, i.e., within ~ 2 ms, which corresponds to the ramp-up time of the LHW. At the start of the LHW, ramp-down HCF currents diffused away within a few ms. The HCF-induced magnetic perturbations are poloidally and toroidally asymmetric, indicating the 3D distortion of the plasma topology. Simulated perturbation fields using the modeled HCFs can reproduce the Mirnov coil signals, as shown in Fig. 3. Here, the HCFs are modeled as currents flowing in the HRBs as seen in Fig. 3(a). The total HCF current can be determined by fitting the simulated perturbation field to the measured one, and is found to be ~ 1.3 kA in this experiment.

Splitting of the divertor strike points (SP) was observed during the application of LHW with similar effects to those reported for RMPs [13], as manifested in the heat load pattern on the divertor plate; see Fig. 4. The surface temperature on the outer lower divertor plate measured by an infrared (IR) camera during LHW shows a distinct multiple splitting of the original SP. The distance between the secondary and original SPs depends on the toroidal angle, indicating the 3D feature of the magnetic topology caused by LHW. In addition, the splitting of the SP depends on the edge safety factor as well, which was not observed in either Ohmic or ICRH plasmas.

The change in magnetic topology has been qualitatively modeled by considering the HCFs in a field-line-tracing code as shown in Fig. 5. The connection lengths of the magnetic field lines are calculated using an experimental equilibrium superimposed with a perturbation field from the HCFs with a total measured filament current of 1.3 kA.

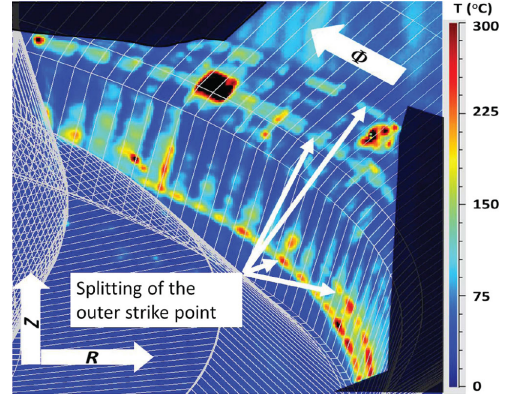


FIG. 4 (color online). IR image of the outer lower divertor plate in a toroidal range of $\phi = 1.3\pi - 1.5\pi$ rad during the application of LHW. Splitting of the original outer SP was shown as a multiple striated heat pattern on the divertor plate. A mesh plot of the wall is superimposed as white lines on the image. The toroidal asymmetry of the SP splitting can be observed.

The fields produced by the HCFs form several lobes of field lines with a long connection length near the X point, which can directly reach the outer divertor plate, resulting in the splitting of the SP, as identified by an IR camera. The calculated results show that strong modifications of the plasma edge depends on the edge safety factor, as well as the amplitude of currents flowing in these filaments.

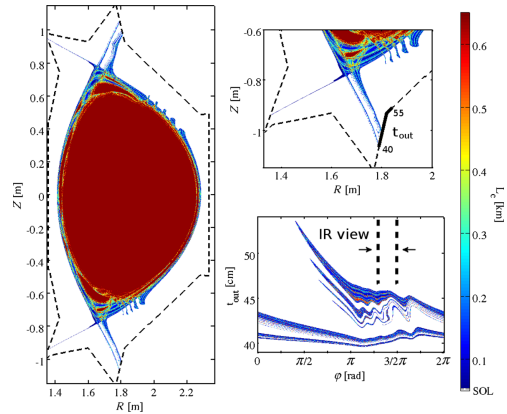


FIG. 5 (color online). Contour of connection length on the full poloidal cross section and expanded view of the bottom divertor region at $\phi = 1.3\pi$ rad, as well as a calculated footprint on the outer divertor plate as a function of the toroidal angle. Here, the calculation was carried out using the equilibrium reconstructed from the experiment shown in Fig. 4, with the IR viewing region indicated.

235002-3

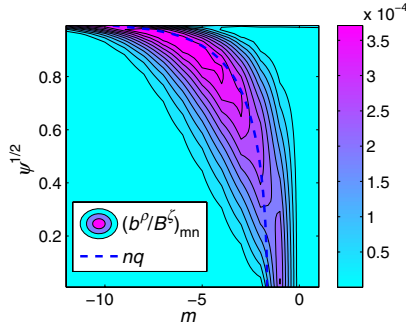


FIG. 6 (color online). Radial component of the $n = 1$ helical mode spectrum calculated with 1 kA HCF current. m is the poloidal mode number, and Ψ is the normalized poloidal flux. The calculation is based on the same equilibrium reconstruction for an EAST pulse shown in Fig. 4. Pitch resonant modes with $m = nq(\Psi)$ are shown by the dashed line.

It should be noted that the HCF model does not take into account the plasma response, and the modeling results can only qualitatively explain the HCF-induced strike point splitting.

Previous experimental results have shown that LHW can produce dithering ELM H modes in SN divertor plasmas on JET [14] and an ELM-free H mode in limiter plasmas on JT-60 [15]. However, the physical mechanism has not been investigated in detail. On EAST, a stationary ELM H mode with mixed type-I and small ELMs can be obtained with an application of stationary LHW power to the ICRH-dominated plasmas in a relatively low-density regime ($n_e/n^{GW} < 0.5$). Here, n^{GW} is the Greenwald-density limit. By decreasing the ratio of ICRH to LHW power and increasing plasma density, a stationary small ELM H -mode regime has been achieved and sustained for 32 s. The new evidence of HCFs induced by the LHW and its effects on the magnetic topology provide a possible explanation for why LHW mitigates or suppresses ELMs and induces a significant change in the heat load pattern on the divertor plate. For an understanding of the physical mechanism behind this, the dependences of LHW ELM mitigation on (i) the lithium wall coating [16], (ii) plasma pedestal collisionality, and (iii) q_{95} will be performed in future EAST experiments.

Because of the geometric effect of the LHW antenna, the perturbation fields induced by the HCFs are dominated by the $n = 1$ components, where n is the toroidal mode number. The magnetic perturbation spectrum calculated based on the experimental parameters indicates a good resonant feature, whereby the plasma edge resonant surfaces are well aligned on the ridge of the spectrum as shown in Fig. 6. In addition, the HCF-induced magnetic perturbations are located more at the plasma edge, without significantly affecting the plasma core. This is mainly

because the HCFs flow along the magnetic field lines in the SOL; thus, the helicity of the HCFs always closely fits the pitch of the edge field lines for whatever the plasma edge safety factor is.

It is to be mentioned that the currents in the SOL induced by LHW have been observed on several devices [11,12], however, the physical mechanism is still unclear. On Alcator C-Mod, the direction of the currents in the SOL did not change when the direction of LHW injection was reversed [11]. The estimated current in the SOL can be up to ~ 20 kA with a LHW power of 850 kW in a high-density regime on Alcator C-Mod, while the poloidally integrated total HCF current is ~ 7 kA with a LHW power of 1.3 MW on EAST. A simulation using the GENRAY-CQL3D code package [11] with a two-dimensional SOL model including the effects of collisional damping shows that about 10% of LHW power can be deposited in the SOL in the high-density plasmas on EAST. The experimentally observed currents in the SOL are far too large to be explained by direct current drive via collisional absorption of the LHW [12]. Note, however, that the absorption of LHW in the SOL could contribute to an increase in the ionization rate for neutrals in the divertor region, thus enhancing the thermoelectric current flowing along the SOL field lines from the hotter, less dense divertor plate to the colder, denser divertor plate.

On EAST, preliminary results show that the amplitude of the HCF current increases with an increase in either the LHW power or the plasma density. However, the radial location of the HCFs mostly stays near the separatrix in the SOL, where the connection length of field lines is much longer than the electron mean-free path. To achieve active control of the ELMs and heat load distribution on the divertor plates by LHW, parametric dependence of the HCF currents will be further investigated on EAST.

In summary, strong influence of LHWs on ELMs has been demonstrated on EAST, showing that the ELMs disappeared or sporadically appeared with increased frequency from ~ 150 to ~ 600 Hz when LHW was applied. LHW appears to induce a profound change in the magnetic topology by driving the nonrotating HCFs flowing along the magnetic field lines in the SOL. This leads to the splitting of the divertor SP with effects similar to those produced by RMPs. The observed change in topology is well reproduced by considering the HCFs in a field-line-tracing code. This offers a new attractive means to optimize the heat load distribution on the divertor plates and to suppress or mitigate the large transit peak heat and particle loads due to ELMs for the next-step fusion reactors (ITER and DEMO).

This work was supported by the National Magnetic Confinement Fusion Science Program of China under Contracts No. 2013GB106003 and No. 2011GB107001. Support from the Helmholtz Association in the frame of the Helmholtz-University Young Investigators Group VH-NG-410 is gratefully acknowledged.

A. Publications included

PRL **110**, 235002 (2013)

PHYSICAL REVIEW LETTERS

week ending
7 JUNE 2013

- *y.liang@fz-juelich.de; www.fz-juelich.de
- [1] F. Wagner *et al.*, *Phys. Rev. Lett.* **49**, 1408 (1982).
 - [2] J. W. Connor, *Plasma Phys. Controlled Fusion* **40**, 531 (1998).
 - [3] ITER Physics Basis Editors, ITER Physics Expert Group Chairs and Co-Chairs, and ITER Joint Central Team and Physics Integration Unit, *Nucl. Fusion* **39**, 2137 (1999).
 - [4] T. E. Evans *et al.*, *Nat. Phys.* **2**, 419 (2006).
 - [5] Y. Liang *et al.*, *Phys. Rev. Lett.* **98**, 265004 (2007).
 - [6] A. Kirk *et al.*, *Nucl. Fusion* **50**, 034008 (2010).
 - [7] W. Suttrop *et al.*, *Phys. Rev. Lett.* **106**, 225004 (2011).
 - [8] Y. Liang, C. G. Gimblett, P. K. Browning, P. Devoy, H. R. Koslowski, S. Jachmich, Y. Sun, and C. Wiegmann, *Phys. Rev. Lett.* **105**, 065001 (2010).
 - [9] J. G. Li and B. N. Wan, *Nucl. Fusion* **51**, 094007 (2011).
 - [10] B. J. Ding *et al.*, *Phys. Plasmas* **18**, 082510 (2011).
 - [11] G. M. Wallace *et al.*, *Phys. Plasmas* **17**, 082508 (2010).
 - [12] R. McWilliams, E. J. Valeo, R. W. Motley, W. M. Hooke, and L. Olson, *Phys. Rev. Lett.* **44**, 245 (1980).
 - [13] D. M. Harting, Y. Liang, S. Jachmich, R. Koslowski, G. Arnoux, S. Devaux, T. Eich, E. Nardon, D. Reiter, and H. Thomsen, *Nucl. Fusion* **52**, 054009 (2012).
 - [14] F. X. Söldner *et al.*, *Europhys. Conf. Abstr.* **22**, 1190 (1998).
 - [15] S. Tsuji *et al.*, *Phys. Rev. Lett.* **64**, 1023 (1990).
 - [16] J. M. Canik *et al.*, *Nucl. Fusion* **50**, 034012 (2010).

235002-5

Name of journal: Physical Review Letters

Impact factor: 7.943 (2012)

Type of authorship: contributing

Own contribution: approx. 15%

Details of contribution: Modelling of the helical current filaments in the scrape-off layer, study of the effect of the helical current filaments on the magnetic topology, investigation of the influence of the changed topology on the divertor strike-line splitting with qualitative comparison to the experimental data, contribution towards preparation of the manuscript.

A. Publications included

A long-pulse high-confinement plasma regime in the Experimental Advanced Superconducting Tokamak

J. Li, H. Y. Guo, B. N. Wan, X. Z. Gong, Y. F. Liang, G. S. Xu, K. F. Gan, J. S. Hu, H. Q. Wang, L. Wang, L. Zeng, Y. P. Zhao, P. Denner, G. L. Jackson, A. Loarte, R. Maingi, J. E. Menard, M. Rack and X. L. Zou

Nature Physics, **9**, 817–821 (2013)

Name of journal: Nature Physics

Impact factor: 19.352 (2012)

Type of authorship: contributing

Own contribution: approx. 10%

Details of contribution: Explanation of the observed strike-line splitting by modelling the helical current filaments, theoretical support of the idea to understand the experimentally observed control of heat distribution to different strike-regions by additional puffing, providing model predictions for the study of the edge safety-factor dependence on the perturbation spectrum, contribution towards preparation of the manuscript.



A rotating directional probe for the measurements of fast ion losses and plasma rotation at Tokamak Experiment for Technology Oriented Research

M. Rack,¹ Y. Liang,¹ H. Jaegers,¹ J. Aßmann,¹ G. Satheeswaran,¹ Y. Xu,² J. Pearson,¹ Y. Yang,³ P. Denner,¹ and L. Zeng^{1,3}

¹Institute of Energy and Climate Research - Plasma Physics, Forschungszentrum Jülich GmbH, Association EURATOM-FZJ, Partner in the Trilateral Euregio Cluster, D-52425 Jülich, Germany

²Laboratoire de Physique des Plasmas - Laboratorium voor Plasmafysica, Association Euratom-Belgian state, Ecole Royale Militaire - Koninklijke Militaire School, Partner in the Trilateral Euregio Cluster, B-1000 Brussels, Belgium

³Institute of Plasma Physics, Chinese Academy of Sciences, Hefei 230031, China

(Received 25 April 2013; accepted 11 July 2013; published online 1 August 2013)

This work discusses a new directional probe designed for measurements of fast ion losses and the plasma rotation with a high angular resolution in magnetically confined plasmas. Directional and especially Mach probes are commonly used diagnostics for plasma flow measurements, and their applicability for the fast ion losses detection has been demonstrated. A limitation of static Mach probes is their low angular resolution. At the Tokamak Experiment for Technology Oriented Research, the angular resolution is strongly restricted by the finite number of available measurement channels. In a dynamic plasma, where instabilities can lead to local changes of the field line pitch-angle, plasma flow, or fast ion losses, a low angular resolution makes a precise data analysis difficult and reduces the quality of the measured data. The new probe design, the rotating directional probe, combines the features of early directional probes and Mach probes. It consists of two radially aligned arrays of nine Langmuir probe pins with each array facing opposite directions. During the measurement the probe head rotates along its axis to measure the ion saturation current from all directions. As a result, the rotating directional probe simultaneously provides an angular dependent plasma flow and fast ion losses measurement at different radial positions. Based on the angular dependent data, a precise determination of the current density is made. In addition, the simultaneous measurement of the ion saturation current at different radial positions allows for resolving radially varying field line pitch-angles and identifying the radial dynamic of processes like fast ion losses. [<http://dx.doi.org/10.1063/1.4816821>]

I. INTRODUCTION

Thermonuclear fusion is foreseen as one of the future energy resources. In the first 50 years of research, the main focus has been on axisymmetric magnetic confinement devices, for which the toroidal magnetic field is described as two-dimensional, assuming toroidal symmetry. Current developments tend to make a three-dimensional treatment of the magnetic field necessary, e.g., in stellarators and tokamaks with edge localized mode (ELM) control via resonant magnetic perturbations (RMPs).¹ The effects of such non-axisymmetric magnetic fields on the plasma and its confined particles are an open question. One of the key aspects is the fast ion confinement, since a sufficient α -particle confinement is needed for an ignition of the fusion plasma; for the study of this, highly suited diagnostics are needed.

Directional and Mach probes are commonly applied diagnostics for plasma flow measurements in magnetically confined plasmas.^{2,3} Their usability for fast ion losses measurements has been shown.⁴ For both usages, the difference between probe signals measured from Langmuir probe pins facing opposite directions contains the information about the asymmetric distribution of plasma parameters, including the plasma rotation and fast ion losses.

Langmuir probes are a simple, well established plasma diagnostics measuring the main plasma parameters: electron

temperature, density, and ion saturation current. They are used in various fields, apart from fusion, for the characterisation of magnetised and non-magnetised plasmas, e.g., space, medical, and industrial research.

The early directional probes, e.g., presented by Hudis and Lidsky,² used one channel for such measurements and were rotated during the discharge through 180° to measure the ion saturation current from both directions. This necessarily assumes that the plasma parameters are constant over a long time, i.e., before and after the rotation of the probe. More recent Mach probes⁵⁻⁷ consist of several Langmuir probe pins distributed around the probe head allowing for a measurement of the ion saturation current to the probe from different directions at the same time. Thus, an assumption of constant plasma parameters during the measurement is not necessary. In addition, an angular dependence of the ion saturation current can be detected, allowing for the simultaneous measurement of parallel and perpendicular plasma flows.

However, the angular resolution reached by these probes is low and often limited due to the number of available channels of the probe manipulator. Especially, at the Tokamak Experiment for Technology Oriented Research (TEXTOR),⁸ the number of channels for reciprocating probes is limited to 20 due to the technical specifications of the fast probe manipulator.⁹ Therefore, such a probe at TEXTOR can only

give a very rough angular dependence. A technique to achieve a much higher angular resolution is a rotating probe as presented by Dyabilin *et al.*¹⁰ The rotating Mach probe, described therein, measures the parallel and perpendicular plasma rotation at one radial position. This allows for a very accurate determination of the Mach number, but only at one radial location. It misses the radial dependence, e.g., the radial correlation of physical quantities such as fast ion losses, ELM filaments, and turbulence.

This paper describes a rotating directional probe which achieves a high angular resolution and a simultaneous measurement of the ion saturation current at different radial positions. The latter is of particular importance for obtaining the radial profile of the plasma rotation and fast ion losses, as well as the radial correlation of these quantities. The probe combines the rotation of a directional probe and the contemporaneous measurement of the ion saturation current from opposite directions of a Mach probe. During the rotation an angular dependent ion saturation current is measured. A radial profile covering 4.8 cm, with a spatial resolution of 6 mm, is provided. In this article, the design of the rotating directional probe (Sec. II) and the experimental set-up used for the probe measurements at TEXTOR (Sec. III) are described. The measurement technique (Sec. IV) and first results (Sec. V) for the fast ion losses and plasma rotation measurement are presented. The advantages and limitations of the rotating directional probe in comparison with static Mach probes are discussed (Sec. VI).

II. ROTATING DIRECTIONAL PROBE DESIGN

One of the key points in the design of such a probe is the materials used. Two main requirements exist for the probe head of the rotating directional probe: (1) it has to sustain a high heat load of plasmas, (2) it has to be mechanically stable to withstand the linear and rotary acceleration. In addition, low-Z materials are preferred to decrease impurities released to the plasma. For a sufficient plasma rotation measurement half a rotation turn is needed. This means that at the maximum rotation speed available the probe head has to stay in the plasma for at least 129 ms. Including the time taken to plunge to the measurement position the total plasma facing time will be 450 ms. An obvious advantage, compared to standard Mach probes, is the rotation which distributes the heat load equity around the probe head.

Boron nitride (HeBoSint) has been chosen for the probe head material due to its high temperature resistance. Its mechanical stability has been tested to be strong enough for a linear movement with 0.3 m s^{-1} and a maximum rotation speed of 4 Hz, so as not to harm the material. During the measurement of the plasma rotation, in an ohmic heated plasma, with the probe placed 3 cm inside the last closed flux surface (LCFS) an innocuous heat increase was noticed.

The probe head has a cylindrical shape with a cross-section diameter of 30 mm and a total length of 160 mm. Its modular design contains 14 segments: nine equipped with two Langmuir probe pins and five without probe pins; see Fig. 1. All segments are conjoined with two stainless steel screws that are sealed with boron nitride caps on the plasma

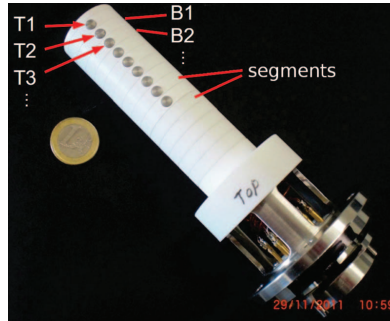


FIG. 1. Picture of the probe head. The probe consists of nine segments with two and five segments with no Langmuir probe pins. The Langmuir probe pins are labelled with T1, T2, T3, ... (seen in the picture) and B1, B2, ... on the opposite side of the probe head.

facing side. The probe pins on the one side are labelled as T1, T2, T3, ... and those facing in opposite directions as B1, B2, ... The radial distance between neighbouring Langmuir probe pins is 6 mm. Each probe pin is made out of tungsten and has a diameter of 4.55 mm. The copper wires attached to the Langmuir probe pins are isolated with ceramic plates connecting to the 20 pin feed through at the base of the probe head, to fit to the TEXTOR probe manipulator.

The Langmuir probes are operated in the ion saturation regime; a biasing of -176 V , against the TEXTOR liner is applied. For this purpose a battery array is used to keep the noise level as low as possible. A typical noise level for the system is less than 4 mA. The data acquisition uses a CT 1-T current transducer of the company LEM for the conversion of the measured currents to voltage signals and INCAA TR32 modules for the digitalisation of such. Data are acquired at 0.5 MHz to provide an accurate angular resolution of the measurement. The linear and rotary motion of the fast reciprocating probe is detected by standard potentiometers recorded by computer-automated measurement and control (CAMAC) modules.

The rotating directional probe is operated in two modes: (a) for fast ion losses detection and (b) for plasma rotation measurement. The fast ion losses are detected with the probe positioned outside of the LCFS. In the rotation measurement mode, the probe is positioned in a range of $r = 43 \text{ cm} - 48 \text{ cm}$ in the plasma edge. A combination of both modes is possible.

III. EXPERIMENTAL SET-UP

TEXTOR is a medium size tokamak with a major radius of 1.75 m and a minor radius of about 48 cm. It has a circular poloidal plasma cross-section. TEXTOR is equipped with neutral beam injection (NBI) and ion cyclotron resonance heating (ICRH) for an auxiliary plasma heating of 7 MW. The two NBIs are arranged tangentially, facing into opposite directions, allowing for independent control of the NBI heating and injection direction of fast particles, as it is used in our experiments to generate the fast ions. Its heating power is changed either via the aperture of the beam, which changes

A. Publications included

083501-3 Rack *et al.*

Rev. Sci. Instrum. **84**, 083501 (2013)

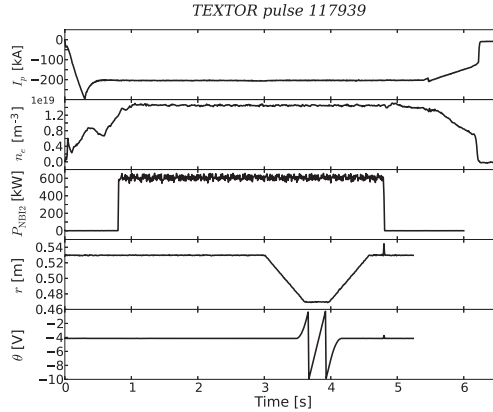


FIG. 2. Typical time-traces for a fast ion losses experiment with the rotating directional probe at TEXTOR. From top to bottom: the plasma current (I_p), the electron density (n_e), the power of the NBI 2 (P_{NBI2}), the radial probe position (r), and the rotation angle (θ).

the amount of injected neutrals, or by adjusting the acceleration speed, which influences the energy of the injected neutrals.

In the conducted experiments for fast ion losses and plasma rotation studies the typical plasma parameters at TEXTOR are core electron temperatures of 1.5 keV, and densities around $2 \times 10^{19} \text{ m}^{-3}$ at plasma currents of about 200 kA, and magnetic fields of 2 T. Figure 2 shows time-traces of a plasma discharge at TEXTOR with auxiliary NBI heating for inducing fast ions. In that discharge, the rotating directional probe is plunged to the position of minor radius $r = 47 \text{ cm}$. The probe rotation angle, θ , is given in the range of -10 V to 0 V , which corresponding to 0° – 360° . During this pulse the probe head is rotated by 720° , the first and last 180° are needed for the acceleration/deceleration of the rotation, the measurement takes place during the centre turn.

The probe head of the rotating directional probe is designed for the usage on the fast reciprocating probe at TEXTOR. The fast reciprocating probe is placed on the mid-plane of the low field side. It can move probes linearly in the radial direction along the mid-plane and rotate them along the probes head major axis. The linear movement is limited from $r = 53 \text{ cm}$ to 39 cm , at a speed of up to 5 m s^{-1} ; for the rotating directional probe a speed of 0.3 m s^{-1} is adequate. Its rotation reaches a frequency of around 4 Hz.

IV. MEASUREMENT TECHNIQUES

Each pair of Langmuir probe pins, mounted on opposite sides of one segment, measures the ion saturation currents in both co- (J_{Co}) and counter-current (J_{Ctr}) directions which are proportional to the parallel particle fluxes Γ , as sketched in Fig. 3.

Due to the rotation feature the ion saturation current detected on one Langmuir probe pin of the directional probe may provide the full information for both the co- and counter-

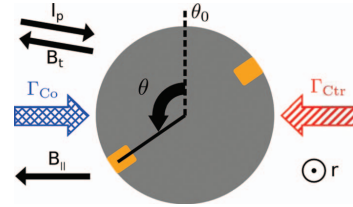


FIG. 3. Sketch of a segment of the rotating directional probe. One segment contains two Langmuir probe pins (orange). Both probe pins are facing into opposite directions to measure the co- and counter-going particle fluxes, Γ_{Co} and Γ_{Ctr} , simultaneously. The probe head rotates anti-clockwise (looking towards the core of the device). I_p and B_t give the toroidal plasma current and toroidal magnetic field direction, B_{\parallel} indicates the direction of the parallel component of the magnetic field, and r is the direction of the minor radius. θ is the rotation angle and θ_0 is the reference angle when the probe pin areas are perpendicular to the parallel flux.

going particle fluxes (for constant plasma parameters during the rotation); see Hudis and Lidsky.² Figure 4 shows the predicted signal of such a measurement, where I_{sat} is the ion saturation current and θ is the rotation angle. With non-changing plasma parameters a constant particle flow in the scrape-off layer (SOL)/plasma edge during the measurement can be assumed. The maximum current from each direction is detected when the Langmuir probe pin area stands normal to the particle flux direction. For a non-zero plasma flow in an ohmic plasma the particle flux differs from the co- and counter-current directions.

Furthermore, since the rotating directional probe is equipped with two Langmuir probe pins on each side only half a turn of the probe head is needed to measure the co- and counter-current going particle fluxes. Consequently, this brings two advantages: first, the measurement time is halved, which reduces the total thermal load on the probe head, second, the probe measurement becomes less frail for changes in the main plasma parameters. Local pitch-angle changes do not disturb the measurement.

As a result of the rotation of the probe head and the fast data acquisition, a precise angle dependence of the ion saturation current, $I_{\text{sat}} \equiv I_{\text{sat}}(\theta)$, is known. From this the current density, j , as a representative for the particle flux $\Gamma \sim j$ can be calculated. j can be substituted with either j_{Co} or j_{Ctr} depending on the angular position of the Langmuir probe pin that is

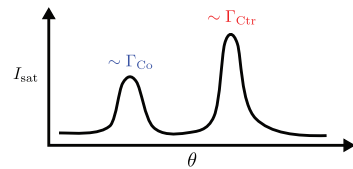


FIG. 4. Example for an ion saturation current measured by one Langmuir probe pin during the rotation of the probe head by 360° with non-zero parallel flow. I_{sat} is the measured ion saturation current and θ is the rotation angle of the probe. The two maxima are proportional to the parallel particle flux in co- (Γ_{Co}) and counter-current (Γ_{Ctr}) directions.

considered. For the current density j we know

$$j = \frac{I_{\text{sat}}(\theta)}{A_{\text{eff}}(\theta)}, \quad (1)$$

with A_{eff} , the effective area of the corresponding probe pin, and I_{sat} , the angle dependent ion saturation current measured from the co-/counter-side, respectively. The effective area can be written as $A_{\text{eff}} = A \sin(\theta - \theta_0)$, where A is the probe pin area. θ_0 gives the probe head angle at which A is perpendicular to the particle flux. With a well aligned probe, regarding the geometrical axis, the local pitch-angle can be determined from θ_0 . Following Eq. (1), the current density can be found by applying a sine fit to the measured data:

$$\frac{I_{\text{sat}}(\theta)}{A} = j \sin(\theta - \theta_0), \quad (2)$$

with the fitting parameters j and θ_0 .

Figure 5 shows the measured data and the fitting results (solid line) for a pair of Langmuir probe pins at $r = 45.2$ cm in an ohmic heated plasma. A mean square algorithm is used for the fit. The curve fits about half the measured data in its maximum region (45° – 135°), but fails near 0° and 180° , where higher saturation currents are measured than expected (cf. Refs. 10 and 11). This increase, when the normal of the probe pin area is perpendicular to the plasma flow direction, can be understood as “gyration hits” of passing ions. At that plasma region ions have a gyration radius of about 0.4 mm in ohmic TEXTOR plasmas. There guiding centre would pass the probe head, but due to their gyration they hit the Langmuir probe pins once it is in a perpendicular position to the plasma flow.

An approach to compensate the gyration hits and get more accurate values from the fit is an additional term in the fit function that takes perpendicular gyration hits into account.

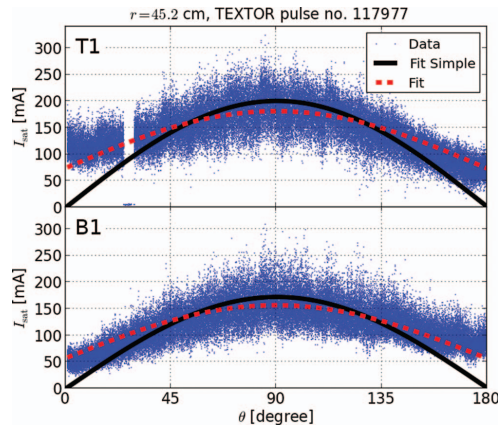


FIG. 5. Data of the rotating directional probe for two opposite facing Langmuir probe pins at $r = 45.2$ cm inside of the LCFs. The dots show the measurement, and the solid and dashed lines give the fitting curves. The dashed curve corrects for gyration hits of passing ions. The view is limited to half a turn of the probe head, since this contains the whole information on the plasma flow.

It extends Eq. (2) to

$$\frac{I_{\text{sat}}(\theta)}{A} = j \sin(\theta - \theta_0) + j_{\text{gyr}}[1 - \sin(\theta - \theta_0)], \quad (3)$$

with j_{gyr} representing the gyration hits. Similar to j , j_{gyr} is handled separately for each Langmuir probe pin. The comparison in Fig. 5 presents a much better fit resulting from this extended fit function (dashed line).

The spontaneous drop in the measured signal of the Langmuir probe on top of Fig. 5 at 30° originates from a technical trip of the electrical connection. Such a drop of the signal below the noise level does not effect the analysis as these regions are not taken into account for the fitting of the data.

The accurate determination of the current density from both sides, as described here, is the basis for the calculation of the fast ion losses and the plasma rotation. Discussions by Goubergen *et al.*¹² pointed out that j depends on the parallel and perpendicular flows $j \sim \exp\{v_{\parallel}/c_s - v_{\perp} \cot(\theta)/c_s - 1\}$, where v_{\parallel} and v_{\perp} are the parallel and perpendicular flow velocities and c_s is the ion sound speed. Following this, a consideration of the perpendicular flow is necessary for the calculations of the current density. During the measurement in the SOL in the presence of fast ion losses the parallel flow is strongly enhanced by the ion losses and becomes dominant over the perpendicular, $v_{\parallel} \gg v_{\perp}$ (see also discussion in Sec. IV A). Therefore, the perpendicular flow can be neglected and no θ dependence of j needs to be considered. However, during measurements in the edge of an ohmic plasma large perpendicular flows may appear that cannot be neglected. The application of the presented analysis technique is then strongly restricted to a θ -range ($80^\circ < \theta - \theta_0 < 100^\circ$) where the v_{\perp} -term becomes negligibly small. For determining the perpendicular flow, the method described in Refs. 10–12 needs to be applied which will not be further discussed here. Instead the main focus is on fast ion losses measurements.

With the knowledge of the current density from opposite facing probe pins the two physical quantities fast ion losses and plasma rotation can be calculated by taking the difference or ratio of the current densities, respectively. The fast ion losses measurements are performed with the probe head located in the SOL whereas the plasma rotation measurements take place in the plasma edge and SOL.

A. Fast ion losses measurement in the SOL

Nagaoka *et al.* presented the general applicability of a directional probe for the measurement of fast ion losses.⁴ Fast ions are generated with a tangential NBI for the performed experiments. The NBI will cause, on the one hand, fast ion losses and on the other hand, a change in the plasma rotation. In the SOL, the asymmetry caused by the fast ion losses is dominant over that caused by the plasma rotation, as sketched in Fig. 6(a), and therefore the asymmetry of the velocity distribution of the bulk plasma can be neglected in the analysis.

The hatched region in Fig. 6(a) corresponds to the amount of particles flowing in counter-current direction that are detected by one Langmuir probe pin and the cross-hatched

A. Publications included

083501-5 Rack *et al.*

Rev. Sci. Instrum. **84**, 083501 (2013)

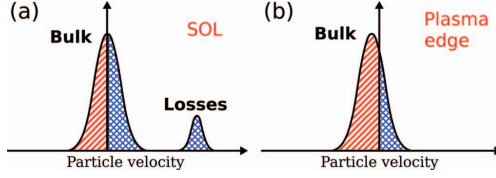


FIG. 6. Sketch of (a) the velocity distributions in the SOL of a beam heated plasma with a dominant fast ion losses contribution and (b) the velocity distribution in the edge of a counter rotating ohmic plasma. The hatched and cross-hatched regions correspond to the particle amount flowing in counter- and co-current direction, respectively. See Fig. 3 for further information on the flow directions with respect to the probe head geometry.

region corresponds to the co-going particles detected by the probe pin facing in the opposite direction (see Fig. 3 for a better visualisation of the flow direction with respect to the probe head). In a beam heated plasma, j_{Ctr} is the current density from the bulk ions and j_{Co} contains, in addition, a large fraction of the beam induced fast ion losses. The current density resulting from the fast ion losses, j_{loss} , can be evaluated by taking the difference of j_{Co} and j_{Ctr} :

$$j_{\text{Co}} = j_{\text{Bulk}} + j_{\text{loss}}, \quad (4)$$

$$j_{\text{Ctr}} = j_{\text{Bulk}}. \quad (5)$$

It follows for a beam heated plasma

$$j_{\text{loss}} = j_{\text{Co}} - j_{\text{Ctr}}, \quad (6)$$

as a measure for fast ion losses in the SOL.

B. Plasma rotation measurement

In an ohmic plasma, the rotating directional probe can be used to measure the local plasma rotation. Figure 6(b) shows a sketch of the velocity distribution in the edge of a counter rotating plasma. It gives the general idea on the background of the measurement.

From the ratio of the ion saturation current measured in co- and counter-directions the local Mach number, M , can be determined as a measure for the plasma rotation

$$M = k \ln \left(\frac{j_{\text{Co}}}{j_{\text{Ctr}}} \right), \quad (7)$$

with k a calibration constant taken as $k \approx 0.4$ based on the calculations for magnetised plasmas by Hutchinson.¹³ k depends on various plasma parameters, such as magnetic flux density and ion temperature,¹⁴ and cannot be calculated analytically for our cases in magnetised plasmas.

V. EXPERIMENTAL RESULTS

Figure 7 shows the fast ion losses measurement in a co-beam heated plasma for four TEXTOR pulses with reversed plasma current in the range -180 kA to -285 kA. A reversed toroidal magnetic field of -2.25 T at an electron density of $1.5 \times 10^{19} \text{ m}^{-3}$ has been used and 600 kW hydrogen NBI heating was applied at an acceleration voltage of $U = 50$ kV.

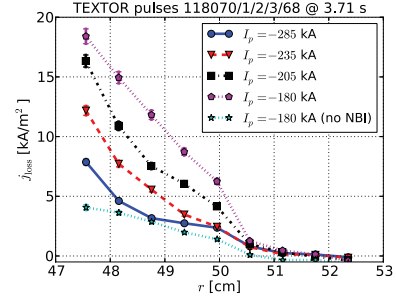


FIG. 7. Measured fast ion losses in a co-beam heated plasma. The dependence of fast ion losses on the plasma current is shown. A reference without beam induced fast ions is shown by the stars.

The observed plasma current dependence is in line with the known dependence of the critical loss energy of fast ions on the plasma current:¹⁵ $E_{\text{loss}} \sim I_p^2$. It can easily be understood by considering the reduced confinement at lower plasma currents. In addition, a clear radial decay of the fast ion losses can be observed for all cases with vanishing losses at around $r = 50.6$ cm. No losses can be detected further outside in this plasma configuration due to plasma facing components intercepting the fast ions.

In Fig. 8, the measurement of the plasma rotation, given as the Mach number, is shown. A slow counter rotation, $M \sim -0.1$, in the range of around $r \leq 46.3$ cm is found which then turns to a co-rotation and increases towards $M \sim 0.8$ at the LCFS. In the SOL, a radial decay of the plasma rotation can be observed. Similar trends are seen in other TEXTOR plasmas as discussed by Xu *et al.*¹⁶ The higher absolute values seen in the presented discharge (Fig. 8) result from a different plasma configuration, here reversed plasma current and toroidal field are used compared to standard TEXTOR discharges.

The denoted error bars result from the inaccuracy of the Langmuir probe pin area, which contains an error of about 5%, and the fit inaccuracy, usually around 1%. Inaccuracies of the data acquisition are below 1% and therefore not considered.

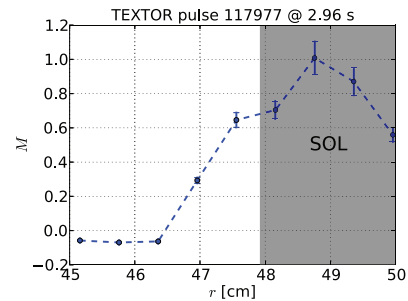


FIG. 8. Plasma edge and SOL Mach number measured in an ohmic plasma.

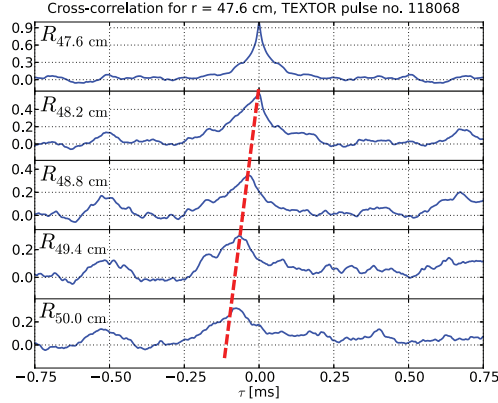


FIG. 9. Cross-correlation between the signal measured at $r = 47.6$ cm with signals measured further away from the plasma. The cross-correlations indicate the radial outward propagation of ion losses with a speed of about 200 m s^{-1} (marked by dashed line).

In addition to the fast ion losses and Mach numbers, the presented multi-pin directional probe may also provide further information about the radially dynamic of the plasma seen as high frequent modulations in the ion saturation current signal (cf. Fig. 5). These modulations can be found inside, as well as outside the LCFS. Fast changes in the ion saturation current can be caused by turbulences and magneto-hydrodynamic instabilities such as saw teeth, tearing modes, and ELMs. Figure 9 depicts the radial cross-correlation of the Langmuir probe pin signal at $r = 47.6$ cm with those measured by further outside probe pins. The presented TEXTOR pulse 118 068 has the probe set-up for the fast ion losses measurement, i.e., probe head in the SOL.

The cross-correlation is calculated based on

$$R_{xy}(\tau) = \frac{1}{T} \int_{-T/2}^{T/2} x(t) \cdot y(t + \tau) dt, \quad (8)$$

where x and y are the measured signals at different radial positions, and T is the considered time window for the correlation. The variable τ gives the lag between the signals.

For the given pulse, the cross-correlations allow us to determine the radial outward propagation of ion losses with a speed of around 200 m s^{-1} starting at a radial position between $r = 48.2$ cm and 48.8 cm. The analysis of the radial correlations has been widely used in the study of edge turbulence by Langmuir probes¹⁷ and is helpful in exploring the radial dynamic of other processes, e.g., in the characterisation of ELM filaments where the presented probe system can be applied as an additional tool to visual observation techniques.¹⁸ In addition, the radial correlation is a useful tool to gain the phase information of externally applied dynamic RMPs¹⁹ which is a major issue in the understanding of RMP physics and has been found to have a radial dependence.²⁰

VI. DISCUSSION AND CONCLUSION

The rotating directional probe is a suitable diagnostics for measurements in a non-axisymmetric dynamic magnetic field, e.g., with the applied dynamic ergodic divertor at TEXTOR. This is a strong advantage compared with earlier directional/Mach probes. The high angular resolution enables for a precise analysis of the ion saturation current, even in presence of dynamic perturbations. A precise adjustment of the probe head angle beforehand, as needed in the case of non-rotating probes to bring the probe pins in line with the parallel or perpendicular particle flow direction, is not necessary. The rotation of the probe head allows the whole angular dependence to be measured. Consequently, the maximum ion saturation current can be detected and, therefore, the fast ion losses and plasma rotation calculated. An angular misalignment or a local change of the pitch-angle does not perturb the measurements. Furthermore, radial changes in the pitch-angle, e.g., due to non-axisymmetric fields, can be detected. As the probe consists of an array with nine probe pins it measures a 4.8 cm radial profile of fast ion losses in the SOL and the plasma rotation. Compared to a static Mach probe or the rotating Mach probe, the measurement of the rotating directional probe takes place at different radial positions simultaneously, whereas for a standard Mach probe it can provide a higher resolved radial dependence during one plunge, but misses radial correlation of the signals from different radii. Due to the design of the rotating directional probe, the radial resolution of the measured profiles is 6 mm. To increase the radial resolution, the measurement is repeated in the same target plasma, shifting the probe by 1 mm each time. Thus a resolution of 1 mm is achieved; higher resolutions are unobtainable due to the limitations of the probe manipulator. This discomfort, compared to standard Mach probes, is a consequence of the probe design focussing on a high angular resolution.

The large radial range that can be covered by the rotating directional probe simultaneously is a strong achievement especially for the fast ion losses measurement. Previous results already showed the fast ion losses measurement with a directional probe at one radial position, but a radial dependent measurement of the fast ion losses could not be presented before. The precise knowledge of the radial dependence of fast ion losses helps for a further understanding of the processes responsible for the losses. Furthermore, the availability of simultaneously measured signals from different radial positions allows for estimating the radial cross-correlation of ion loss signals. The radial dynamic is valuable information for the investigation of the involved processes and becomes even more important in the presence of dynamic perturbations of the plasma.

Typical signal intensities of the rotating directional probe are in the order of a 100 mA with a signal to noise ratio below 4% . The sub-structures in Fig. 5 with ± 50 mA on top of the main signal are caused by fast intermittent events such as turbulences that can be further characterised using the presented probe, which is not in the scope of this publication.

Due to the good signal to noise ratio and the high time-resolution of 0.5 MHz, the rotating directional probe is also

A. Publications included

083501-7 Rack *et al.*

Rev. Sci. Instrum. **84**, 083501 (2013)

well suited for studying ELM filaments, and the effect of RMPs on those. The typical ELM frequencies measured at TEXTOR are in the range of several hundred hertz and the maximum RMP rotation frequency is 5 kHz. In ELM filament studies during a limiter high-confinement mode (H-mode) discharge the rotating directional probe measurements focus on the filament propagation through the SOL, thus the probe is positioned outside of the LCFS. Due to the strongly increased heat fluxes in the confined plasma a safe operation of the probe inside the plasma cannot be guaranteed during a limiter H-mode. With the probe outside of the plasma, the limiter takes the ELM heat loads and a safe operation of the probe is gained.

The usage of the rotating directional probe on the fast reciprocating probe at TEXTOR brings limitations for the presented probe which could be overcome by using an optimized probe manipulator. These limitations are: the maximum rotation speed of about 4 Hz, and the limit of 20 available channels for measurement signals. A faster actuator for the rotation will reduce the time needed for the probe to stay in the plasma at a fixed radial position. If there was a larger number of available measurement channels, the probe head could be equipped with further arrays of Langmuir probe pins positioned at different angles, which could be described as a rotating Gundestrup probe. Such an improvement also reduces the waiting time of the probe during the rotation. However, more Langmuir probe pins will bring difficulties in the construction of the probe head. Due to the limitations and technical difficulties outlined these improvements are not seen to be advantages for the measurements currently performed with the rotating directional probe at TEXTOR.

The presented rotating directional probe, allowing for a highly resolved, angular dependent measurement of the ion saturation current, is well suited for the measurements of fast ion losses and plasma rotation in the presence of local pitch-angle changes and dynamic perturbations. Its highly angular resolved data and their radial correlation strongly extend the achievable information on fast ion losses and the plasma rotation. The main focus for the future work with the probe is the effect of RMP on the fast ion losses and plasma rotation.

ACKNOWLEDGMENTS

The help of the whole TEXTOR Team is gratefully acknowledged, with special thanks to Jörg Thomas, Sebastian

Kraus, D. Brinkmann, U. Schaufert, G. Esser, and D. Nicolai. Furthermore, M.R. thanks Ch. Perez von Thun for the valuable discussions. Support from the Helmholtz Association in frame of the Helmholtz-University Young Investigators Group VH-NG-410 is gratefully acknowledged.

- ¹Y. Liang, "Overview of edge-localized mode control in tokamak plasmas," *Fusion Sci. Technol.* **59**(3), 586 (2011).
- ²M. Hudis and L. M. Lidsky, "Directional Langmuir probe," *J. Appl. Phys.* **41**(12), 5011 (1970).
- ³K.-S. Chung, "Mach probes," *Plasma Sources Sci. Technol.* **21**(6), 063001 (2012).
- ⁴K. Nagaoka, M. Isobe, K. Shinohara *et al.*, "Energetic ion measurements using a directional probe," *Plasma Fusion Res.* **1**, 005 (2006).
- ⁵C. S. MacLathry, C. Boucher, D. A. Poirier *et al.*, "Gundestrup: A Langmuir/Mach probe array for measuring flows in the scrape-off layer of TdeV," *Rev. Sci. Instrum.* **63**(8), 3923 (1992).
- ⁶S. Jachmich, P. Peleman, M. Van Schoor *et al.*, "First Mach probe measurements of rotation, electric field and particle transport in the DED-ergodized edge plasma of TEXTOR," in *33rd EPS Conference on Plasma Physics, Roma (Italy)*, 19–23 June 2006.
- ⁷X. Zhang, D. Dandurand, T. Gray *et al.*, "Calibrated cylindrical Mach probe in a plasma wind tunnel," *Rev. Sci. Instrum.* **82**(3), 033510 (2011).
- ⁸O. Neubauer, G. Czymek, B. Giesen *et al.*, "Design features of the tokamak TEXTOR," *Fusion Sci. Technol.* **47**(2), 76 (2005).
- ⁹M. Mitri, "Control of a fast reciprocating probe for the TEXTOR fusion experiment," M.S. thesis (University Duisburg-Essen, 2005).
- ¹⁰K. Dyabilin, M. Hron, J. Stöckel *et al.*, "Rotating Mach probe for ion flow measurements on the CASTOR tokamak," *Contrib. Plasma Phys.* **42**(1), 99 (2002).
- ¹¹J. P. Gunn, C. Boucher, P. Devynck *et al.*, "Edge flow measurements with Gundestrup probes," *Phys. Plasmas* **8**(5), 1995 (2001).
- ¹²H. V. Goubergen, R. R. Weynants, S. Jachmich *et al.*, "A 1D fluid model for the measurement of perpendicular flow in strongly magnetized plasmas," *Plasma Phys. Controlled Fusion* **41**(6), L17 (1999).
- ¹³I. H. Hutchinson, "Ion collection by probes in strong magnetic fields with plasma flow," *Phys. Rev. A* **37**, 4358 (1988).
- ¹⁴K.-S. Chung, "Why is the Mach probe formula expressed as $R = J_{up}/J_{in} = \exp[K M_{\infty}]?$," *Jpn. J. Appl. Phys.* **45**(10A), 7914 (2006).
- ¹⁵W. Heidbrink and G. Sadler, "The behaviour of fast ions in tokamak experiments," *Nucl. Fusion* **34**(4), 535 (1994).
- ¹⁶Y. Xu, C. Hidalgo, I. Shesterikov *et al.*, "Role of symmetry-breaking induced by $E_r \times B$ shear flows on developing residual stresses and intrinsic rotation in the TEXTOR tokamak," *Nucl. Fusion* **53**, 072001 (2013).
- ¹⁷Y. H. Xu, S. Jachmich, R. R. Weynants *et al.*, "Investigation of self-organized criticality behavior of edge plasma transport in Torus experiment of technology oriented research," *Phys. Plasmas* **11**(12), 5413 (2004).
- ¹⁸A. Kirk, B. Koch, R. Scannell *et al.*, "Evolution of filament structures during edge-localized modes in the MAST tokamak," *Phys. Rev. Lett.* **96**, 185001 (2006).
- ¹⁹O. Neubauer, G. Czymek, K. Finken *et al.*, "The dynamic ergodic divertor in TEXTOR—A novel tool for studying magnetic perturbation field effects," in *Proceedings of the 23rd Symposium of Fusion Technology* [Fusion Eng. Design **75–79**, 495 (2005)].
- ²⁰Y. Yang, Y. Liang, Y. Sun *et al.*, "Experimental observations of plasma edge magnetic field response to resonant magnetic perturbation on the TEXTOR tokamak," *Nucl. Fusion* **52**(7), 074014 (2012).

Name of journal: Review of Scientific Instruments

Impact factor: 1.602 (2012)

Type of authorship: 1st

Own contribution: 80%

Details of contribution: Testing and improvement of existing probe design, set-up of the measurement scenarios, development of and participation in building the data acquisition system, development and testing the data analysis method and tools, preparation and performing of the experiments, analysing the data, preparation and writing of the manuscript.

On the effects of magnetic perturbations on fast ion losses studied at TEXTOR

M Rack¹, Y Liang¹, P Denner¹, J Pearson¹, Y Yang², L Zeng²
and the TEXTOR Team

¹Forschungszentrum Jülich GmbH, Institut für Energie- und Klimaforschung –
Plasmaphysik, 52425 Jülich, Germany

²Institute of Plasma Physics, Chinese Academy of Sciences, Hefei 230031, China

Abstract. One criterion for the ignition of a fusion plasma is sufficient fast ion confinement. A key aspect in that context is the maintainability of good fast ion confinement in the presence of non-axisymmetric fields, such as those found in stellarators and during the application of resonant magnetic perturbations (RMPs) in tokamaks. This paper focuses on the influence of RMPs on the fast ion losses, studied at the Tokamak Experiment for Technology-Oriented Research (TEXTOR), a medium-sized device. TEXTOR is equipped with a flexible perturbation coil system, the dynamic ergodic divertor, allowing for the application of static or rotating perturbation fields. A rotating directional probe is used for the radially resolved fast ion loss measurements. The results achieved are presented and discussed for the poloidal/toroidal perturbation modes $m/n = 3/1$ and $6/2$, with static and rotating fields.

PACS numbers: 52.55.Fa, 52.55.Pi, 52.25.Gj

Submitted to: *Plasma Phys. Control. Fusion*

1. Introduction

Sufficiently high α -particle and, more generally, fast ion confinement is of importance for a self-sustaining burning fusion plasma. The fusion-born α -particles need to be confined until their high energy is mainly transferred to the bulk plasma, known as α -particle heating. Today, an open issue in fusion research is the sustainability of good fast ion confinement in the presence of non-axisymmetric fields, such as those found in stellarators [1, 2], and during the application of resonant magnetic perturbations (RMPs) on tokamaks [3, 4, 5]. The application of RMPs is currently the most promising technique for edge localized mode (ELM) control [6] and heat load distribution on the plasma facing components, and their usage in the next-generation fusion device ITER is very likely. Therefore, there is an increasing focus on the understanding of RMP effects on the fast ion losses. Theoretical and experimental work [3, 4, 7, 8, 9] is ongoing in this field; however, as of yet, final conclusions cannot be drawn. The understanding of these effects allows optimization of the fast ion confinement in the presence of non-axisymmetric fields for the next-generation fusion devices.

Studies of confined fast ions on the Tokamak Experiment for Technology-Oriented Research (TEXTOR) have been performed in the past using collective Thomson scattering [10, 11, 12, 13]. This paper focuses on the study of RMP effects on fast ion losses at TEXTOR. The measurements are performed using a rotating directional probe. Such probe measurements at TEXTOR with its flexible dynamic ergodic divertor (DED) may help towards the understanding of fast ion losses, which is needed for the next-generation fusion devices, like ITER and Wendelstein 7-X.

The paper is structured as follows: section 2 describes the experimental set-up, also giving an overview of the features and the qualification of the analysis method used for the rotating directional probe. The experimental results are presented in section 3, split into general features seen with this probe and the observations during the application of RMPs. Section 4 discusses the findings from TEXTOR in relation to other devices. Finally, the last section summarizes the observations on TEXTOR.

2. Experimental set-up

TEXTOR is a medium-sized tokamak with a cylindrical shape in a limiter design [14]. Its major and minor radii are $R = 1.75$ m and $a \approx 48$ cm. A plasma current of $I_p = 200$ kA and magnetic fields between $B_t = 1.3$ T and 2.2 T were chosen for the fast ion loss studies performed with both reversed. The central electron density for this experiment was $n_e = 1.5 \times 10^{19} \text{ m}^{-3}$ with deuterium as the species for the low-confinement mode (L-mode) plasma.

A flexible perturbation coil system, the DED [15], is used in our experiment for the application of static perturbation fields or fields rotating at up to 5 kHz. It is located on the high-field side as sketched in figure 1 (a) and differs from the more common rectangular perturbation coils in that the DED coils are aligned parallel to field lines

A. Publications included

On the effects of magnetic perturbations on fast ion losses studied at TEXTOR 3

on the surface with safety factor $q = 3$. Perturbations with dominant poloidal/toroidal mode numbers of either $m/n = 3/1$ or $6/2$ were applied for the experiment.

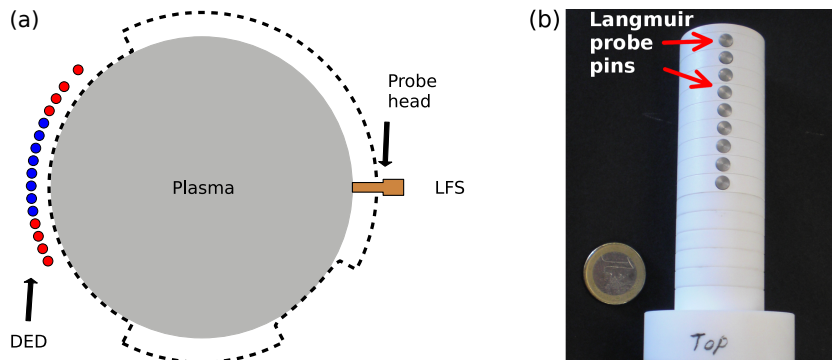


Figure 1. In (a) the geometrical set-up of the measurement is sketched. The poloidal cross-section of TEXTOR is shown at the toroidal location of the probe measurement ($\varphi \approx 346^\circ$). The dashed line gives the first wall of TEXTOR and the colours of the DED mark the current flow direction in the $m/n = 3/1$ perturbation mode (blue: clockwise, red: counter-clockwise). (b) gives a picture of the probe head. A similar array of Langmuir probe pins is located on the opposite side.

As TEXTOR cannot operate in a regime where fusion-born α -particles are created, tangential neutral beam injection (NBI) with an energy $E_{\text{NBI}} = 50 \text{ keV}$ was used as a proxy for generating fast ions in the plasma. Hydrogen atoms were injected. At TEXTOR, two tangential NBIs are available facing in opposite directions [16]. Most of the experiments performed used only one NBI facing in the co-current direction (stated if different). The power output of the NBI is controlled via the aperture of the beam [17]: in our standard settings with $P_{\text{NBI2}} = 600 \text{ kW}$, the so-called V-target was set to 120 mm.

The rotating directional probe [18] is mounted on the reciprocating probe [19, 20] and inserted from the low-field side (LFS) along the mid-plane into the scrape-off layer (SOL) to a final position of $r = 47 \text{ cm}$ touching the plasma edge at a toroidal angle $\varphi \approx 346^\circ$; see figure 1. The probe head is equipped with two arrays of nine Langmuir probe pins facing in opposite directions. A negative biasing (-160 V) is applied to the Langmuir probe pins in order to measure ion saturation currents. The probe rotates along its major axis during the measurements with a speed of about 4 Hz and acquires data at 0.5 MHz, allowing for a very high angular resolution. Radial profiles, with a resolution of $\Delta r = 6 \text{ mm}$, are recorded during the measurement. For each of the radial positions, an ion saturation current is measured as a function of angle, which is a requirement for an accurate detection of the fast ion losses.

Figure 2 shows time traces of the typical plasma parameters relevant for our experiment. The probe is inserted once during the discharge and rotated twice at its final radial position. The middle 360° of the rotation are used for the measurement. In figure 3, the measured ion saturation current of one probe channel is plotted against

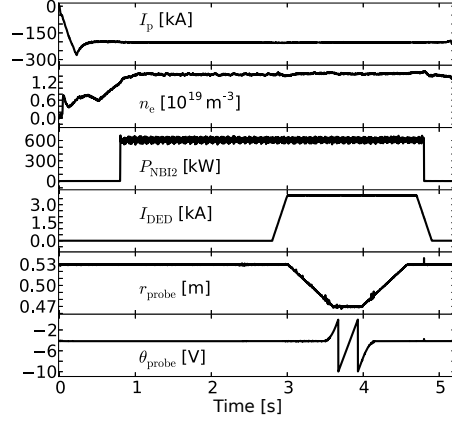


Figure 2. Time traces of typical plasma parameters for the experiments presented. From top to bottom: plasma current (I_p), electron density (n_e), power of NBI 2 (P_{NBI2}), DED current (I_{DED}), radial probe position (r_{probe}), and rotation angle of the probe (θ_{probe}), with -10 V to 0 corresponding to one complete turn.

the angle of rotation. The most obvious effect is the change from the low signal in the range $0^\circ < \theta < 180^\circ$ to the sine-like dependence during the second half of the rotation with a signal up to one order of magnitude higher. Furthermore, fast spikes with an amplitude of several hundred mA are superposed with the base signal and can be observed independently of the angle. These spikes are caused by transient events and are observed with a non-rotating probe as well. In other words, these events have a time dependence rather than an angular dependence; even so, their nature differs for opposite directions as present below.

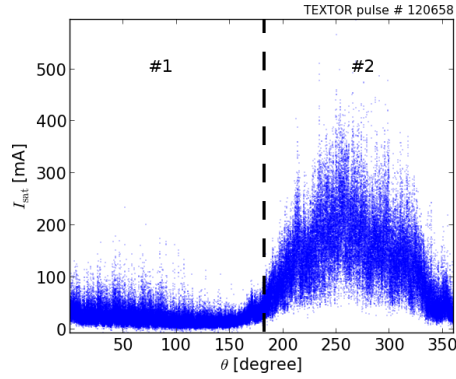


Figure 3. Measured ion saturation current of one channel of the probe plotted over the rotation angle. The measurement is taken at $r = 47.6\text{ cm}$.

The important aspect during the analysis of these data is the distinction between

A. Publications included

On the effects of magnetic perturbations on fast ion losses studied at TEXTOR 5

thermal and fast ion losses. An analysis technique for detecting beam-induced fast ions by means of a directional probe was initially presented in [21] and is further studied here. Therefore, the following considerations are made. Thermal ions show a correlation in the toroidal direction with a certain radial and poloidal extent as known from turbulence studies [22]. This is different from fast ions that only propagate in one direction. These show no correlation in the toroidal direction. Another aspect to consider is the much larger Larmor radius of the fast ions compared to the thermal ions. Consequently, the fast ions are travelling faster in radial direction when they are lost to the SOL. This also results in a difference in the correlation. The correlation of thermal ions has a radial extent but that of fast ions does not. These properties can be used to distinguish between thermal and fast ion losses using the rotating directional probe and comparing the signal of opposite facing probe pins. To do so, the correlation of the probe signal closest to the plasma is correlated to all the other probe signals with

$$R_{xy}(\tau) = \frac{1}{T} \int_{-T/2}^{T/2} x(t) \cdot y(t + \tau) dt, \quad (1)$$

where T is the time window used for the correlation (here 1 ms), and τ is the lag between the time-dependent signals x and y .

Figure 4 gives the peak values of the correlation R_{peak} for each time window ($T = 1$ ms) and the corresponding lag τ_{peak} of the signals. The correlations to the signals measured on the same side (a) and to signals from the opposite facing probe pins (b) are plotted. There are two main aspects to be pointed out: on the one hand, there is a clear difference between the first and second half of the rotation in (a); on the other hand, there is a very weak correlation to the probe signals of the opposite side. The latter is in agreement with the expectations for fast ion losses. One side of the opposite facing probe pins is always seeing the fast ion contribution. A consequence is that no correlation between opposite facing probe pins can be found. This directly follows the fact that the considered fast ions only propagate in one direction. The fact that there are two different regions in figure 4 (a) further supports the idea of the different nature of the main losses detected in the first and second half of the rotation, i.e. the losses from different directions. The strong correlation observed in the first half is due to thermal ions, which are transported outward on a longer time scale than fast ions and therefore show a radial correlation with a long tail. In addition, some events with inward propagating ions are seen for $110^\circ < \theta < 160^\circ$ ($\tau_{\text{peak}} > 0$). The second half also shows a correlation, but with a much shorter radial extent, which is a consequence of the strong fast ion content from that direction. It can be understood as the thermal part being perturbed by the fast ion contribution.

The difference can be made even clearer when averaging the correlation peaks detected in the first half (#1) and those from the second half (#2) and plotting these against the radial coordinate along the probe, see figure 5. The half containing the strong fast ion contribution (dashed) decays much more quickly. Additionally, the purely thermal part (solid) shows a long tail. The correlations to the probe signals from the opposite side (dashed-dotted, dotted) are also shown. These are below 12%

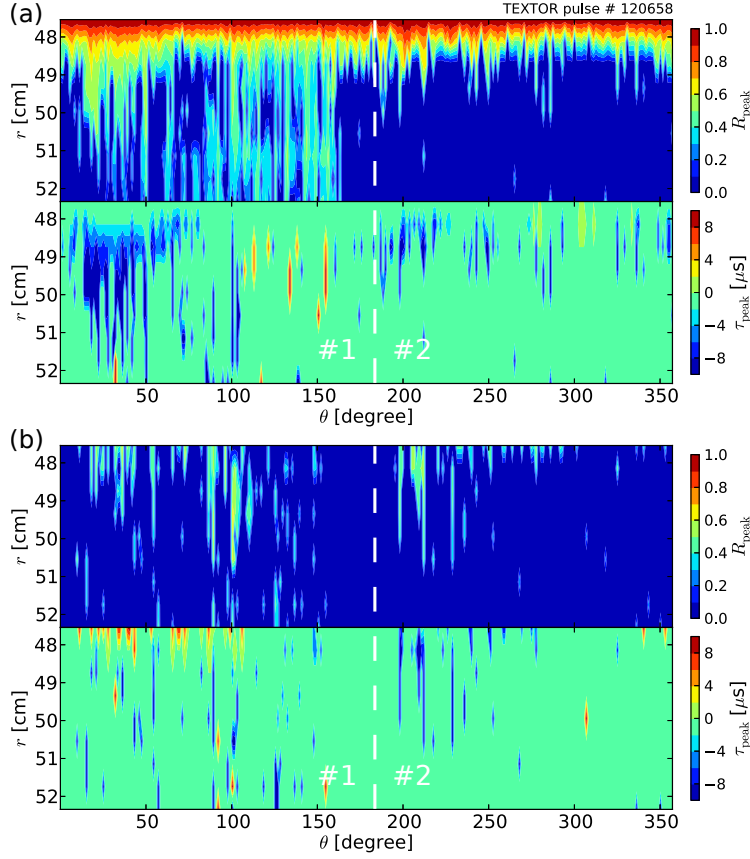


Figure 4. Correlation diagram of the probe signal close to the plasma with all other radial locations on the same (a) and opposite side (b). The correlation peak $R_{\text{peak}} := \max(R_{x,y})$ and corresponding lag time τ_{peak} are shown by the colour code for 1 ms time windows at different rotation angles of the probe.

along the entire profile. The different behaviour strongly supports the assumptions of the analysis method presented in [21, 18]: fast ions are only detected from one side.

In the following the transient events are neglected and only the slow change in the signal due to the rotation is considered. The angular dependent signals from opposite facing probe pins are fitted with sine curves to derive accurate values of the current density measured for the different directions. The fit formula is $I_{\text{sat}}(\theta_{\text{probe}})/A = (j_{\parallel} - j_{\perp}) \sin(\theta_{\text{probe}} - \theta_0) + j_{\perp}$, with the ion saturation current I_{sat} , the Langmuir probe pin area A , the parallel and perpendicular current densities j_{\parallel} , j_{\perp} , the rotation angle θ_{probe} , and the reference angle θ_0 at which the ion flux is normal to the probe pin area. The fraction of fast ion losses is determined by $j_{\text{loss}} = j_{\parallel, \text{Co}} - j_{\parallel, \text{Ctr}}$ [21]; for further details on the analysis, see [18]. A rotation of the probe by 180° is sufficient for measuring the

A. Publications included

On the effects of magnetic perturbations on fast ion losses studied at TEXTOR 7

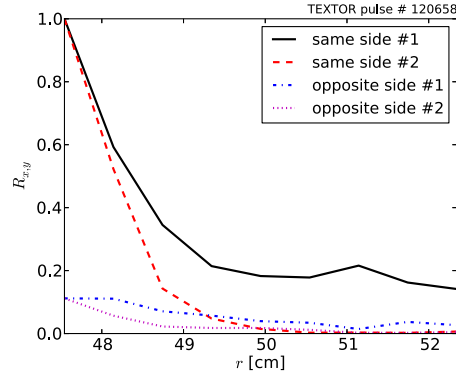


Figure 5. Averaged correlation peak profiles of the first half rotation (#1) and the second half rotation (#2) with the signals from the same and the opposite side.

fast ion losses as described in [18], but to improve the accuracy of the data presented, the fast ion losses have been calculated based on data for 360° , and the first and second half of a turn has been averaged. The error bars shown in the following figures result from systematic and fitting inaccuracies as well as the standard deviation of the averaging. The TEXTOR discharge numbers are given in the top-right corner of the figures, and the plasma parameters are stated in the shaded box within the figure.

3. Experimental results

3.1. General properties without additional magnetic perturbations

Before presenting the results from the RMP experiments, some general properties measured by the rotating directional probe are discussed, expanding those presented in [18]. A general property of the ion losses seen in figures 6 and 11 is their radial decay for $r \leq 50.6$ cm and a vanishing of the losses from around $r \geq 51.2$ cm, likely due to the interception of the plasma facing components.

3.1.1. Dependence on beam power The impact of the number of beam particles injected is studied based on discharges with different V-target opening, but the same acceleration energies of the particles. The triangles in figure 6 give a reference case of detected losses without additional beam particles. With increasing opening of the V-target, the detected losses increase for all radial positions $r \leq 50.6$ cm. At $r = 48.2$ cm, the cases with an opening larger than 60 mm are getting closer and overlap for $r = 47.6$ cm. This can possibly be explained by the location of the measurement being close or already inside the last closed flux surface (LCFS). Both the intrinsic and the beam-induced ion losses follow the plasma current direction. In the following, the effects on the ion losses detected between 48.8 cm $\leq r \leq 50.6$ cm are considered (dashed rectangle).

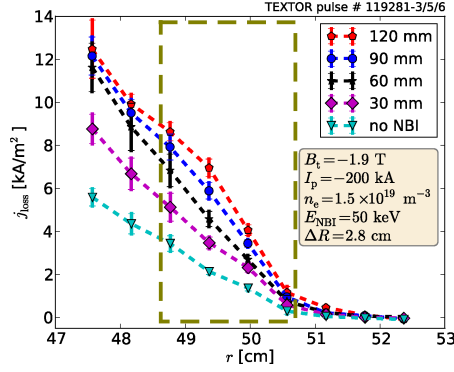


Figure 6. Radial profiles of the fast ion losses. The dependence on the NBI power is shown by changing the V-target opening, with 30 mm to 120 mm corresponding to a power of about 200 kW to 600 kW.

3.1.2. Dependence on plasma position As seen above, the losses depend on the distance from the LCFS. Exact measurements of the position of the LCFS at TEXTOR do not exist for the discharges studied. However, the location of the magnetic axis is known from laser interferometry measurements [23]. In the following, this is used to judge the difference in distance of the LCFS from the probe, keeping in mind that an exact measurement lacks the knowledge of the Shafranov shift. Figure 7 (top) shows the dependence of fast ion losses on the plasma position. The plasma position, ΔR , varies with respect to the geometrical centre while keeping all other plasma parameters the same. It is observed that a more outward plasma position (larger ΔR) causes higher losses as the plasma is closer to the probe compared to the cases with the plasma axis moved by about 2.5 cm further inwards. The discharges with plasma positions of $-7 \text{ cm} < \Delta R < -5 \text{ cm}$ show further reduced losses. No large differences can be seen in this range, likely due to the fact that the losses are already strongly reduced in this range and additional changes cannot be resolved.

However, a simple shift of the loss profiles cannot fully explain the observed changes if modifying ΔR . Additionally, the different plasma position affects the toroidal field ripple δ seen at the LCFS. The ripple is known to have a strong effect on the fast ion confinement [3] and should not be neglected in the interpretation of the observations. Therefore, the influence of the plasma shift on the ripple is also plotted in figure 7 (bottom). It can be seen that the ripple changes from 0.74% at the outermost plasma position to 0.33% for the innermost position. An increase in losses is observed when a stronger ripple is present, which is in line with observations from other devices. An interplay of both effects—the distance of the probe from the LCFS and the different toroidal field ripple—are likely to cause the observed influence on the ion losses.

The strong effect of the plasma position needs to be considered in the following studies. Consequently, the relative plasma position is stated as a plasma parameter and

A. Publications included

On the effects of magnetic perturbations on fast ion losses studied at TEXTOR 9

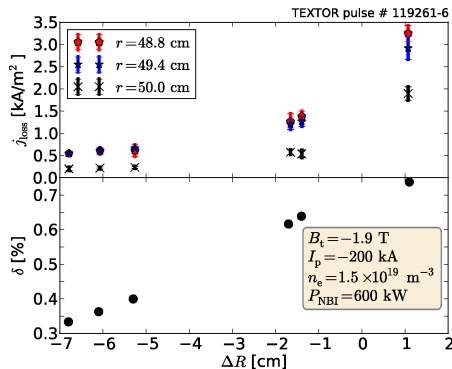


Figure 7. Dependence of the fast ion losses on the plasma position. The plasma position is given as the displacement ΔR of the magnetic axis with respect to the geometrical centre. On the top the ion losses are given and on the bottom the toroidal field ripple.

only those pulses with the about same plasma location are compared. Changes in the vertical plasma position are not detected at TEXTOR and are set to the geometrical centre for all discharges.

3.1.3. Dependence on beam ratio The availability of two opposite-facing NBIs at TEXTOR allows for the study of the effect of co- and counter-injected fast ions at constant heating power. Therefore, a beam ratio scan was performed. The power of each beam was controlled by changing the V-target while the dependence of V-target opening and beam power in the range considered is about linear (cf. figure 6 of [17]). The beam ratio f is determined as

$$f = \frac{(\text{opening NBI 2}) - (\text{opening NBI 1})}{(\text{opening NBI 2}) + (\text{opening NBI 1})}, \quad (2)$$

with a fixed total opening of 120 mm. The experimental results presented in figure 8 do show a trend to larger losses for predominantly co-injected cases, but not a clear dependence. It is observed that the losses for both extremes occur in the co-current direction.

Based on these observations, we can conclude that the observed losses do not result from passing particle losses, as those passing particles usually keep their initial direction of motion and therefore should lead to different loss directions if co- or counter-NBI is used. This is not seen here. Furthermore, prompt losses caused by intersection of the beam particles with the plasma-facing components are unlikely as they usually happen close to the fast ion source and should lead to a strong difference in the results at our measurement position as NBI 1 is much closer to the measurement position than NBI 2. Remaining types of known loss processes for the fast ions include the first orbit losses and the stochastization losses [24, 25].

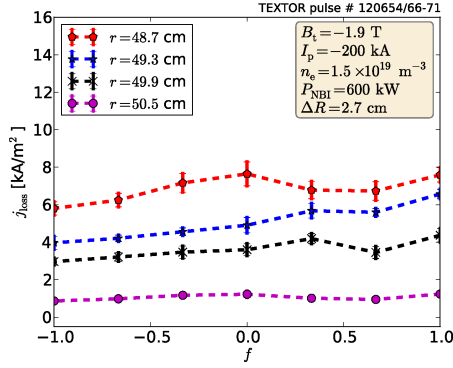


Figure 8. Influence of the NBI direction on the fast ion losses. Different ratios f of the V-target opening for each of the opposite facing NBI systems are compared.

3.2. Study of the influence of RMPs

For the study of RMP effects on fast ion losses, the DED is applied to create static as well as rotating fields in both perturbation modes $m/n = 3/1$ and $6/2$.

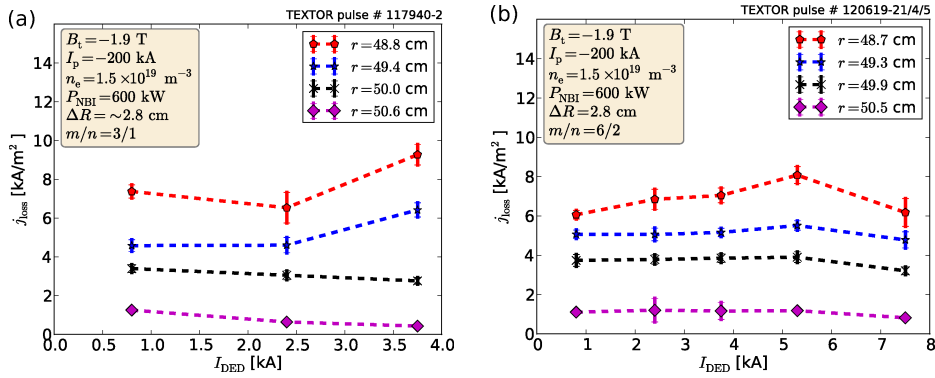


Figure 9. Effect of the static DED on fast ion losses. Different perturbation amplitudes for the perturbation modes $m/n = 3/1$ (a), and $m/n = 6/2$ (b) are shown.

3.2.1. Static DED Figure 9 shows the stepwise increase in the strength of a static perturbation field that covers the whole available range in both perturbation modes. Even at the maximum perturbation strength, no locked modes [26] are observed for those discharges. In figure 9 (a), results from the $3/1$ perturbation mode are shown. The three different perturbation amplitudes do not show a clear trend in the effect on the ion losses. Only for the strongest perturbation are increased losses seen at $r = 48.8$ cm and $r = 49.4$ cm. The further outward channels are not affected. Figure 9 (b) shows

A. Publications included

On the effects of magnetic perturbations on fast ion losses studied at TEXTOR 11

the results for the 6/2 cases. Due to the different perturbation mode, it is technically feasible to reach double the DED current. The results for the strongest and weakest perturbations are similar along the entire profile. For the other perturbation amplitudes, the losses at the innermost location appear to be slightly higher and peak around $I_{\text{DED}} = 5.3 \text{ kA}$. The strong increased losses for $r = 48.8 \text{ cm}$ and $r = 49.4 \text{ cm}$ as in the 3/1 cases cannot be found. From this results it is difficult to state a clear dependence of the perturbation amplitude of the DED on the fast ion losses at TEXTOR.

3.2.2. Rotating DED In figure 10 (a), the two different rotation directions are compared for the rotating DED in the 6/2 perturbation mode. The perturbation field was rotating with a frequency $f_{\text{DED}} = 1.38 \text{ kHz}$ in the co- (filled symbols) and counter-current (open symbols) direction. Each direction is studied at different perturbation amplitudes up to the maximum available. It should further be noted that only half the set of coils is used in the rotating 6/2 DED operation compared to the static operation. In both cases, the ion losses are identical for all three amplitudes. No dependence on the perturbation amplitude can be seen in the range considered.

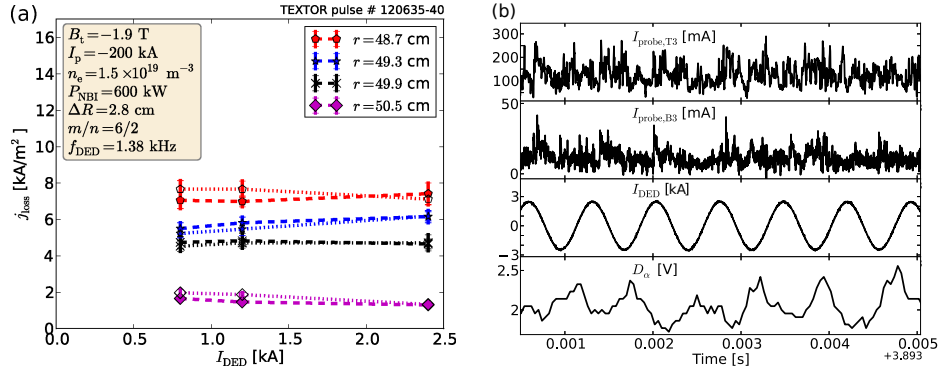


Figure 10. Effect of the rotating DED on fast ion losses. In (a) different perturbation amplitudes for co- (filled symbols) and counter-rotation (open symbols) with respect to the plasma current direction are shown. (b) shows the comparison of the ion saturation signal of two opposite-facing probe pins at $r = 48.7 \text{ cm}$ with the DED current modulation for TEXTOR discharge 120638 (cf. open pentagon in (a) at $I_{\text{DED}} = 2.4 \text{ kA}$). Additionally, the influence of the DED on the D_α signal is shown.

Due to the analysis method used on the experimental data, high-frequency modulations on the ion loss signal cannot be resolved in plots like those shown in figure 10 (a). Therefore, figure 10 (b) shows time traces of the raw ion saturation data in comparison with the DED amplitude and the D_α signal. The upper two time traces show the ion saturation current measured from opposite-facing probe pins at the same radial position $r = 48.7 \text{ cm}$ for a short time interval of about 5 ms. The interval is chosen at the time when the probe signals peak. Sub-structures can be seen in the probe signal, but they do not correlate with the DED amplitude modulation. In

contrast, the D_α signal shows a modulation following the DED amplitude as observed before on TEXTOR [27] which can be understood as results of the near field effects on the strike lines.

Experiments with the 3/1 perturbation mode have also been performed at TEXTOR for different rotation frequencies and directions. Technical restrictions only allow DED currents of up to 0.8 kA, but with the full set of coils and therefore only about a third weaker compared to the cases in the 6/2 perturbation mode. Frequencies of 1 kHz and 5 kHz have been used. Similar to the results with 3/1, the study in 6/2 does not show any impact on the fast ion losses. In conclusion, it can be stated that an effect of the rotating DED field on the fast ion losses cannot be observed at these perturbation amplitudes.

3.2.3. Dependence on edge safety factor An important aspect of RMP physics is the edge safety factor of the plasma as this defines the location of the resonant layers of the perturbation. To study the influence of different edge safety factors, q_a , under the same DED conditions, a q_a scan is performed by modifying B_t . Although the preferred technique for performing q_a scans is the variation of I_p rather than B_t in order to keep the effective perturbation the same, this is not an option when studying effects on fast ion losses. As presented in [28, 18], fast ion losses are strongly dependent on the chosen plasma current. Figure 11 shows the study of the B_t dependence. With the chosen B_t fields 1.3 T to 2.2 T, q_a ranges from about 4 to 7 and the effective perturbation decreases by 40%. The grey shaded region marks the reference cases without applied DED where no effect on the losses but a larger scatter can be seen. With the perturbation, B_t fields larger than 1.6 T do not show a clear dependence and lead to losses similar to the unperturbed cases. In contrast, a clear difference for the 1.3 T case (pentagons) is seen. The losses are strongly reduced by about a factor of two. Additionally, the shape of the radial profile changed strongly, which indicates a modified distribution of the fast ion losses. In the region $48.2 \text{ cm} < r < 50 \text{ cm}$, the profile becomes very flat, which could be an indication of fast radial transport in that region. Studying the magnetic response of the plasma, shows no mode locking or field penetration in this pulse. Instead, an increase in central plasma rotation is observed, seen via the sawtooth precursor mode, which spins up from 6.2 kHz to 7.8 kHz in the co-current direction. Such an effect due to the DED fields has previously been observed [29]; the only requirement for the observation is that no field penetration occurs as in the case here.

At first glance, the reduced losses appear counter-intuitive to an effect on fast ion losses by RMPs. The observation of reduced losses can mean three things: (a) increased losses appear at a different location in the torus and therefore the losses at the measurement position decrease, (b) an external kinking of the plasma results in a larger distance between the probe and the LCFS, which leads to reduced losses (cf. figure 7), or (c) the fast ion confinement improved, i.e. the losses are reduced. Due to a lack of diagnostic capabilities at TEXTOR it is not possible to measure the fast ion losses at a different location or to determine a possible kinking of the plasma edge. However,

A. Publications included

On the effects of magnetic perturbations on fast ion losses studied at TEXTOR 13

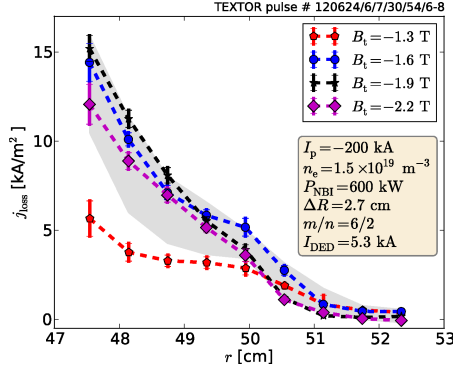


Figure 11. Effect of the edge safety factor on the fast ion losses. The scan was performed by changing B_t . The grey shaded region gives the reference to non-perturbed plasmas.

some considerations can be made to support the one idea or another. In contrast to other fast ion loss detectors, the rotating directional probe provides measurements along a radial profile. It is easily understood that measuring along the radial profile is equivalent to measuring along the toroidal direction: fast ions leaving the confined region propagate in the toroidal and radial directions before they intersect the plasma facing components. Consequently, the rotating directional probe provides information along a toroidal range and not only a local measurement. Tracing of fast ion orbits is required to get an estimate of the toroidal range covered; unfortunately, this does not exist. Still, the drop along the entire profile indicates improved fast ion confinement and diminishes possibility (a). A second aspect is the observed increase in plasma rotation. One consequence of increased plasma rotation is better confinement, also including better fast ion confinement. Nevertheless, modelling of the topology changes due to the DED fields and/or fast ion tracing is required for a complete understanding of the observations.

4. Discussion

The studies presented on different perturbation strengths and types have not shown a clear effect of the applied perturbation fields on fast ion losses, apart from the case with low edge safety factor. The low edge safety factor $q_a \approx 4$ leads to a strong resonance of the RMPs in the plasma edge as the DED is aligned with field lines on the $q = 3$ surface that are located close to the plasma edge for such a case. Consequently, a strong effect is seen. This is in line with observations from KSTAR: studies with perturbations which are resonant and non-resonant in the plasma edge have been performed leading to the result that only resonant perturbations show an effect on fast ion losses [9]. Those experiments at KSTAR were performed with perturbations of a toroidal mode

number $n = 1$. In the non-resonant cases, nearly twice as high perturbation fields were applied without effects on the fast ion losses. This supports the idea that only at strong resonances do the perturbation fields affect the fast ion confinement.

Another aspect to consider when evaluating the TEXTOR results is the limitation of the study to a fixed toroidal and poloidal location. Variation of the measurement position in the toroidal or poloidal direction was not possible. Experiments on other devices have shown a toroidal and poloidal dependence of fast ion losses towards the wall components. A strong toroidal dependence is found on ASDEX Upgrade (AUG) by measurements with fast ion loss detectors located about 30 cm above the mid-plane and 113° apart toroidally [9]. The toroidal asymmetry in the losses led to a strong increase at one position, while at the other position, the fast ion loss signal dropped rapidly if RMPs were applied. Recalling our finding for a low edge safety factor (figure 11), one explanation can be a toroidal asymmetry of the fast ion losses as found on AUG. However, in contrast to the radially localized measurements at AUG, the measurement at TEXTOR provides a radial profile which also contains information from different toroidal locations. Therefore, a drop along a wide toroidal range is seen, which gives a second possible explanation: a reduction of the fast ion losses. At DIII-D, losses appear predominantly at the mid-plane compared to a second detector significantly below the mid-plane, which is not strongly affected by the applied RMP [5]. The studies at DIII-D were performed in L-mode plasmas. There, a kinking of the plasma edge was observed when the effect on the fast ion losses were seen.

Furthermore, simulations with the ASCOT code, a Monte Carlo method-based fast ion tracer, show for AUG that the effect of RMPs on the losses strongly depends on the NBIs and toroidal field configurations used [8]. For simulations with high toroidal fields, nearly no effect of the RMP on the fast ion losses is seen. At low toroidal field, the amount of losses depends on the NBI system used (different in location and injection direction).

5. Summary

This article presents the results of a study of the RMP influence on fast ion losses at TEXTOR. The measurements were taken with a rotating directional probe located at the mid-plane at a fixed toroidal angle providing information along the radial axis in the SOL with a resolution $\Delta r = 6$ mm. From discharges without applied RMPs, the strong dependence of the losses on the location of the LCFS could be seen, and the appearance of passing particle losses could be excluded at the measurement position. During this work, clear RMP effects on the fast ion losses are only seen when investigating the edge safety factor dependence. At a low edge safety factor about $q_a \approx 4$, a strong reduction of the losses by 50% along the entire profile is observed when applying strong static perturbation fields with a poloidal/toroidal mode number $6/2$. At a moderate edge safety factor $q_a \approx 6$, RMP rotation scans in co- and counter-direction with frequencies of up to 5 kHz show no clear effects on the fast ion losses at TEXTOR. These scans have

A. Publications included

On the effects of magnetic perturbations on fast ion losses studied at TEXTOR 15

been performed for poloidal/toroidal mode numbers of 3/1 and 6/2. Theoretical studies that involve tracing the fast ions are required to understand the impact of RMPs on the losses at TEXTOR and can help towards a further interpretation of the experimental results.

Acknowledgments

Thanks to H. Jaegers, J. Aßmann, G. Satheeswaran, J. Thomas, S. Kraus, D. Brinkmann, and Ch. Perez von Thun for their help and valuable discussions. Support from the Helmholtz Association in the framework of the Helmholtz-University Young Investigators Group VH-NG-410 is gratefully acknowledged.

References

- [1] Strumberger E 2000 *Nuclear Fusion* **40** 1697
- [2] Osakabe M *et al.* 2010 *Fusion Science and Technology* **58** 131–140
- [3] Fasoli A *et al.* 2007 *Nuclear Fusion* **47** S264
- [4] Spong D A 2011 *Physics of Plasmas* **18** 056109
- [5] Zeeland M A V *et al.* 2014 *Plasma Physics and Controlled Fusion* **56** 015009
- [6] Liang Y 2011 *Fusion Science and Technology* **59** 586–601
- [7] Koskela T, Asunta O, Hirvijoki E, Kurki-Suonio T and Äkäslompolo S 2012 *Plasma Physics and Controlled Fusion* **54** 105008
- [8] Asunta O, Äkäslompolo S, Kurki-Suonio T, Koskela T, Sipilä S, Snicker A, noz M G M and the ASDEX Upgrade team 2012 *Nuclear Fusion* **52** 094014
- [9] Garcia-Munoz M *et al.* 2013 *Nuclear Fusion* **53** 123008
- [10] Bindslev H *et al.* 2007 *Plasma Physics and Controlled Fusion* **49** B551
- [11] Moseev D *et al.* 2011 *Plasma Physics and Controlled Fusion* **53** 105004
- [12] Nielsen S *et al.* 2011 *Nuclear Fusion* **51** 063014
- [13] Nielsen S K *et al.* 2008 *Physical Review E* **77** 016407
- [14] Neubauer O, Czymek G, Giesen B, Hüttemann P, Sauer M, Schalt W and Schruff J 2005 *Fusion Science and Technology* **47** 76–86
- [15] Neubauer O, Czymek G, Finken K, Giesen B, Hüttemann P, Lambertz H and Schruff J 2005 *Fusion Engineering and Design* **75-79** 495 – 498 Proceedings of the 23rd Symposium of Fusion Technology
- [16] Euringer H, Lochter M, Pfister U and Uhlemann R 1989 in *Fusion Engineering, 1989. Proceedings., IEEE Thirteenth Symposium on* pages 991–995 vol.2
- [17] Uhlemann R and Ongena J 1999 *Fusion Science and Technology* **35** 42–53
- [18] Rack M, Liang Y, Jaegers H, Aßmann J, Satheeswaran G, Xu Y, Pearson J, Yang Y, Denner P and Zeng L 2013 *Review of Scientific Instruments* **84** 083501
- [19] Cosler A, Hothker K, Kemmerit E, Schurer M, Bieger W and Heuser W 1995 in *Fusion Engineering, 1995. SOFE '95. Seeking a New Energy Era., 16th IEEE/NPSS Symposium* volume 2 pages 1051–1053
- [20] Mitri M 2005 *Control of a Fast Reciprocating Probe for the TEXTOR Fusion Experiment* Master's thesis University Duisburg-Essen
- [21] Nagaoka K, Isobe M, Shinohara K, Osakabe M, Shimizu A and Okamura S 2006 *Plasma and Fusion Research* **1** 005–005
- [22] Gunn J, Stckel J, Admek J, uran I, Horek J, Hron M, Jakubka K, Kryka L, ek F and Van Oost G 2001 *Czechoslovak Journal of Physics* **51** 1001–1010 10.1023/A:1012885815332
- [23] Donné A *et al.* 2005 *Fusion Science and Technology* **47** 220–245

- [24] Goldston R J, White R B and Boozer A H 1981 *Physical Review Letters* **47** 647–649
- [25] Zweben S *et al.* 1995 *Nuclear Fusion* **35** 893
- [26] Koslowski H R *et al.* 2006 *Plasma Physics and Controlled Fusion* **48** B53
- [27] Finken K *et al.* 2007 *Nuclear Fusion* **47** 522
- [28] Heidbrink W and Sadler G 1994 *Nuclear Fusion* **34** 535
- [29] Bock M D, Classen I, Busch C, Jaspers R, Koslowski H, Unterberg B and the TEXTOR Team
2008 *Nuclear Fusion* **48** 015007

A. Publications included

Name of journal: submitted to Plasma Physics and Controlled Fusion

Impact factor: 2.369 (2012)

Type of authorship: 1st

Own contribution: 90%

Details of contribution: Designing and performing the experiments, development and testing of the advancement of the data analysis, data analysis and interpretation, preparation and writing of the manuscript.

B. Commonly used acronyms

Some experienced scientists in the field of magnetically confined fusion love to use acronyms when talking about their own research. For young scientists, such as master and Ph.D. students, it is very difficult to follow these discussions in the beginning. Nevertheless, fusion needs many young and interested researchers, being able to understand each other as good as possible, to reach the ambitious goal of a working fusion reactor in the next decades.

Therefore, young fusion scientists might find the following list of acronyms, commonly used in the field of magnetically confined fusion, helpful. For further details the first appearance of each acronym in this dissertation is given.

ASDEX Axially Symmetric Divertor EXperiment.....	4
AUG ASDEX Upgrade.....	9
DED dynamic ergodic divertor.....	9
EFCC error field correction coil.....	8
EAST Experimental Advanced Superconducting Tokamak.....	10
ELM edge localized mode.....	5
H-mode high-confinement mode.....	4

B. Commonly used acronyms

HFS high-field side	9
JET Joint European Torus	3
L-mode low-confinement mode	4
LCFS last closed flux surface	3
LFS low-field side	15
LHW lower hybrid wave	9
NBI neutral beam injection	30
RMP resonant magnetic perturbation	5
SOL scrape-off layer	3
TEXTOR Tokamak Experiment for Technology-Oriented Research	3

Acknowledgments/Danksagung

An aller erste Stelle danke ich meiner Familie und meiner Freundin. Die kontinuierliche Unterstützung hat mir geholfen im Auge zu behalten, was im Leben wirklich wichtig ist. Ohne ihrer Hilfe wäre ich nie in der Lage gewesen diese Dissertation mit so großem Erfolg abzuschließen.

Als nächstes danke ich den Technikern und Ingenieuren, die mir bei meinen Arbeiten für und an TEXTOR geholfen haben: Herrn Jaegers, der mich die Grundlagen im Umgang mit Sonden und Vorgängen an TEXTOR lehrte; Herrn Schaufert und Dr. Krämer-Flecken, für die Hilfe mit der Datenerfassung; Guru Satheeswaran und Jochen Aßmann, von denen ich hervorragende Unterstützung bei den Arbeiten mit der Schnellen Sonde und dem Sondenkopf erhalten habe; Sebastian Kraus, Jörg Thomas und Horst Lambertz, für ihren schnelle Einsatz, wenn die Steuerung der Schnellen Sonde versagte; Dirk Nicolai, Manfred Sauer, Gerwin Esser und Robert Habrichs, für den Betrieb von TEXTOR und die Bereitschaft alle meine Fragen zu dessen technischen Details zu beantworten. Thanks also go to Dr. Yuhong Xu, Dr. Yao Yang, and Dr. Arkadi Kreter for introducing me to the fast reciprocating probe from the point of view of a scientist.

Ich danke Thomas Eich und Bernhard Sieglin, den Kollegen aus Garching. Das frühe Zusammentreffen war eine große Bereicherung für mich. Durch sie wurde ich in infrarot Thermographie trainiert und bekam die Möglichkeit interessante Forschung am weltweit größten Fusionsexperiment, JET, durchzuführen. Zudem, besten Dank an Bernhard für die Bekanntmachung mit Python und an Thomas für seine wertvollen Kommentare in den unterschiedlichsten Phasen meiner Vorbereitung auf die Dissertation. Ohne diese beiden wäre der Spaß und der Erfolg der Arbeit wesentlich geringer gewesen. I also acknowledge the good team work with Dr. Itziar Balboa at JET.

A special thanks go to Dr. Rudi Koslowski, Dr. Jonathan Pearson, and Dr. Peter Denner. I experienced them not only as colleges, but also as friends from which I received useful comments all over the time – colleges that made

the work in Jülich more enjoyable. Also, to be mentioned here: Albert Hiller (thanks for all the stories about Thomas), Yu Gao (thanks for the good experience in supervising you), Long Zeng, Roland Bär, and Philipp Drews.

Danke, an meine ehemaligen Kollegen vom Institut für theoretische Physik I der Heinrich-Heine Universität in Düsseldorf. Die technische Unterstützung durch Dr. Götz Lehmann und Evgenij Bleile hat das Erreichen meiner Ziele um einiges beschleunigt. Ein besonderer Dank gilt Prof. Dr. Spatschek und Dr. Andreas Wingen, die mich während Bachelor- und Masterarbeit hervorragende ausgebildet haben und mir während meiner Promotion weiterhin zur Seite standen.

Ich danke den Direktoren des IEK-4, unter denen ich arbeiten durfte. Prof. Reiter für das Zutrauen, dass ich auch experimentell erfolgreich arbeiten kann und Prof. Samm ganz besonders für die guten Gespräche in der Endphase meines Promotionsvorhabens, sowie das generelle Vertrauen, dass er mir entgegengebracht hat.

Finally, I thank my supervisor, Dr. Yunfeng Liang, for all the opportunities I got and the freedom to choose the focus of my work. I could gain a lot from his wide knowledge, especially in the field of MHD physics. Furthermore, his example helped me to see which path I want to take in the future.

Eidesstattliche Versicherung

Ich versichere an Eides Statt, dass die Dissertation von mir selbständig und ohne unzulässige fremde Hilfe unter Beachtung der “Grundsätze zur Sicherung guter wissenschaftlicher Praxis an der Heinrich-Heine-Universität Düsseldorf” erstellt worden ist.

Jülich, den

Erklärung

Hiermit erkläre ich, dass ich die Dissertation keiner anderen Fakultät vorgelegt habe und keinerlei erfolglose oder erfolgreiche Promotionsversuche unternommen habe.

Jülich, den